Image Synthesis for the Attenuation Correction and Analysis of PET/MR Data

Ninon Burgos

A dissertation submitted in partial fulfillment

of the requirements for the degree of

Doctor of Philosophy

of

University College London.

Department of Medical Physics and Biomedical Engineering

University College London

September 2016

I, Ninon Burgos, confirm that the work presented in this thesis is my own. Where information has been derived from other sources, I confirm that this has been indicated in the work.

A moumou et poupou

Abstract

While magnetic resonance imaging (MRI) provides high-resolution anatomical information, positron emission tomography (PET) provides functional information. Combined PET/MR scanners are expected to offer a new range of clinical applications but efforts are still necessary to mitigate some limitations of this promising technology. One of the factors limiting the use of PET/MR scanners, especially in the case of neurology studies, is the imperfect attenuation correction, leading to a strong bias of the PET activity. Exploiting the simultaneous acquisition of both modalities, I explored a new family of methods to synthesise X-ray computed tomography (CT) images from MR images. The synthetic images are generated through a multi-atlas information propagation scheme, locally matching the MRI-derived patient's morphology to a database of MR/CT image pairs, using a local image similarity measure. The proposed algorithm provides a significant improvement in PET reconstruction accuracy when compared with the current correction, allowing an unbiased analysis of the PET images.

A similar image synthesis scheme was then used to better identify abnormalities in cerebral glucose metabolism measured by ^{18}F-fluorodeoxyglucose (FDG) PET. This framework consists of creating a subject-specific healthy PET model based on the propagation of morphologically-matched PET images, and comparing the subject's PET image to the model via a Z-score. By accounting for inter-subject morphological differences, the proposed method reduces the variance of the normal population used for comparison in the Z-score, thus increasing the sensitivity.

To demonstrate that the applicability of the proposed CT synthesis method is not limited to PET/MR attenuation correction, I redesigned the synthesis process to derive tissue attenuation properties from MR images in the head & neck and pelvic regions to facilitate MR-based radiotherapy treatment planning.

Acknowledgements

I would like to start by thanking my supervisors Prof. Sébastien Ourselin, Prof. Brian Hutton and Dr M. Jorge Cardoso for their support and advice throughout my PhD. A special thank you to Jorge who encouraged me, shared his knowledge and was there each time I needed him.

I thank Siemens for funding my project together with the UCL Faculty of Engineering, and Chloe Hutton and Jerome Declerck for their comments on the work done in this thesis.

I am thankful to Prof. John Duncan and Dr Jonathan Schott for providing most of the data used in this thesis, and to all the people I worked with at the Dementia Research Centre and the Institute of Nuclear Medicine for providing help and advice.

I would have never moved to London without the encouragement of Christian Faye and Thomas Tang who convinced me that I could find my way in research and helped me get where I am today. A very warm thank you.

Thanks to all the people at the Centre for Medical Image Computing and Translational Imaging Group who made my PhD years so pleasant, particularly my office mates and those few who will recognise themselves when reading these lines.

Finally I would like to thank my parents for their unconditional support wherever life has carried me.

Publication List

Journal papers

1. Sekine, T., **Burgos, N.**, Warnock, G., Huellner, M.W., Buck A., ter Voert, EGW , Cardoso, M.J., Hutton, B.F., Ourselin, S., Veit-Haibach, P., and Delso, G.: Multi atlas-based attenuation correction for brain FDG-PET imaging using a TOF-PET/MR scanner—comparison with clinical single atlas- and CT-based attenuation correction. *Journal of Nuclear Medicine*, 57(8): 12581264, 2016

2. Jiao, J., Bousse, A., Thielemans, K., **Burgos, N.**, Weston, P., Markiewicz, P., Schott, J., Atkinson, D., Arridge, S.R., Hutton, B.F. and Ourselin, S.: Direct parametric reconstruction with joint motion estimation/correction for dynamic brain PET data. *IEEE Transactions on Medical Imaging*, 2016 (in press)

3. Guerreiro*, F., **Burgos*, N.**, Dunlop, A., Wong, K., Petkar, I., Nutting, C., Harrington, K., Bhide, S., Newbold, K., Dearnaley, D., deSouza, N.M., Morgan, V.A., McClelland, J., Nill, S., Cardoso, M.J., Ourselin, S., Oelfke, U., Knopf, AC.: Evaluation of a multi-atlas CT synthesis approach for MRI-only radiotherapy treatment planning. *Physica Medica* (submitted, *: joint first authorship)

4. Ladefoged, C. N., Law, I., Anazodo, U., St. Lawrence, K., Izquierdo-Garcia, D., Catana, C., **Burgos, N.**, Cardoso, M.J., Hutton, B.F., Ourselin, S., Merida, I., Costes, N., Hammers, A., Benoit, D., Holm, S., Juttukonda, M., An, H., Cabello, J., Lukas, M., Nekolla, S., Ziegler, S., Fenchel, M., Jakoby, B., Casey, M., Benzinger, T., Højgaard, L., Hansen, A.E., and Andersen, F.L.: A multicentre evaluation study of eleven PET/MRI brain attenuation correction methods on a large cohort of patients: ready for clinical implementation. *NeuroImage* (submitted)

5. **Burgos, N.**, Cardoso, M.J., Thielemans, K., Modat, M., Dickson, J., Schott, J.M., Atkinson, D., Arridge, S.R., Hutton, B.F. and Ourselin, S.: Multi-contrast attenuation map synthesis for PET/MR scanners: Assessment on FDG and Florbetapir PET tracers. *European Journal of Nuclear Medicine and Molecular Imaging*, 42(9): 1447–1458, 2015

6. Zuluaga*, M.A., **Burgos*, N.**, Mendelson, A.F., Taylor, A.M., Ourselin, S.: Voxelwise atlas rating for computer assisted diagnosis: Application to cardiovascular diseases. *Medical Image Analysis*, 26(1): 185–194, 2015 (*: joint first authorship)

7. Kochan, M., Daga, P., **Burgos, N.**, White, M., Cardoso, M.J., Mancini, L., Winston, G.P., McEvoy, A.W., Thornton, J., Yousry, T., Duncan, J.S., Stoyanov D., Ourselin S.: Simulated field maps

for susceptibility artefact correction in interventional MRI. *International Journal of Computer Assisted Radiology and Surgery*, 10(9): 1405–1416, 2015

8. Weston, P.S.J., Paterson, R.W., Modat, M., **Burgos, N.**, Cardoso, M.J., Magdalinou, N., Lehmann, M., Dickson, J., Barnes, A., Bomanji, J.B., Kayani, I., Cash, D.M., Ourselin, S., Toombs, J., Lunn, M.P., Mummery, C.J., Warren, J.D., Rossor, M.N., Fox, N.C., Zetterberg, H., Schott, J.M.: Using florbetapir PET to explore CSF cut-points and grey zones in small sample sizes. *Alzheimer's & Dementia: Diagnosis and Disease Monitoring*, 1(4): 440–446, 2015

9. **Burgos, N.**, Cardoso, M.J., Thielemans, K., Modat, M., Pedemonte, S., Dickson, J., Barnes, A., Ahmed, R., Mahoney, C.J., Schott, J. M., Duncan, J.S., Atkinson, D., Arridge, S.R., Hutton, B.F. and Ourselin, S.: Attenuation correction synthesis for hybrid PET-MR scanners: Application to brain studies. *IEEE Transactions on Medical Imaging*, 33(12): 2332–2341, 2014

Conference papers

1. **Burgos, N.**, Guerreiro, F., McClelland, J., Nill, S., Dearnaley, D., deSouza, N.M., Oelfke, U., Knopf, A-C., Ourselin, S. and Cardoso, M.J.: Joint segmentation and CT synthesis for MRI-only radiotherapy treatment planning. *MICCAI*, 2016

2. Ladefoged, C. N., Law, I., Anazodo, U., St. Lawrence, K., Izquierdo-Garcia, D., Catana, C., **Burgos, N.**, Cardoso, M.J., Hutton, B.F., Ourselin, S., Merida, I., Costes, N., Hammers, A., Benoit, D., Holm, S., Juttukonda, M., An, H., Cabello, J., Lukas, M., Nekolla, S., Ziegler, S., Fenchel, M., Jakoby, B., Casey, M., Benzinger, T., Højgaard, L., Hansen, A.E., and Andersen, F.L.: Multi-center evaluation of eleven PET/MRI brain attenuation correction methods. *IEEE NSS-MIC*, 2016

3. **Burgos, N.**, Cardoso, M.J., Mendelson, A.F., Schott, J.M., Atkinson, D., Arridge, S.R., Hutton, B.F., Ourselin, S.: Subject-specific models for the analysis of pathological FDG PET data. *MICCAI*, 2015

4. **Burgos, N.**, Cardoso, M.J., Guerreiro, F., Veiga, C., Modat, M, McClelland, J., Knopf, A-C., Punwani, S., Atkinson, D., Arridge, S.R., Hutton, B.F. and Ourselin, S.: Robust CT synthesis for radiotherapy planning: Application to the head & neck region. *MICCAI*, 2015

5. Zuluaga*, M.A., **Burgos*, N.**, Taylor, A.M., Ourselin, S.: Multi-atlas synthesis for computer assisted diagnosis: Application to cardiovascular diseases. *IEEE ISBI*, 2015

6. Jiao J., Markiewicz P., **Burgos N.**, A. David, Hutton B.F., Arridge S.R., Ourselin S.: Detail-preserving PET reconstruction with sparse image representation and anatomical priors. *IPMI*, 2015

7. **Burgos, N.**, Thielemans, K., Cardoso, M.J., Markiewicz, P., Jiao, J., Dickson, J., Duncan, J.S., Atkinson, D., Arridge, S.R., Hutton, B.F. and Ourselin, S.: Effect of scatter correction when comparing attenuation maps: Application to brain PET/MR. *IEEE NSS-MIC*, 2014

8. Jiao, J., Bousse, A., Thielemans, K., Markiewicz, P., **Burgos, N.**, S., Atkinson, D., Arridge, S.R., Hutton, B.F. and Ourselin, S.: Joint parametric reconstruction and motion correction framework for dynamic PET data. *MICCAI*, 2014

9. Kochan, M., Daga, P., **Burgos, N.**, White, M., Cardoso, M.J., Mancini, L., Winston, G.P., McEvoy, A.W., Thornton, J., Yousry, T., Duncan, J.S., Stoyanov D., Ourselin S.: Simulated field maps: Toward improved susceptibility artefact correction in interventional MRI. *IPCAI*, 2014

10. **Burgos, N.**, Cardoso, M.J., Modat, M., Pedemonte, S., Dickson, J., Barnes, A., Duncan, J.S., Atkinson, D., Arridge, S.R., Hutton, B.F. and Ourselin, S.: Attenuation correction synthesis for hybrid PET-MR scanners. *MICCAI*, 2013

Conference abstracts

1. **Burgos, N.**, Cardoso, M.J., Guerreiro, F., McClelland, J., Knopf, A-C. and Ourselin, S.: Simultaneous organ-at-risk segmentation and CT synthesis in the pelvic region for MRI-only radiotherapy treatment planning. *ICCR*, 2016

2. **Burgos, N.**, Cardoso, M.J., Guerreiro, F., McClelland, J., Knopf, A-C., Punwani, S. and Ourselin, S.: CT synthesis in the head & neck and pelvic regions for radiotherapy treatment planning. *IPEM Workshop on MRI Guided Radiotherapy*, 2016

3. Sekine, T., **Burgos, N.**, Warnock, G., Huellner, M.W., Buck A., ter Voert, EGW , Cardoso, M.J., Hutton, B.F., Ourselin, S., Veit-Haibach, P., and Delso, G., Multi atlas-based attenuation correction for brain FDG-PET imaging using a TOF-PET/MR scanner—comparison with clinical single atlas- and CT-based attenuation correction. *ISMRM*, 2016

4. Prados, F., Cardoso, M.J., **Burgos, N.**, Wheeler-Kingshott, C. and Ourselin, S.: NiftyWeb: web based platform for image processing on the cloud, *ISMRM*, 2016

5. Ladefoged, C. N., Law, I., Anazodo, U., Izquierdo-Garcia, D., **Burgos, N.**, Merida, I., Benoit, D., Juttukonda, M., Cabello, J., Fenchel, M., Jakoby, B., Højgaard, L., Hansen, A.E., and Andersen, F.L.: A multi-method, multi-center study of PET/MRI brain attenuation correction on a large cohort of [18F]-FDG patients: ready for clinical implementation. RSNA, 2016

6. **Burgos, N.**, Cardoso, M.J., Modat, M, Punwani, S., Atkinson, D., Arridge, S. R., Hutton, B. F. and Ourselin, S.: CT synthesis in the head & neck region for PET/MR attenuation correction: an iterative multi-atlas approach. *EJNMMI Physics*, 2(Suppl 1):A31, 2015

7. Guerreiro, F., McClelland, J., **Burgos, N.**, Cardoso, M.J., Dunlop, A., Wong, K., Nill, S., Oelfke, U. and Knopf, AC.: Evaluation of different approaches to obtain synthetic CT images for a MRI-only radiotherapy workflow, *MR in RT*, 2015

8. Dickson, J., Erlandsson, K., Lehmann, M., Modat, M., **Burgos, N.**, Groves, A., Schott, J.M.: Partial volume correction of Amyvid and FDG PET data using the discrete iterative Yang technique. *EJNMMI*, 42, S69-S69, 2015

9. Mota, A., Cuplov, V., Schott, J.M., Hutton, B.F, Thielemans, K., Drobnjak, I., Dickson, J., Bert, J., **Burgos, N.**, Cardoso, M.J., Modat, M., Ourselin, S., and Erlandsson, K.: Establishment of an open database of realistic simulated data for evaluation of partial volume correction techniques in brain PET/MR. *EJNMMI Physics*, 2(Suppl 1):A44, 2015

10. **Burgos, N.**, Cardoso, M.J., Thielemans, K., Duncan, J. S., Atkinson, D., Arridge, S. R., Hutton, B. F. and Ourselin, S.: Attenuation correction synthesis for hybrid PET-MR scanners: Validation for brain study applications. *EJNMMI Physics*, 1(Suppl 1):A52, 2014

11. Markiewicz, P., Thielemans, K., **Burgos, N.**, Manber, R., Jiao, J., Barnes, A., Atkinson, D., Arridge, S. R., Hutton, B. F. and Ourselin: Image reconstruction of mMR PET data using the open source software STIR. *EJNMMI Physics*, 1(Suppl 1):A44, 2014

Contents

Glossary

μmap Attenuation map

Aβ ^{18}F-florbetapir tracer

AC Attenuation correction

CSF Cerebrospinal fluid

CT Computed tomography

CV Coefficient of variation

DVH Dose volume histogram

FCM Fuzzy c-means

FDE Frequency domain entropy

FDG ^{18}F-fluorodeoxyglucose

FOV Field of view

GPU Graphics processing unit

HU Hounsfield units

ICBM International Consortium for Brain Mapping

LAC Linear attenuation coefficient

LIS Local image similarity

LNCC Local normalised correlation coefficient

LNSSD Local normalised sum of square differences

LOR Line of response

LPA Logopenic progressive aphasia

MAE Mean absolute error

ME Mean error

MPRAGE Magnetisation-prepared rapid gradient-echo

MR Magnetic resonance

MRI Magnetic resonance imaging

NAC Non attenuation corrected

OAR Organ at risk

OSEM Ordered subsets expectation maximisation

PCA Posterior cortical atrophy

pCT Pseudo CT

PD Proton density

PD-w PD-weighted

PET Positron emission tomography

PiB Pittsburgh compound B

PNFA Progressive nonfluent aphasia

PSF Point spread function

PTV Planning target volume

R2 Spin-spin relaxation rate

R2* Spin-spin relaxation rate with local magnetic field inhomogeneities

rMAE Relative mean absolute error

rME Relative mean error

ROI Region of interest

RTP Radiotherapy treatment planning

SD Standard deviation

SPM Statistical Parametric Mapping

SSD Sum of square differences

SSS Single scatter simulation

SUV Standardised uptake value

SUVR Standardised uptake value ratio

T1 Spin-lattice relaxation time

T1-w T1-weighted

T2 Spin-spin relaxation time

T2* Spin-spin relaxation time with local magnetic field inhomogeneities

T2-w T2-weighted

TE Echo time

TE_1 Time of the first echo when referring to the UTE sequence

TE_2 Time of the first echo when referring to the UTE sequence

TOF Time of flight

TR Repetition time

UTE Ultrashort echo time

UTE_1 First-echo image when referring to the UTE sequence

UTE_2 Second-echo image when referring to the UTE sequence

List of Figures

List of Tables

Chapter 1

Introduction

The end goals of medical research are to detect, diagnose, treat, and ultimately prevent diseases, thus improving human health and welfare. This requires an understanding of the cellular, molecular and physiological mechanisms occurring both in the healthy and diseased human body. Medical imaging plays an important role in the prevention, detection, diagnosis and treatment monitoring of diseases, and new technology is being developed to improve patient care. Medical imaging includes many different imaging modalities such as X-ray computed tomography, magnetic resonance imaging (MRI), ultrasound, positron emission tomography (PET), and optical tomography. Recently, research has been focused on exploiting the synergies existing between different modalities, which led to the development of hybrid PET/MR imaging. PET/MR systems allow the simultaneous acquisition of both PET and MRI modalities by a single scanner. By combining functional and anatomical information, PET/MR scanners are expected to offer a new range of clinical applications. However, efforts are still necessary to mitigate some limitations of this promising technology. This is the subject of this thesis.

1.1 Imaging modalities

Medical imaging comprises a wide range of single and combined imaging modalities. I first focus on the individual modalities.

1.1.1 Positron emission tomography

Positron emission tomography is an imaging technique that requires the injection of a substance labelled with a positron-emitting radioactive isotope. The labelled substance is distributed throughout the patient's body by the blood circulation and accumulates in target regions. The positrons emitted by the radioactive isotope combine with the electrons present in the tissues and annihilate. Each annihilation produces two nearly collinear photons (Figure 1.1). The two photons are simultaneously detected by two opposing detectors and a coincidence event is assigned to a line of response (LOR) connecting the two detectors. In a time of flight (TOF) PET system, the difference in arrival times between the two coincident photons is measured. Without TOF information, the annihilation is located with equal probability along the LOR, while with TOF information, the annihilation site can be reduced to a limited range (Figure 1.2), thus decreasing the spatial uncertainty and increasing the signal-to-noise ratio. Once reconstructed, the PET image is a map of the radioactivity distribution throughout the body.

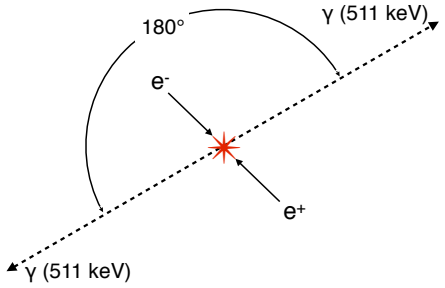

Figure 1.1: PET annihilation. When a positron (e^+) and an electron (e^-) collide, they annihilate and create a pair of collinear gamma rays (γ).

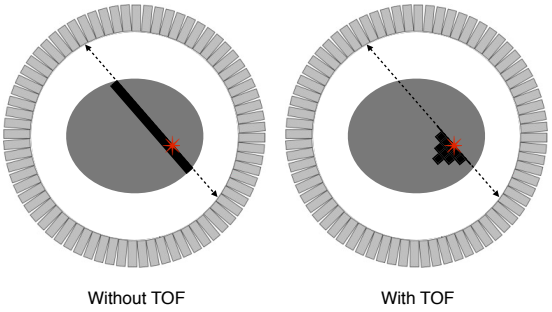

Figure 1.2: Illustration of PET data detection. Without TOF, the annihilation is located with equal probability along the LOR, while with TOF, it is located in a limited portion of the LOR.

2-deoxy-2-[^{18}F]fluoro-D-glucose, or ^{18}F-fluorodeoxyglucose (FDG), is the most widely used PET radiopharmaceutical (Hess et al., 2014). FDG behaves as an analogue of glucose: it is transported to a cell and converted into FDG-6-phosphate by phosphorylation. However, unlike glucose, the altered FDG molecule remains trapped in the cell. As many malignant cells consume glucose at an accelerated rate, FDG accumulates more in the malignant cells than in the normal cells, making this radiopharmaceutical an excellent marker of changes in glucose metabolism. FDG is first applied to oncology imaging, but its use is also predominant in infection, cardiology and neurology imaging. In the brain, FDG acts as an indirect marker of synaptic dysfunction and is part of the diagnosis of epilepsy and neurodegenerative diseases, such as Alzheimer's disease.

Although FDG is a non-specific tracer, other radiopharmaceuticals target specific diseases. Amyloid tracers, such as the Pittsburgh compound B (PiB) and florbetapir, which bind to fibrillar Aβ plaques, are for example used in the diagnosis of dementia syndromes.

PET imaging provides information about the functional or metabolic changes associated with a pathology but does not provide accurate anatomical information.

1.1.2 X-Ray computed tomography

X-ray imaging is built on the work of Roentgen who 'discovered the exceedingly curious fact that bone is so much less transparent to these radiations than flesh and muscle' (Nature, 1896).

When an X-ray beam passes through the body, part of its energy is absorbed or scattered: the number of X-ray photons are reduced by attenuation (Figure 1.3). On the opposite side of the body, detectors capture the remaining X-ray photons and an image is generated. In an X-ray image, the contrast, defined as the relative intensity change produced by an object, originates from the variations in linear attenuation coefficient with tissue type and density. X-ray imaging provides excellent contrast between bone, air and soft-tissue but very little contrast between the different types of soft-tissue.

Although the images produced were originally in 2D, X-ray computed tomography (CT) enables the reconstruction of 3D images by rotating the X-ray source and detectors around the body. Rather than using the absolute values of the linear attenuation coefficients, CT image intensities, or CT number, are expressed in a standard unit, the Hounsfield unit. The tissue attenuation coefficient is compared to the

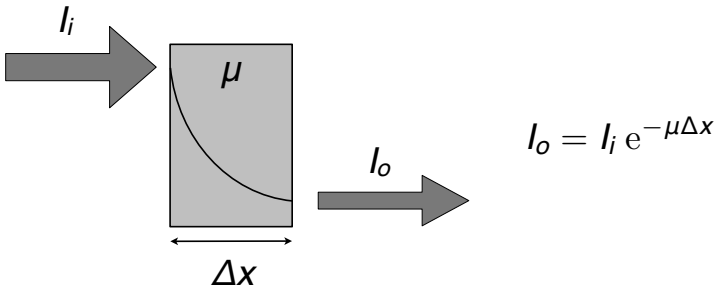

Figure 1.3: Attenuation of X-rays by matter. As it passes through a material of thickness Δx and linear attenuation coefficient μ, the x-ray beam is attenuated. Its intensity decreases exponentially with the distance travelled: $I_o = I_i\, \mathrm{e}^{-\mu \Delta x}$, where I_i and I_o are the input and output X-ray intensities.

attenuation value of water and displayed on the Hounsfield scale

$$HU = 1000 \times \frac{\mu - \mu_{water}}{\mu_{water} - \mu_{air}}$$

where μ_{water} and μ_{air} are the linear attenuation coefficients of water and air, respectively.

1.1.3 Magnetic resonance imaging

In MRI, the image is obtained by exploiting the magnetic properties of certain atomic nuclei present in the human body.

The MRI signal comes principally from the hydrogen nuclei found in the water molecules in our bodies. In the absence of a strong external magnetic field, the directions of the proton's spins are random, thus cancelling each other out. When the spins enter a strong external magnetic field (B0) they align either parallel or anti-parallel and they all precess around the B0 axis, referred to as the z axis. As a result, they cancel each other out in the transverse (x,y) plane but they add up along the z axis. The result of this vector addition, called net magnetisation M0, is proportional to the proton density (PD). With the application of the a radio frequency (RF) pulse, the system of spins and the net magnetisation are tipped by an angle determined by the strength and duration of the RF pulse. For a 90° RF pulse, the magnetisation along the z axis (Mz) becomes zero and the magnetisation in the transverse plane (Mxy) becomes equal to M0. When the RF pulse is then turned off, two phenomena occur. First, the system of spins relaxes back to its preferred energy state of being parallel with B0 in a time T1, called longitudinal or spin-lattice relaxation time, and the longitudinal magnetization Mz slowly recovers to its original magnitude M0. Second, each spin starts precessing at a frequency that is slightly different from the one of its neighbouring spins because the field of the MRI scanner is not uniform and because each spin is influenced by the small magnetic fields of the neighbouring spins. When the spins are completely dephased, they are evenly spread in the transverse plane and Mxy becomes zero. Mxy decreases at a much faster rate than that at which the Mz recovers to M0. The transverse relaxation time T2, also called spin-spin relaxation time, describes the Mxy decrease because of interferences from neighbouring spins, while T2* describes the decrease because of both spin-spin interactions and non-uniformities of the B0. Finally, the MRI signal is obtained by measuring the transverse magnetisation as an electrical current by induction.

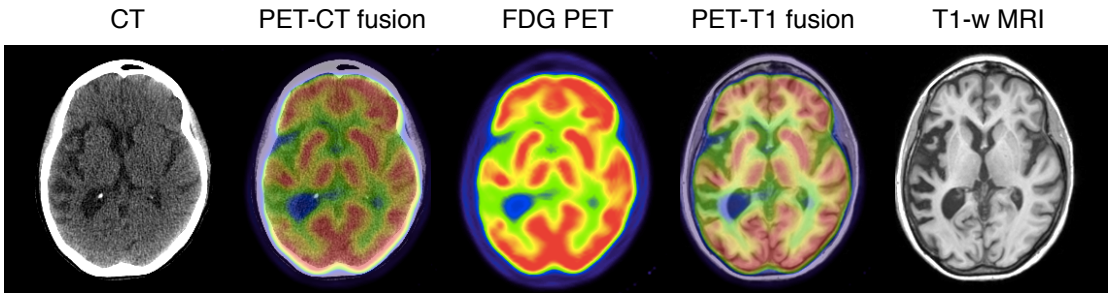

Figure 1.4: Example of PET, CT, T1-w MR and fused images

The contrast in MR images depends on three main parameters: the proton density, the longitudinal relaxation time T1, and the transverse relaxation time T2. These parameters can be adjusted by changing the time at which the signal is recorded, called echo time (TE), and the interval between successive excitation pulses, called repetition time (TR). A T1-weighted (T1-w) image is created by choosing a short TR, a T2-weighted (T2-w) image by choosing a long TE and a PD-weighted (PD-w) image by minimising both the T1 and T2 weighting of the image (long TR and short TE).

MRI provides high-resolution anatomical information and excellent contrast between soft tissues. It can also be used to study the diffusion of water molecules in tissue (diffusion MRI), analyse brain activity (functional MRI), assess relative cerebral blood flow (perfusion MRI) or provide information about tissue metabolites (MR spectroscopy).

1.2 Combining imaging modalities

PET imaging is limited by its lack of accurate anatomical information, preventing the precise localisation of areas with abnormal uptake. Furthermore, FDG, the most widely used tracer, is not specific to a disease and accumulates in various normal organs, such as the brain, heart, liver, intestines, and lungs, making the images difficult to interpret. A way to improve the interpretation of PET images and add functional information to the more structurally-oriented imaging modalities is to combined PET with CT or MR imaging. An example of PET, CT, MRI and fused images is displayed in Figure 1.4.

1.2.1 PET/CT scanners

One of the first dual-modality imaging systems combining anatomy and function, the PET/CT scanner, was introduced commercially in 2001 (Beyer et al., 2000; Townsend, 2008). The PET and CT components are integrated within a single gantry, the CT on the front and the PET at the back, and a single patient bed is used for both modalities. Co-registered functional and anatomical images can then be obtained by performing a CT study followed by a PET study on the same scanner without moving the patient. Only one visit to the hospital is necessary to acquire a complete set of anatomical and functional images and assess the status of the patient's disease. Since 2006, PET/CT systems have totally supplanted stand-alone PET scanners (Townsend, 2008).

1.2.2 PET/MR scanners

The first PET/MR images of the brain were obtained in 2006 by inserting PET detectors into an existing MRI scanner (Schlemmer et al., 2008). Four BrainPET inserts (Siemens Healthcare, Erlangen, Germany) were then installed in 2008 at Tubingen, Boston, Julich and Atlanta (Herzog et al., 2011). In 2010, two whole-body PET/MR scanners were commercially available: the Ingenuity TF PET/MR, a sequential scanner from Philips (Philips Medical Systems, Best, The Netherlands) and the mMR Biograph, a simultaneous scanner from Siemens. The simultaneous acquisition of PET and MR images generates high expectations but the technology is young and still presents some limitations.

1.2.2.1 A land of opportunities...

One of the main advantages of PET/MR scanners is the reduced radiation dose received by the patient. They also benefit from the good soft-tissue contrast and the possible uses of MRI such as functional MRI, diffusion weighted imaging or MR spectroscopy. Another advantage of combining PET and MRI in one scanner is the reduced time necessary to acquire the two modalities, which helps increasing patients' comfort. The scan time is even lower when PET and MRI are acquired simultaneously. Simultaneous PET/MR scanners do not simply incorporate two modalities into the same scanner, they combine them in a way so that each modality contributes to the enhancement of the other. The BrainPET or the mMR Biograph scanners allow the concurrent acquisition of complementary data such as structural, functional and kinetic information (Heiss, 2009). Exploiting simultaneous acquisition, new motion correction techniques are being developed. The motion field can be derived from either the PET (Manber et al., 2014) or MRI (Catana et al., 2011; Ullisch et al., 2012; Ouyang et al., 2013) data. As the two modalities are acquired simultaneously, PET and MR images are assumed to be co-registered, which can for example facilitate partial volume correction (Erlandsson et al., 2012; Hutton et al., 2013). Finally, using both PET and MRI contrast agent creates the opportunity for both input functions to be determined at the same time (Sari et al., 2015).

By combining technological innovations, PET/MR scanners open the way to new clinical applications (Catana et al., 2013). They find their first application when the radiation dose needs to be kept to a minimum, such as for paediatric subjects. Moreover, numerous examinations will benefit from the high soft-tissue contrast brought by MR imaging. Neurology studies will certainly profit from the combination of functional and anatomical imaging (Catana et al., 2012), for example to diagnose dementia. Indeed, the diagnosis of dementia is based on both MRI and PET information. Structural MR images are used to estimate atrophy while diffusion tensor imaging is used to assess white matter integrity and functional MRI to detect changes in the functional networks. Several PET tracers are used for the study of dementia (Herholz, 2014). FDG PET reflects the glucose consumption which correlates with the activity of the synapses while PiB or Florbetapir tracers are used to image the deposition of beta-amyloid plaques in the brain.

1.2.2.2 ... but fraught with pitfalls

PET/MR scanners give the opportunity to develop new technical procedures and clinical applications. However, performing PET and MRI simultaneously is a challenge (Catana et al., 2013). On one side,

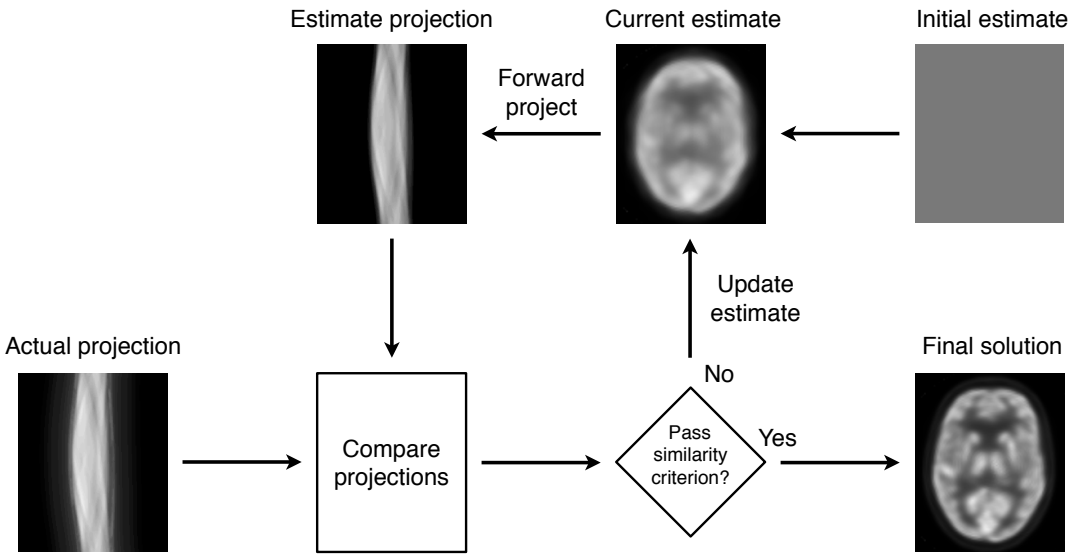

Figure 1.5: Flow diagram of an iterative reconstruction algorithm. The process starts with a simple initial image estimate. A forward projection step computes projections from the estimated image. The estimated projections are then compared with the one actually acquired, and the difference between the two is calculated as a cost function. Based on the cost function the estimated data are updated to improve the similarity between actual and estimated data.

the magnetic field causes gain changes and spatial distortions in the photomultiplier tubes (PMTs) of the PET detectors . On the other side, electromagnetic interferences produce image artefacts and decrease the signal-to-noise ratio. The PET components can also generate inhomogeneities in the magnetic field. Another challenge is the restricted space. The PET detectors have to fit in the 70 cm bore diameter of the MRI. Although many of these technical challenges have been tackled, for example by replacing the PMTs with avalanche photodiodes or silicon photomultipliers, software challenges still remain. Performing attenuation correction in a limited space and with a lack of photon density information is one of them and will be discussed in the following section and in the next chapter.

1.3 PET reconstruction

PET scanners do not measure the radiotracer distribution directly but detect the annihilation photon pairs produced from the positron emissions. A reconstruction process is necessary to recover the map of radioactivity concentration.

1.3.1 PET reconstruction algorithms

Image reconstruction consists of determining the spatial distribution of a radiotracer from the coincidence events detected by the PET scanner. Reconstruction algorithms can be divided into two main families: analytical or iterative reconstructions (Qi and Leahy, 2006; Reader and Zaidi, 2007; Tong et al., 2010). The main analytical reconstruction technique is filtered back-projection, which was historically used in clinical practice. Filtered back-projection assumes a relatively simple model of the emission and detection processes and would become complex if more advanced models were applied. This technique is also limited by the presence of artefacts. Iterative reconstruction techniques can integrate more complex models and formulate assumptions regarding the statistical properties of the acquired data. Many ap-

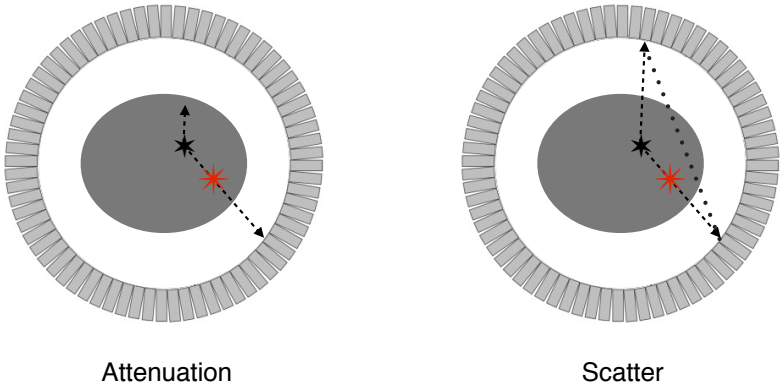

Figure 1.6: Illustration of the attenuation and scatter of photons due to Compton scattering. Photons emitted from the annihilation site (red star) interact with matter (black star) and deviate from their original path. As a consequence, they might not be detected (attenuation) or they might be detected but their annihilation site will be wrongly located (scatter).

proaches exist and can be summarised as follows (Figure 1.5). The process starts with a simple initial image estimate. A forward projection step computes projections from the estimated image. The estimated projections are then compared with the one actually acquired, and the difference between the two is calculated as a cost function. Based on the cost function the estimated data are updated to improve the similarity between actual and estimated data.

1.3.2 Attenuation and scatter corrections

To accurately quantify the radionuclide uptake, a number of correction factors need to be estimated prior to image reconstruction. The attenuation and scatter corrections are detailed below but it is also necessary to correct for random coincidences, variations in detector efficiency and count-rate losses due to dead-time (Meikle and Badawi, 2005).

1.3.2.1 Interaction of photons with matter

Compton scattering is the main interaction of 511-keV photons, emitted following annihilation between a positron and an electron, with tissue (Fig 1.1). The Compton effect leads to two phenomena: attenuation and scatter, both a consequence of the same physical process.

Photons undergoing Compton scattering will deviate from their original path (Fig 1.6). As a result, they might not be detected (attenuation) or they might still be detected but their annihilation site will be wrongly located (scatter). In order to accurately quantify the radionuclide uptake, the emission data need to be corrected for both scatter and attenuation.

1.3.2.2 Attenuation correction of PET data

The attenuation correction factor (ACF), for a specific LOR and a given attenuation map μ at location r, is defined as $ACF(LOR) = \exp(\int_{LOR} \mu(r))$. The corrected emission data can be obtained by multiplying the original projected emission data E by the ACF: $E_{corrected} = E \times ACF$. Alternatively, the attenuation correction factors can be incorporated in the iterative reconstruction (Michel et al., 1998).

Stand-alone PET scanners In stand-alone PET scanners, the attenuation information can be derived from two measurements: a blank measurement (without patient) and a transmission measurement (with

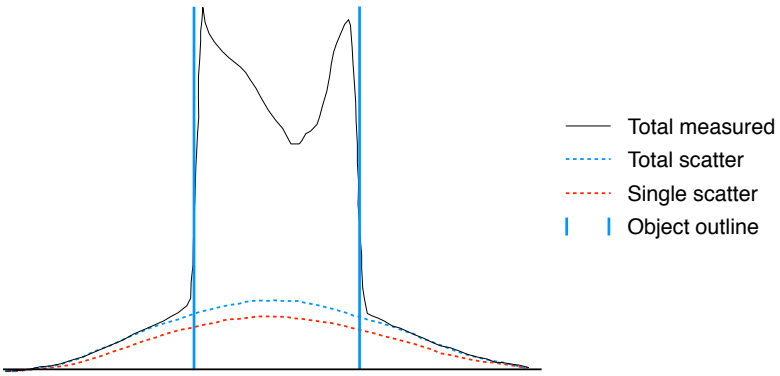

Figure 1.7: Illustration of the single scatter simulation (SSS) algorithm. Emission and attenuation information are used to model single Compton scattering. The estimated scatter is then scaled to fit the tails of the sinogram, identified from the attenuation map, where it is assumed that the signal is only coming from scattered events.

patient), obtained using one or several moving sources (either 68Ge or 137Cs). The ACF is then defined as the ratio between blank and transmission scans: $ACF(LOR) = blank/transmission$ (Ostertag et al., 1989).

PET/CT scanners In combined PET/CT systems, the attenuation information is usually derived from a CT image as the Hounsfield unit scale is a linear transformation of the linear attenuation coefficients (section 1.1.2). The CT values expressed in HU can be converted to linear attenuation coefficients in cm^{-1} by a piecewise linear transformation (Burger et al., 2002):

$$\mu = \begin{cases} \mu_{\text{water}} \left(1 + \frac{I^{CT}}{1000}\right) & I^{CT} \leq 0 \text{ HU} \\ \mu_{\text{water}} \left(1 + \frac{I^{CT}}{1000} \frac{\rho_{\text{water}}(\mu_{\text{bone}} - \mu_{\text{water}})}{\mu_{\text{water}}(\rho_{\text{bone}} - \rho_{\text{water}})}\right) & I^{CT} > 0 \text{ HU} \end{cases}$$

where μ_{water} and μ_{bone} represent the attenuation coefficients at the PET 511 keV energy for water and bone respectively and ρ_{water} and ρ_{bone} represent the attenuation coefficients at the CT energy.

PET/MR scanners Regarding PET/MR scanners, the strong magnetic field and the limited bore diameter of the MRI prevent the use of a transmission source. As MR image intensities do not reflect the electron densities, alternative methods have to be developed for the attenuation correction of PET/MR acquisitions (Bezrukov et al., 2013). These methods can be classified into four main categories: transmission, emission, segmentation, and atlas-based approaches, and will be the subject of the next chapter.

1.3.2.3 Scatter correction of PET data

Several methods exist to correct for scatter coincidences (Zaidi and Koral, 2004). They can exploit multiple energy windows, be based on convolution and deconvolution, or calculate scatter from the emission and attenuation data using a model or Monte Carlo simulation. One of the most popular approaches is the single scatter simulation (SSS) algorithm (Watson, 2000). The SSS algorithm consists of using the emission and attenuation information to model single Compton scattering. The estimated scatter is then scaled to fit the tails of the sinogram, obtained from the attenuation map, where it is assumed that the signal is only coming from scattered events (Figure 1.7).

1.4 Thesis contributions

The new technical advances brought by simultaneous PET/MR scanners are expected to open the way to new clinical applications that were not accessible with PET/CT scanners. However, for a new generation of technology to supplant the previous generation, it first needs to be its equal. This is not yet the case for PET/MR and PET/CT scanners, mainly because of the limitations caused by the imperfect attenuation correction. The main weakness of the MR-based attenuation correction methods is the lack of accuracy of the bone delineation as both bone and air have similar low intensities in most MR images. However, these inaccuracies lead to a strong spatial bias of the PET activity, particularly in the brain, as shown in Andersen et al. (2014) and Dickson et al. (2014). My first objective is to develop a new method to improve attenuation correction of PET/MR data in the brain.

Abnormalities in cerebral glucose metabolism detectable on FDG PET can be assessed on a regional or voxel-wise basis. In regional analysis, the average relative uptake over a region of interest is compared with the average relative uptake obtained for normal controls. Prior knowledge is required to determine the regions where abnormal uptake is expected, which can limit its usability. On the other hand, voxel-wise analysis consists of comparing the metabolic activity of the patient to the normal controls voxel-by-voxel, usually in a groupwise space. Voxel-based techniques are limited by the inter-subject morphological and metabolic variability in the normal population, which can limit their sensitivity. My second objective is to develop a new framework for the analysis of FDG PET images, exploiting both the subject's MRI and PET data, able to improve the delineation of disease-specific metabolic patterns.

Attenuation correction is not the only domain where the lack of electron density information of MR images is a problem. In radiotherapy, the optimal dose distribution for treating a tumour is determined according to the attenuation properties of the different tissues, which explains why most radiotherapy treatments are planned using a CT scan of the patient. However, CT images have low soft tissue contrast, which can lead to large variations when delineating the tumour, particularly when located in the brain, head & neck, or prostate. Instead, the excellent soft-tissue contrast of MR images could be exploited to more accurately delineate the tumour and organs at risk. However, the tissue attenuation properties are not easily estimated from MRI data, which limits the development of MR-based radiotherapy treatment planning. My third objective is to develop a new method to derive tissue attenuation properties from MR images in the head & neck and pelvic regions to facilitate MR-based radiotherapy treatment planning.

The contributions of this thesis include the following:

- To improve the attenuation correction of PET/MR data in the brain, I propose a new method to synthesise CT images from T1-weighted MR images. The method was inspired by the label-fusion techniques used for segmentation. In these techniques, a set of anatomical images from several subjects, and their corresponding labels, are mapped to a target subject. The labels are subsequently fused according to the similarity between the mapped and the target anatomical images (Heckemann et al., 2006; Sabuncu et al., 2010; Cardoso et al., 2012). For attenuation correction purposes, instead of propagating labels, CT image intensities are propagated to synthesise what

will be called in the following a pseudo CT. This pseudo CT is then used to derive an attenuation map, as described in section 1.3.2.2.

- As we will see in more detail in the next chapter, obtaining attenuation information from PET/MR data is challenging. Several authors have quantified the effect of an imprecise attenuation map on the reconstructed PET image but its influence on scatter correction has usually been ignored. I propose to investigate the effects of imperfect attenuation maps on the scatter correction and assess the importance of re-evaluating scatter when comparing MR-based attenuation maps to the reference CT attenuation map.

- The multi-atlas CT synthesis method proposed strongly depends on a database of MR and CT image pairs. I investigate if an optimal number of subjects in the database exists and if demographic characteristics such as the subjects gender and age have an influence on the accuracy of the pseudo CT generated.

- To make the CT synthesis approach more flexible, I extend the method, first to other MRI contrasts, and then to multi-contrast MR images by combining different MRI sequences.

- The CT and attenuation map synthesis method, both from single and multi-contrast MR images, is evaluated on two different PET tracers (FDG and Florbetapir). The PET reconstruction accuracy is assessed, for both tracers, by comparing the reference PET images, corrected for attenuation using the CT-based μ-map, to the PET images corrected using the proposed method.

- I propose a novel framework for the analysis of FDG PET data that consists of creating a subject-specific healthy PET atlas. The analysis is done in the original subject space and provides voxel-by-voxel statistics of normality/abnormality.

- Finally, I redesign the synthesis process and present an iterative multi-atlas algorithm to synthesise CT images in the neck and pelvic regions. I show that the application of the CT synthesis method is not limited to PET/MR attenuation correction and that pseudo CTs can also be useful for MR-based radiotherapy treatment planning.

1.5 Thesis organisation

Attenuation correction methods developed from PET/MR scanners can be classified into four main categories: transmission-, emission-, segmentation-, and atlas-based approaches. The next chapter reviews the main methods in each category. In chapter 3, I describe how pseudo CTs are synthesised from a single T1-weighted MR image using a database of pre-acquired MR and CT image pairs. In chapter 4, I evaluate how an imprecise attenuation map might affect scatter correction. Chapter 5 focuses on the optimal way to build the MR-CT database used to synthesise pseudo CTs. In chapter 6, a novel similarity measure is proposed to improve the CT synthesis accuracy and the method is extended to other MRI contrasts (T2-weighted and LAVA-Flex). In chapter 7, the CT synthesis method is further extended to multi-contrast MR images. Chapter 8 presents a validation of the multi-atlas, multi-contast CT synthesis on two PET tracers (FDG and Florbetapir). Chapter 9 describes a new framework for the analysis of FDG PET data that consists of generating a subject-specific PET model. In chapter 10, I redesign the CT synthesis method to generate pseudo CTs in the neck and pelvic regions and show that the method is not restricted to PET/MR attenuation correction but can be applied to MR-based radiotherapy treatment planning. Finally, chapter 11 concludes this thesis and outlines potential future research directions.

Chapter 2

Attenuation correction for PET/MR scanners

Before the emergence of PET/CT scanners, attenuation correction was mostly based on transmission measurements. However, because of the restricted space and the strong magnetic field, installing a rotating radiation source in a PET/MR scanner is challenging. With PET/CT systems, the attenuation coefficients are derived from CT scans. However, in contrast with CT images, MR image intensities do not directly provide information about the tissue attenuation properties. For these reasons, alternative methods are being developed for the attenuation correction of PET/MR acquisitions. These methods can be classified into four main categories: transmission-, emission-, segmentation-, and atlas-based approaches. This chapter will describe the main methods developed in each category. Tables summarising the different approaches are available at the end of the chapter (Tables 2.1, 2.2, 2.3, 2.4 and 2.6).

2.1 Transmission-based approaches

The first class of methods focuses on the design of new transmission sources as an alternative to the rotating sources.

2.1.1 Simultaneous emission and transmission measurements

Simultaneous measurement of emission and transmission is not a new technique (Meikle et al., 1995), but to adapt to the limited bore size and the strong magnetic field of PET/MR scanners, new transmission sources need to be developed. Mollet et al. (2012) proposed to use a thin annulus-shaped source covering the whole field of view (FOV) of the scanner, which contains a positron-emitting isotope. Emission and transmission data are acquired simultaneously, and a TOF-based classification method is used to separate transmission data from emission data. Evaluating their method on 5 subjects, Mollet et al. (2014) demonstrated that an annulus-shaped transmission source could be used to estimate the attenuation map in TOF PET/MR systems. Another alternative to the rotating sources could be to use a sparse transmission system (Watson et al., 2014).

2.1.2 Combination of transmission measurement and tissue segmentation

Kawaguchi et al. (2014) proposed an attenuation estimation method using a non-rotational radiation source and a segmented tissue map. Attenuation coefficients were computed, for each tissue class segmented from an anatomical MRI, from a blank scan, a transmission scan, and the partial path length of each tissue calculated from a virtual blank scan and the segmented MRI.

2.2 Emission-based approaches

The second class of methods exploits information in the PET emission data to estimate the attenuation maps. These methods exploit the fact that the emission data contain information both about the distribution of the activity and the attenuation within the body, and thus aim at simultaneously calculating the attenuation and activity coefficients.

2.2.1 Joint estimation of emission and attenuation

Joint estimation without TOF In one of the first works published on this topic, Censor et al. (1979) calculated the attenuation and activity coefficients from the emission data using an iterative process based on the system of non-linear equations describing the model of gamma-ray emission. Nuyts et al. (1999) later built on this idea and developed the maximum-likelihood reconstruction of activity and attenuation (MLAA) algorithm which takes into account the Poisson nature of the emission data. The method is based on the likelihood optimisation but also incorporates simple a priori knowledge about the attenuation coefficients in the human body. As the solution of the simultaneous estimation is not unique in the absence of prior information (Natterer and Herzog, 1992), the success of these methods is limited. The coupling of activity and attenuation also creates cross-talk problems, where localised errors in the activity image are compensated by localised errors in the attenuation image (Rezaei et al., 2012).

Joint estimation with TOF Defrise et al. (2012) showed that with TOF information, the joint estimation of attenuation and activity from the emission data has a unique solution except for a constant. Based on this result, Rezaei et al. (2012) applied the MLAA algorithm (Nuyts et al., 1999) to TOF-PET. They showed that TOF information can eliminate the problem of activity and attenuation cross-talk but that, because the solution is only determined up to a scaling constant, some prior knowledge is still required. Instead of maximising the data likelihood with respect to the activity and attenuation images, Rezaei et al. (2014) and Defrise et al. (2014) proposed to maximise the data likelihood with respect to the activity image and the attenuation sinogram, defined as the set of attenuation factors for all LORs. This method, called maximum likelihood reconstruction of activity and attenuation correction factors (MLACF), avoids the reconstruction of the attenuation image but requires some prior knowledge about the activity or the attenuation factors. Under ideal conditions, the evaluation on simulated and measured data of both the MLAA and MLACF approaches showed promising results. Recently, Li et al. (2015) developed a new way to estimate the attenuation using histo-images created from the TOF-PET emission data.

Joint estimation using scattered coincidences As an alternative to using the extra information provided by TOF systems to simultaneously estimate the activity and attenuation from the emission data, Berker et al. (2014) exploited additional information from scattered coincidences.

2.2.2 Joint estimation using anatomical priors

In the context of PET/MR scanners, the joint reconstruction of emission and attenuation can be regularised using anatomical information from MR images. In the work of Salomon et al. (2011), the attenuation estimation is initialised by assigning the attenuation coefficients of water to the segmented

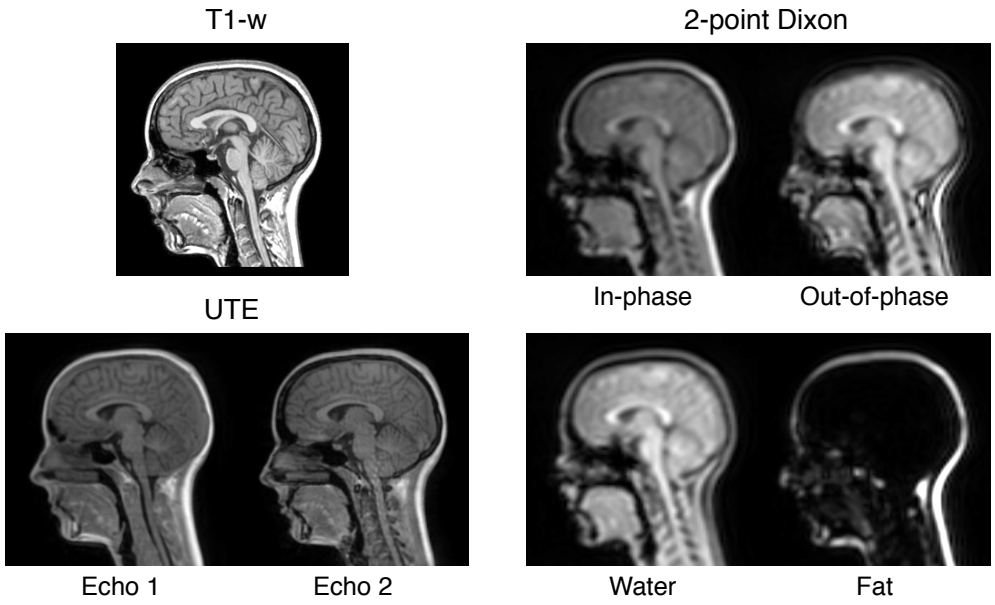

Figure 2.1: Example of MRI sequences used to derive attenuation maps. Top left: T1-weighted. Bottom left: ultrashort echo time (UTE). Right: 2-point Dixon.

MR image and the activity estimation is constrained using TOF information. Mehranian and Zaidi (2015) pushed this idea further and improved the initial attenuation map by segmenting the MR image into four classes using a Gaussian mixture model and by adding bone information obtained from a co-registered average CT. Benoit et al. (2015) modified the existing non-TOF MLAA technique and used a segmentation-based attenuation map together with a T1-weighted MR image as prior information.

2.3 Segmentation-based approaches

In segmentation-based methods, predefined or subject-specific attenuation coefficients are assigned to tissue classes obtained by segmenting one or several MR images.

2.3.1 Segmentation methods ignoring bone

Several MRI sequences can be used as an input for segmentation techniques. Martinez-Möller et al. (2009) used a 2-point Dixon sequence to segment the body into four classes: background, lungs, fat and soft-tissues. The Dixon method exploits the fact that water and fat protons have slightly different resonance frequencies. By acquiring images when their spins are in- and out-of-phase with each other, water and fat images can be derived (Dixon, 1984). An example of Dixon images is displayed in Figure 2.1. In the work from Martinez-Möller et al. (2009), a threshold was applied to the water and fat images to separate soft-tissue and fat from the background. Connected-component analysis of the air in the inner part of the body was used to define the lung class. The tissue/air classification was refined using a morphologic closing filter.

Schulz et al. (2011) based their 3-class (air, soft-tissue and lung) segmentation method on a T1-w sequence, often acquired as part of clinical protocols. The body was first extracted from the background using slice-wise region growing with an automatically determined threshold, and another region growing was performed to segment the lungs.

Instead of segmenting MR images, Chang et al. (2013) investigated the use of non attenuation corrected (NAC)-PET images. The 3-class segmentation consists of segmenting the NAC-PET to derive a first attenuation map, using this map to correct the raw PET data for attenuation, and refining the segmentation using the newly reconstructed PET image. This process is repeated to first segment the body contour, then segment the lungs, and finally refine the lung segmentation.

While the results obtained with these methods in whole-body studies are satisfactory, the lack of bone information has a significant impact on the quantification of the radionuclide uptake in brain studies (Schleyer et al., 2010).

2.3.2 Segmentation methods including bone

Several methods aim at extracting a bone class from different MRI sequences, such as T1-w, Dixon and ultrashort echo time (UTE), or a combination of sequences.

From a T1-weighted MRI sequence Segmenting MR images for attenuation correction was already a topic of interest in the Nineties. Le Goff-Rougetet et al. (1994) segmented brain T1-w MR images based on thresholding and mathematical morphology tools to simplify the acquisition protocol and reduce the dose received by the patient. With the same objective, Zaidi et al. (2003) proposed to apply a fuzzy c-means (FCM) algorithm on the T1-w spin-echo images to segment air, brain tissue, skull, nasal sinuses, and scalp. Some manual intervention of the operator was required to refine the segmentation of the skull.

The knowledge-based segmentation approach developed by Wagenknecht et al. (2009) consisted of three steps. First, tissues were segmented using a supervised neural network-based classification. The brain and extracerebral region were then separated based on anatomical knowledge: it is known that the brain soft-tissue is surrounded by cerebrospinal fluid (CSF) which is in turn surrounded by the extracerebral region, while the extracerebral region is surrounded by the background region. Anatomical knowledge is finally used to segment the extracerebral region into the mastoid process, craniofacial cavities, bone, and soft-tissue, based for example on the fact that air-filled cavities are compact and connected by small junctions, while bone regions are narrow and elongated.

Instead of segmenting the skull in image space, Yang and Fei (2013) proposed a skull segmentation method for T1-w MR images via a multiscale bilateral filtering processing of MRI sinogram data in the Radon domain. This segmentation method, combined with a multiscale FCM approach to classify the other tissues, was integrated into the PET/MR quantification tools developed by Fei et al. (2012).

From T1-weighted and Dixon sequences Exploiting multiple MRI sequences, Anazodo et al. (2015) proposed to overlay a bone mask to the attenuation map obtained from the segmentation of Dixon images (Martinez-Möller et al., 2009). The bone mask is created by segmenting the T1-w magnetisation-prepared rapid gradient-echo (MPRAGE) image using the new segment function in SPM (Ashburner and Friston, 2005) and International Consortium for Brain Mapping (ICBM) Tissue Probabilistic Atlases.

From UTE sequences The low signal intensity of cortical bone in both T1-w and Dixon images makes the distinction of bone and air difficult, which is a major issue as they have very different attenuation coefficients. However, with UTE sequences, cortical bone can have a high signal on an image despite its very short spin-spin relaxation time (T2) (Robson et al., 2003).

Keereman et al. (2010) exploited this property and used UTE images as the input of their segmentation strategy. However, instead of directly segmenting a single UTE image, they proposed to acquire two images UTE_1 and UTE_2 at different echo times, TE_1 and TE_2 respectively, such that the bone signal is present in UTE_1 but not in UTE_2, while the signals from other tissues are similar in both images. See Figure 2.1 for an example of dual UTE images. From these two images, they calculated for each voxel the R2* value, which is the inverse of the T2* relaxation time, as follows: $R2^* = \frac{\ln UTE_1 - \ln UTE_2}{TE_2 - TE_1}$. It was then possible to distinguish between cortical bone, which is expected to have high R2* values, from soft-tissue, expected to have low R2* values. The distinction between air and tissue is however more difficult because of possible artefacts or noise in the UTE images. To overcome this problem, a binary air mask was created from the first-echo image (UTE_1) and applied to the R2* map. Finally, the corrected R2* map was segmented into three tissue classes (bone, soft-tissue and air) using thresholds and converted to attenuation map by assigning fixed linear attenuation coefficients to each tissue class. This approach can be improved by correcting for Eddy current artefacts in the UTE images by measuring the true k-space trajectories during a calibration scan and using them in subsequent image reconstructions (Aitken et al., 2014). Refinements for the R2* map segmentation were later proposed by Cabello et al. (2015).

Catana et al. (2010) also based their 3-class (bone, soft-tissue and air) segmentation strategy on dual UTE images but proposed an alternative to the R2* map. A head mask was first obtained by applying a morphologic closing operation to the UTE_2 image. Bone tissue was segmented from a combination of the two UTE images $\left(\frac{UTE_1 - UTE_2}{{UTE_2}^2}\right)$ using an empirically determined threshold. The air cavities were segmented in the same way but from another combination of the UTE images $\left(\frac{UTE_1 + UTE_2}{{UTE_1}^2}\right)$. Finally, the voxels included in the head mask that were not identified as bone or air were classified as soft-tissue.

As an alternative to the UTE sequence, Wiesinger et al. (2016) explored PD-weighted, 'zero' TE imaging to delineate bone.

From UTE and Dixon sequences Combining cortical bone segmentation and water-fat decomposition, Berker et al. (2012) proposed a 4-class (bone, soft-tissue, fat and air) segmentation technique using a UTE triple-echo sequence. The combination of the first and third echoes, both in-phase, is used to segment cortical bone, while the combination of the second echo, out-of-phase, with the in-phase echoes enables the separation of the fat and water signals and the calculation of the water-fat fraction. Bone was then segmented using an empirically determined threshold and was assigned a predefined linear attenuation coefficient, while the attenuation coefficient for each mixed water-fat voxel was calculated from the relative water-fat fraction and tissue-specific attenuation coefficients.

Hsu et al. (2013) proposed to apply an FCM algorithm to segment a set of MR images (T1-w, T2-w, Dixon and UTE) into five tissue classes (fluid, fat, white matter, grey matter and bone). The pseudo CT was generated by assigning relative attenuation coefficients with weights based on the probability that each class exists at a given location.

Su et al. (2015) followed a similar idea but reduced the inputs to a single acquisition UTE-mDixon sequence. The three images derived from this sequence (fat, water and R2*) were used as inputs for an FCM algorithm aiming at identifying five clusters (air, brain, fat, fluid, and bone). The attenuation map

was finally created assuming that each voxel represents a mixture of the different tissue types.

Instead of the UTE sequence, Khateri et al. (2015) proposed to use a short echo time sequence, combined with a Dixon sequence, to segment the head in four tissue classes using FCM clustering.

2.3.3 Segmentation methods with subject-specific bone attenuation coefficients

In the segmentation-based methods presented in the previous section, predefined linear attenuation coefficients were assigned to the different tissue classes, which may limit their accuracy as the variability in attenuation coefficients between the subjects is not taken into account. This is particularly important in the bone region as it is known that several factors can affect the bone density (Fehily et al., 1992; Schulte-Geers et al., 2011). To overcome this limitation, several groups explored the possible existence of a mapping between the CT HU and the R2* values in the bone region. If the ability of CT imaging to determine bone mineral content has been known for a long time (Reich et al., 1976), recent studies showed that MR imaging could also provide some useful information. Horch et al. (2010) were able to show using the UTE sequence that the water bound to the collagen in cortical bone (higher density) has a shorter spin-spin relaxation time T2 than the water present in the porous regions of cortical bone (lower density). As T2* includes T2 relaxation (see section 1.1.3), it is expected that changes in R2* values (R2* = 1/T2*) would reflect changes in bone density.

Juttukonda et al. (2015) acquired dual UTE and Dixon sequences from which they derived R2*, fat, water, and UTE_1 images used to segment bone, fat, soft-tissue, and air, respectively, based on simple thresholding. Predefined LAC were then assigned to the air, fat and soft-tissues classes while tissues classified as bone were converted to HU using a regression model between the R2* values and HU. Several steps were necessary to obtain this model. First, the CT and R2* images of several subjects were aligned and bone was segmented in both modalities using thresholds. To reduce the noise, the R2* values were divided into bins. The mean R2* values and HU were then computed and plotted for each bin. Finally, a sigmoid model was fitted to the data.

Ladefoged et al. (2015) also acquired and used UTE images to extract a continuous bone signal for each patient and map R2* values to HU. The model was however different as a third order polynomial was fitted instead of a sigmoid. This could be explained by the lower threshold chosen for included bone and the different formula used to compute the R2* map. In addition to the R2* to HU mapping, they proposed to improve the attenuation map generation using regional masks to separately treat complex areas with mixed air and tissue. These regional masks, defined on an atlas, were transported into to subject's space and used, in combination with the R2* values, to assign predefined attenuation coefficients to the frontal sinus, nasal septa and ethmoidal sinus, mastoid process, and skull base.

Other sequences such as the water- and fat-suppressed proton projection imaging (WASPI) sequence (Huang et al., 2015) could be used to map MR to CT intensities.

2.4 Atlas-based approaches

In atlas-based methods, an anatomical model or dataset can either be deformed to match the subject's anatomy using non-rigid registration, or be used to map the subject's MR image intensities to CT HU through regression.

2.4.1 Single-atlas approaches

Montandon and Zaidi (2005) proposed to use an atlas formed of an emission and transmission pair, and preliminary PET reconstructions of the subject's brain images to construct the subject-specific attenuation map. The PET-transmission atlas was obtained by averaging the pre-aligned PET and transmission images of normal subjects mapped in a common space. To create the subject-specific transmission image, the PET atlas was registered to a preliminary PET image of the subject, reconstructed after attenuation correction using a uniform fit-ellipse based method (Weinzapfel and Hutchins, 2001), and the same transformation was applied to the transmission atlas.

Kops and Herzog (2007) developed a similar approach but registered MR images instead of the PET images to map the atlas space to the subject's space. To build the transmission-MRI atlas, the transmission and MR images of normal volunteers were spatially normalised and averaged using SPM2. To create the subject-specific transmission image, the subject's MR image was first manually aligned to the subject's PET image. The MRI atlas was then registered to the subject's MR image, now aligned to the PET image, and the same transformation was applied to the transmission atlas. With this method, it is possible to take into account morphological differences related to gender using female and male templates (Kops and Herzog, 2008).

Schreibmann et al. (2010) developed a multimodality optical flow deformable model mapping a representative CT template directly to the subject's MR image, thus generating a simulated CT image that matches the patient's anatomy.

Dowling et al. (2012) proposed to generate a subject-specific pseudo CT image by registering an MRI atlas, result of a groupwise registration, to the subject's MR image and applying the same transformation to a CT atlas aligned to the MRI atlas.

Izquierdo-Garcia et al. (2014) proposed to generate attenuation maps using the SPM8 software. The initial step of the method consists of creating MRI and CT atlases. To do so, T1-w MR images were first segmented into six tissue classes (grey matter, white matter, cerebrospinal fluid, bone, soft-tissue, and air) using SPM. The 22 segmented images were then non-rigidly co-registered using Dartel (Ashburner, 2007) to form the MRI atlas. The same transformations were applied to the CT images, previously affinely aligned with the T1-w images, and the CT atlas was created by averaging the 22 co-registered CT images. To generate a pseudo CT, the patient's MR image was segmented into six tissue classes and non-rigidly registered to the MRI atlas. The associated CT atlas was finally mapped into the patient's space by applying the inverse transformation.

2.4.2 Multi-atlas approaches

The methods described in the previous section rely on a single atlas or template and strongly depend on the accuracy of the mapping between the atlas and subject spaces and on the representativeness of the atlas. A possible solution to improve the representativeness of the atlas and limit the consequences of mis-registrations is to use multiple atlases.

The multi-atlas methods reported below rely on a database of CT and MRI pairs. Each pair is created by rigidly registering the CT and MR images of a subject. To generate a pseudo CT from the subject's MR image, the MR images from the database are non-rigidly registered to the subject's MRI. The CTs in the database are then mapped to the target subject using the transformation that maps the subject's corresponding MRI in the atlas database to the subject's MRI. A final step consists of fusing the deformed CT images.

To fuse the deformed CTs, Sjölund et al. (2015) proposed an iterative registration to the mean. The consistency of the deformed CTs is improved by iteratively forming their voxelwise mean, registering each deformed CT to the mean, and creating a new mean estimate. However, it appeared that better results were reached by directly taking the voxelwise median of the deformed CTs.

Merida et al. (2015) looked at the probability of a voxel in the subject space to belong to a certain tissue class. Three tissue classes (air, soft-tissue and bone) were defined by intensity thresholding the deformed CTs. The intensity value of the pseudo CT was determined by averaging for each voxel the CT intensities of the atlases belonging to the maximum probability class.

2.4.3 Patch-based approaches

In contrast with the single- and multi-atlas approaches, patch-based methods do not require an accurate alignment between the atlases and the target, meaning that non-rigid registration is not needed. The use of patches is also motivated by the fact that the neighbouring voxels surrounding a voxel of interest may contain useful information that could help find similarities between atlases and target.

Roy et al. (2014) used intensity normalised dual UTE images and CT images to form their training dataset. For each voxel in the training images, 3D overlapping patches were extracted and stacked into 1D vectors. The MR feature vector of a certain voxel was obtained by concatenation of the two UTE patches while the CT feature vector corresponds to the CT patch. Similar patches were defined in the target MR images. The proposed method is based on the assumption that if the target and training MR patches have similar intensities, they probably originate from the same distribution of tissues, meaning that the corresponding CT patch in the training dataset could be an approximation of the subject CT patch. As the training patches might not be representative enough of the target patches, the authors considered combinations of pairs of training patches and constructed a probability distribution with each interpolated pair acting as the mean of a component of a Gaussian mixture model. They further assumed that the target CT patch was a random vector whose mean was also a combination of training CT patches with the same weighting coefficients as those that generated the MR patches. The probability of observing the target patches was then obtained using expectation-maximisation. The estimated target CT patch was thus defined as the weighted average of the combinations of training CT patch-pairs with the

weights depending on the similarity between the MR target and training patches, as well as the similarity between the estimated target CT and training CT patches.

In the method developed by Andreasen et al. (2015), the training dataset was formed of co-registered T1-w MR and CT images. 3D patches were defined for all the voxels in the MR and CT training images thus creating a database of MR and CT patches. The target pseudo CT was predicted by extracting patches from its MR image and running an intensity-based nearest neighbour search in the patch database. The K patches minimising the squared L^2-norm between the target and training MR patches were identified and the corresponding CT patches were used in a similarity-weighted average to compute the pseudo CT. A similar approach was proposed by Torrado-Carvajal et al. (2016) and implemented on GPU.

Huynh et al. (2016) also used co-registered T1-w MR and CT images to create their training dataset. In the training stage of the method, multi-scale features were extracted from each MR image and used with the corresponding CT image to train an initial structured random forest. The resulting forest was then used to predict the CT image for each MR image in the training set, leading to an initial set of predictions. Together with the features from the MR images, context features were extracted from the predicted CT images to train a new structured random forest and perform prediction again. A sequence of trained forests was obtained by repeating this process until convergence. In the testing stage, features were extracted from the target MR image and fed into the trained forests to predict the pseudo CT.

Wu et al. (2015) proposed to predict pseudo CT from T1-w and/or T2-w MR images based on local sparse correspondence combination. The authors assumed that MR and CT patches were located on two different non-linear manifolds and that the mapping from the MR manifold to the CT manifold approximated a diffeomorphism under a local constraint. Four steps were used to reinforce the local constraint. First, for each patch in the target MR image, a local search window was defined to extract the MR and CT training patches. Second, the k-nearest neighbour (kNN) algorithm was used to strengthen the locality of the MR training dataset. Third, to guarantee the locality in the CT training dataset, k-means clustering and kNN were combined to detect outliers. The corresponding patches in the MR training dataset were then deleted, generating a new MR training dataset. Finally, local anchor embedding was performed to find the coefficients corresponding to the contribution of a particular MR training patch in representing a target patch. Once obtained, these coefficients were locally and linearly transferred from the MR manifold to the CT manifold, and used to combine the patches in the CT training dataset to generate a target CT patch. The final pseudo CT was obtained by taking the weighted average of the overlapping CT patches at each voxel.

2.4.4 Supervised learning approaches

As no model mapping MR image intensities and CT HU can be derived from the physics of magnetic resonance and X-Ray imaging, several groups proposed to use supervised learning approaches to learn input-output mappings from a training dataset.

Johansson et al. (2011) chose a Gaussian process method to solve the regression problem (Rasmussen and Williams, 2006). Two dual UTE sequences with different flip angles, a T2-w 3D spin echo

sequence and a CT were acquired for five patients to build the training dataset. The MRI sequences were chosen to best distinguish between tissues. To increase the number of input variables, two new images were derived per MR image by calculating for each voxel its local mean and standard deviation. All the MR images and the CT image were co-registered and a mask excluding the background voxels was generated. A Gaussian mixture regression model was then defined to link the MR and CT image intensities of the training dataset. For a new patient, the pseudo CT was generated by calculating for each voxel the conditional expectation for the CT value given the set of observed MR intensities. The model was later extended to include the spatial position of each voxel inside the head (Johansson et al., 2013).

Navalpakkam et al. (2013) chose another supervised learning approach, the ε-insensitive support vector regression (ε-SVR) (Vapnik, 2000). The method required the acquisition of a dual UTE sequence and a 2-point Dixon sequence, for both training and testing, and a CT image for training. To exclude air voxels from the prediction, an air mask was segmented from the UTE_1 image, and in-phase and out-of-phase Dixon images. The model was trained using this air mask, the difference map obtained from the UTE images ($\ln \mathrm{UTE}_1 - \ln \mathrm{UTE}_2$), the fat and water images derived from the in-phase and out-of-phase Dixon images, and the CT image. All the images were previously co-registered. The model generation consisted of learning the mapping between some feature vectors extracted from the MR data and their corresponding CT HU. The features included the mean, median, variance, and maximum and minimum values across a local neighbourhood computed from the difference maps, and water and fat images. For a new subject, the trained ε-SVR model was used to predict a pseudo CT from the subject's air mask, difference map, and fat and water images.

2.4.5 Combination of atlas and regression approaches

To increase the accuracy of the CT estimation, several groups proposed to combine multi-atlas and regression approaches.

In the method developed by Hofmann et al. (2008), local information derived from a supervised learning technique and global information obtained from multi-atlas registration were combined to predict a pseudo CT image: multi-atlas registration was used as prior knowledge for a Gaussian process regression. The global step of the method consisted of non-rigidly registering the MR images from the training dataset to the target's MR image and applying the same transformations to the corresponding CT images in the training dataset. The local step aimed at determining a mapping between MR image patches centred at a voxel of interest and the real CT HU values using Gaussian process regression. Training pairs comprising the position of the voxel in the target coordinate system and the patch surrounding it were extracted from the deformed images in the training dataset. Prior knowledge from the atlas registration was included by setting the mean function of the Gaussian process to the average value of the registered CT images. For an unseen patch, Gaussian process regression returned a Gaussian-distributed predictive distribution for the mapping of the MR patches to the CT HU. Finally, to predict a pseudo CT image for a new patient, for each voxel of the MR image a surrounding patch was extracted and the mean of the Gaussian-distributed predictive distribution was defined as the estimated CT value. The method was also adapted to whole-body attenuation correction (Hofmann et al., 2011).

A similar approach combining intensity and geometry information into a unifying probabilistic Bayesian framework was proposed by Gudur et al. (2014).

The method developed by Chen et al. (2015) relies on a database of co-registered T1-w MR images, CT images and air masks segmented from the CT images using k-means clustering. Pseudo CT generation required three steps. First, each atlas was non-rigidly registered to the target. A probabilistic air mask was then computed as the percentage of the aligned CT atlases that labelled a voxel as air, and refined using a hidden Markov random field segmentation on the T1-w MR image. Each voxel labelled as air was assigned the mean value of the atlas CTs belonging to the air mask. For the rest of the tissues, small neighbourhoods centred around each voxel were defined in the target. Patches of the same size were defined in the atlases in the vicinity of the central voxel. Sparse regression was then used to select the most similar patches, in terms of intensity, among all the atlas patches within the search window. Finally, the sparse coefficients were applied to combine the atlas CTs and generate the pseudo CT.

2.5 Hybrid approaches combining segmentation and use of an atlas

The methods described in this last category combine both image segmentation and atlas techniques.

Bezrukov et al. (2013) proposed a method combining segmentation, multi-atlas and supervised learning techniques, which relied on the subject's Dixon images and on an atlas database. Each atlas comprised a 5-tissue class segmentation (outer air, lung, fat tissue, non-fat tissue, and fat/non-fat tissue mix), a map of potential artefact locations extracted from regions with low MR intensity and differentiated into air-filled regions not part of the lungs and soft-tissue regions, a CT image, and a bone location map. After segmentation of the subject's MR image into five tissue classes, the segmented MR images from the atlas database were registered to the subject's image and the resulting transformations were applied to the images forming the atlases. A subject-specific map of potential artefact locations was created by averaging the atlas artefact maps. This map was used to classify the low MR intensity regions as inside air or soft-tissue masked by artefacts. Predefined LACs were assigned to the segmented regions of the MR image to create an intermediate attenuation map ($\mu\text{map}_{\text{SEG}}$). For the prediction of bone tissue, a map of potential bone locations was created from the atlas CT images by combining the individual bone location maps. This map determined the areas where Gaussian process regression was applied. For each voxel within these areas, a pseudo CT value was computed from the CT atlases and converted to LAC using a piecewise linear transformation. The final attenuation map was created by augmenting the intermediate attenuation map $\mu\text{map}_{\text{SEG}}$ with the predicted bone LACs.

Combining the segmentation of an MR image and the use of a CT image database, Marshall et al. (2013) proposed a method where the subject's MR image was compared to the database of CT images using a set of 19 similarity metrics such as gender, age, and body, lung and bone geometries. The most similar CT image was selected and non-rigidly aligned to the subject's MR image. Bones from the registered CT image were then added to the MR image previously segmented into four tissue classes (air, lung, fat and lean tissue).

Poynton et al. (2014) proposed an approach for deriving attenuation maps from UTE and T1-w images by combining segmentation and atlas-based techniques. CT images from several subjects, aligned

in a common space, were segmented into bone, soft-tissue and air to produce three binary label maps. Maximum likelihood estimates were obtained from the binary label maps to produce an atlas containing the probability of air, soft-tissue, and bone at each voxel. This probability atlas was then combined with the MR and CT data to train a classifier calculating the probability of each class at each voxel. The MR data were composed of a T1-w image and two images derived from the UTE images enhancing signal from bone and air voxels. This classifier was finally applied to segment the MR images of a new subject.

The method developed by Paulus et al. (2015) was based on a regular 4-class segmentation from a Dixon sequence and atlas-based bone segmentation algorithm. The atlas was composed of pairs of pre-aligned MR image and bone mask (containing bone densities) for each major bone in the body, including left and right upper femur, left and right hip, spine, and skull. To generate a subject-specific attenuation map, the subject's Dixon images were first segmented into four classes (air, lung, soft-tissue and fat). The bone class was then added by registering the MR model to the subject for each bone individually and applying the same transformation to the bone mask. The method was then validated in the brain region (Koesters et al., 2016).

2.6 Discussion

Although using transmission measurements was one of the first solutions to correct for attenuation PET data, their use for PET/MR systems is not established and finding an optimal design is still an open research topic. Using a transmission source would also increase the dose received by the patient, which would diminish the benefits of using PET/MR scanners, particularly for paediatric patients.

Emission methods were also being developed before the emergence of the PET/MR technology. Improvements in computational performance and the easy access to anatomical priors have made them very promising. As these methods mostly rely on the emission data, no task-specific MRI sequence needs to be acquired, also meaning that their sensitivity to artefacts in the MR images is limited. However, more validation on patients is required to fully assess their capabilities to accurately correct for attenuation PET data. Finally, most of these methods require TOF information, not available on all PET/MR systems, which limits their usability.

Segmentation-based methods essentially rely on the subject's MR images. The first methods available for attenuation correction on commercial PET/MR scanners were either based on a Dixon sequence, leading to a 4-class segmentation (air, soft-tissue, fat and lungs) (Martinez-Möller et al., 2009), or on a T1-w sequence, resulting in a 3-class segmentation (air, soft-tissue and lungs) (Schulz et al., 2011). While the results obtained in whole-body studies are satisfactory, the lack of bone information has a significant impact on the quantification of the radionuclide uptake in brain studies (Schleyer et al., 2010; Andersen et al., 2014; Dickson et al., 2014). Several groups have thus focused on developing techniques able to delineate bone. The first methods were based on T1-w images but their success was limited by the difficulty in differentiating bone from air and CSF as they all have similar low intensities on T1-w images. The necessity of using an MRI sequence able to capture bone signal became apparent and methods using the UTE sequence, on its own or combined with other sequences such as the Dixon, have been developed. The downside of the UTE and Dixon sequences is that their use is often limited to attenuation

correction. The time spent acquiring them reduces the time available for clinically relevant sequences. The UTE sequence demonstrated its usefulness when used in the brain region (Cabello et al., 2015) but evaluations for whole-body applications are still needed. If segmentation-based methods made a pivotal progress by being able to delineate bone, a limitation still remains. Once segmented, fixed LACs are assigned to the different tissues classes, which may limit the attenuation map accuracy as the variabilities in attenuation coefficients between the subjects and within the tissue classes are not accounted for. These variabilities are particularly important in the bone region (Fehily et al., 1992; Schulte-Geers et al., 2011) and the lungs (Marshall et al., 2012). To overcome this limitation, groups have developed techniques to map MR image intensities to CT HU in the bone region based on the properties of the R2* maps, derived from the UTE sequence, which provide bone density information (Juttukonda et al., 2015; Ladefoged et al., 2015). Advances in segmentation methods are still needed to improve the tissue delineation in regions with air/tissue and air/bone interfaces, such as nasal region (Aasheim et al., 2015). Another challenge will be to reduce the influence of MR image artefacts that occur in a substantial number of PET/MR datasets and can alter PET quantification and visual interpretation (Brendle et al., 2015).

The other main family of MR-based attenuation correction methods relies on atlases. By construction these methods include bone prediction and generate continuous attenuation coefficients. The first atlas-based methods developed relied on a single atlas or template to generate a subject-specific attenuation map. Their accuracy is limited as a single template can hardly be representative of all the potential patients, even if they do not present morphological abnormalities. These methods also strongly depend on the accuracy of the registration used to map the atlas to the target subject. A solution to both improve the representativeness of the atlas and reduce the impact of registration inaccuracies is to use a database of atlases. However, this comes with the price of having to run multiple non-rigid registrations. An alternative is to divide the training and target images into patches. Patch-based methods do not require non-rigid alignment between the training and target subjects but the patch search has to be carefully designed to guarantee a reasonable run time. Rather than focusing on subsets of the images, it is possible to globally learn a mapping between MR image intensities and CT HU from a training dataset. Supervised learning methods, as to some extent the other atlas-based methods, need images with sufficient contrast to distinguish between air, bone, and soft-tissues. Finally, more studies are necessary to evaluate the impact of anatomical abnormalities on the resulting attenuation maps.

When I started my PhD in 2012, a limited number of attenuation correction methods had been developed. The methods available on the mMR Biograph (Siemens Healthcare, Erlangen, Germany) for brain studies were based on the segmentation of Dixon images in four classes (air, lungs, fat and soft-tissue) (Martinez-Möller et al., 2009) or of UTE images in three classes (air, soft-tissue and bone) (Catana et al., 2010). When compared to CT-based attenuation correction, these methods could present differences in activity concentrations of up to 21% for the Dixon-based and 17% for the UTE-based approach (Dickson et al., 2014). This significant underestimation of activity concentrations throughout the brain was limiting the quantitative accuracy of neurological PET/MR (Dickson et al., 2014). As an alternative to segmentation-based methods, atlas-based approaches, first single-atlas (Montandon and

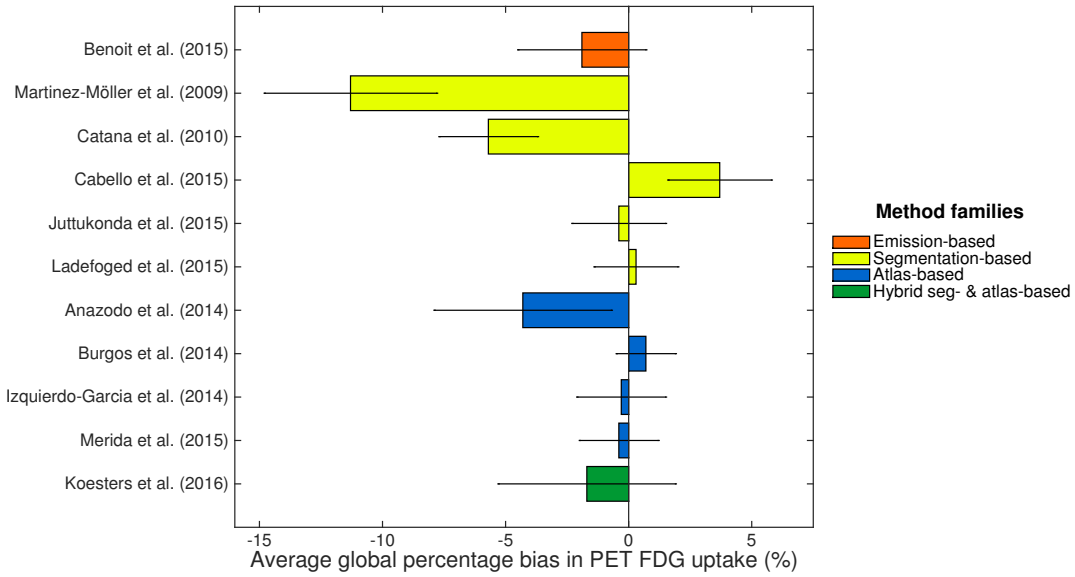

Figure 2.2: Bar plots displaying the average global percentage bias in PET FDG uptake obtained with different MR-based attenuation correction methods evaluated in (Ladefoged et al., 2016). The error bars represent twice the standard deviation.

Zaidi, 2005) and then multi-atlas (Hofmann et al., 2008), had started to be developed. Their promising initial results, an activity overestimation of less than 10% (Hofmann et al., 2008), pushed me to explore this direction further.

At the very end of my PhD, Ladefoged et al. (2016) published a multi-centre study aiming at evaluating the performance of various attenuation correction methods. In total, 11 methods were evaluated: an emission-based (Benoit et al., 2015), five segmentation-based (Martinez-Möller et al., 2009; Catana et al., 2010; Cabello et al., 2015; Juttukonda et al., 2015; Ladefoged et al., 2015), four atlas-based (Anazodo et al., 2015; Burgos et al., 2014b; Izquierdo-Garcia et al., 2014; Merida et al., 2015) and a hybrid approach combining segmentation and use of an atlas (Koesters et al., 2016). Brain FDG PET images of $\sim$200 subjects were reconstructed using the different MR-based attenuation maps and compared to the reference PET images reconstructed using the CT-based attenuation maps. The average global percentage bias in PET FDG uptake obtained with the different MR-based attenuation correction methods is shown in Figure 2.2. These results highlight the limited accuracy of the vendor-provided methods (Martinez-Möller et al., 2009; Catana et al., 2010), whose global errors fall outside of the $\pm$5% often considered as the acceptable limit, and suggest that segmentation-based methods with subject-specific bone attenuation coefficients (Juttukonda et al., 2015; Ladefoged et al., 2015) and some atlas-based methods (Burgos et al., 2014b; Izquierdo-Garcia et al., 2014; Merida et al., 2015) are able to provide accurate enough attenuation correction.

Table 2.1: Overview of the transmission-based approaches as they appear in section 2.1.

Method	Inputs	Require TOF?	Short description of the method
Mollet et al. (2012)	Emission and transmission data	Yes	Joint reconstruction of simultaneously acquired emission and transmission using a static annulus-shaped transmission source
Watson et al. (2014)	Emission and transmission data	No	Joint reconstruction of simultaneously acquired emission and sparse transmission
Kawaguchi et al. (2014)	Emission, transmission and anatomical MRI data	No	Attenuation estimation using a non-rotational radiation source and a segmented tissue map

Table 2.2: Overview of the emission-based approaches as they appear in section 2.2.

Method	Inputs	Require TOF?	Short description of the method
Censor et al. (1979)	Emission data	No	Iterative inversion of the forward mathematical model
Nuyts et al. (1999)	Emission data	No	Maximum-likelihood reconstruction of activity and attenuation (MLAA)
Rezaei et al. (2012)	Emission data	Yes	Maximum-likelihood reconstruction of activity and attenuation (MLAA)
Rezaei et al. (2014)	Emission data	Yes	Maximum likelihood reconstruction of activity and attenuation correction factors (MLACF)
Defrise et al. (2014)	Emission data	Yes	Maximum likelihood reconstruction of activity and attenuation correction factors (MLACF)
Li et al. (2015)	Emission data	Yes	Attenuation-estimation from emission histo-images
Berker et al. (2014)	Emission and scattered data	No	Scatter-to-attenuation (S2A) back-projection
Salomon et al. (2011)	Emission data and anatomical priors	Yes	Iterative reconstruction using TOF spatial constraint and MR anatomical information
Mehranian and Zaidi (2015)	Emission data and anatomical priors	Yes	MLAA using constrained Gaussian mixture model and Markov random field smoothness prior
Benoit et al. (2015)	Emission data and anatomical priors	No	Modified MLAA using MR anatomical information

Table 2.3: Overview of the segmentation-based approaches as they appear in section 2.3.

Method	Bone class?	Input images	Area	LACs	Short description of the method
Martinez-Möller et al. (2009)	No	Dixon	Whole-body	Predefined	Thresholding and connected-component analysis
Schulz et al. (2011)	No	T1-w	Whole-body	Predefined	Region growing
Chang et al. (2013)	No	NAC-PET	Whole-body	Predefined	Iterative segmentation involving active contour model, thresholding and region growing
Le Goff-Rougetet et al. (1994)	Yes	T1-w	Brain	Predefined	Thresholding
Zaidi et al. (2003)	Yes	T1-w	Brain	Predefined	Fuzzy c-means
Wagenknecht et al. (2009)	Yes	T1-w	Brain	Predefined	Supervised neural network and anatomical knowledge
Yang and Fei (2013)	Yes	T1-w	Brain	Predefined	Multiscale filtering in the Radon domain
Anazodo et al. (2015)	Yes	T1-w and Dixon	Brain	Predefined	Thresholding, connected-component analysis and SPM
Keereman et al. (2010)	Yes	Dual UTE	Brain	Predefined	Thresholding on the R2* map
Cabello et al. (2015)	Yes	Dual UTE	Brain	Predefined	Thresholding on the postprocess R2* map
Catana et al. (2010)	Yes	Dual UTE	Brain	Predefined	Thresholding on combinations of UTE images
Berker et al. (2012)	Yes	Triple-echo UTE	Brain	Predefined	Thresholding on combinations of UTE images
Hsu et al. (2013)	Yes	T1-w, T2-w, Dixon and dual UTE	Brain	Predefined	Fuzzy c-means
Su et al. (2015)	Yes	UTE-mDixon	Brain	Predefined	Fuzzy c-means
Khateri et al. (2015)	Yes	Short echo time and Dixon	Brain	Predefined	Fuzzy c-means
Juttukonda et al. (2015)	Yes	Dual UTE and Dixon	Brain	Subject-specific	Thresholding and R2* to HU mapping
Ladefoged et al. (2015)	Yes	Dual UTE	Brain	Subject-specific	Thresholding, R2* to HU mapping and regional masks

Table 2.4: Overview of the atlas-based approaches as they appear in section 2.4.

Method	Subcategory	Atlas/training dataset	Input images	Area	Short description of the method
Montandon and Zaidi (2005)	Single atlas	PET-transmission atlas	PET	Brain	Non-rigid registration
Kops and Herzog (2007)	Single atlas	MRI-transmission atlas	T1-w	Brain	Non-rigid registration
Schreibmann et al. (2010)	Single atlas	CT template	Structural MRI	Brain	Non-rigid registration
Dowling et al. (2012)	Single atlas	MRI-CT atlas	T2-w	Pelvis	Non-rigid registration
Izquierdo-Garcia et al. (2014)	Single atlas	MRI-CT atlas	T1-w	Brain	Non-rigid registration (SPM)
Sjölund et al. (2015)	Multi-atlas	Database of T1-w and CT image pairs	T1-w	Brain	Non-rigid registration and fusion by iterative registration to the mean
Merida et al. (2015)	Multi-atlas	Database of T1-w and CT image pairs	T1-w	Brain	Non-rigid registration and fusion based on maximum probability
Roy et al. (2014)	Patch	Database of UTE and CT image pairs	Dual UTE	Brain	Patches combined via a Bayesian framework
Andreasen et al. (2015)	Patch	Database of T1-w and CT image pairs	T1-w	Brain	Patches combined via a similarity-weighted average
Huynh et al. (2016)	Patch	Database of T1-w and CT image pairs	T1-w	Brain	Prediction using structured random forest and auto-context model
Wu et al. (2015)	Patch	Database of MRI and CT image pairs	T1-w and/or T2-w	Brain	Prediction based on local sparse correspondence combination
Johansson et al. (2011)	Supervised learning	Database of UTE, T2-w and CT image triplets	Dual UTE and T2-w	Brain	Gaussian mixture regression
Navalpakkam et al. (2013)	Supervised learning	Database of UTE, Dixon and CT image triplets	Dual UTE and Dixon	Brain	ε-insensitive support vector regression
Hofmann et al. (2008)	Multi-atlas & regression	Database of T1-w and CT image pairs	T1-w	Brain	Non-rigid registration and Gaussian process regression
Hofmann et al. (2011)	Multi-atlas & regression	Database of UTE, Dixon and CT image triplets	Dual UTE and Dixon	Whole-body	Non-rigid registration and Gaussian process regression
Gudur et al. (2014)	Multi-atlas & regression	Database of T1-w and CT image pairs	T1-w	Brain	Non-rigid registration and Bayesian framework
Chen et al. (2015)	Multi-atlas & regression	Database of T1-w and CT image pairs	T1-w	Brain	Non-rigid registration and sparse regression

Table 2.5: Overview of the atlas-based approach developed in this thesis.

Method	Subcategory	Atlas/training dataset	Input images	Area	Short description of the method
Burgos et al. (2013, 2014a)	Multi-atlas	Database of T1-w and CT image pairs	T1-w	Brain	Non-rigid registration and fusion based on local morphological similarity
Burgos et al. (2015a)	Multi-atlas	Database of T1-w, T2-w and CT image triplets	T1-w and/or T2-w	Brain	Non-rigid registration and fusion based on local morphological similarity
Burgos et al. (2015c)	Multi-atlas	Database of T2-w and CT image pairs	T2-w	Head & neck	Non-rigid registration and fusion based on local morphological similarity
Burgos et al. (2016)	Multi-atlas	Database of T1-w, T2-w and CT image triplets	T1-w and T2-w	Pelvis	Non-rigid registration and fusion based on local morphological similarity

Table 2.6: Overview of the hybrid segmentation/atlas-based approaches as they appear in section 2.5.

Method	Input images	Area	Short description of the segmentation method	Atlas composition	Short description of the atlas method
Bezrukov et al. (2013)	Dixon	Whole-body	Thresholding	Dixon and CT images	Non-rigid registration and Gaussian process regression
Marshall et al. (2013)	Turbo-FLASH	Whole-body	Thresholding	CT images	Non-rigid registration and selection based on similarity metrics
Poynton et al. (2014)	Dual UTE and T1-w	Brain	Trained classifier	Dual UTE, T1-w and CT images	Affine registration
Paulus et al. (2015)	Dixon	Whole-body	Thresholding	Dixon and bone masks	Non-rigid registration
Koesters et al. (2016)	Dixon	Brain	Thresholding	Dixon and bone masks	Non-rigid registration

Chapter 3

CT synthesis from a single T1-w MR image

The proposed MR-based attenuation correction method follows the principle of multi-atlas propagation to synthesise a CT from an MR image. As an alternative to a one-to-one mapping from the observed MR image intensities to CT-like intensities, one can exploit the concept of morphological similarity between subjects. When used in the context of segmentation propagation (Heckemann et al., 2006), a set of segmented anatomical atlases from several subjects are mapped to a target subject and subsequently fused according to the morphological similarity between the mapped and the target anatomical images. This morphological similarity, normally interpreted as an image similarity measure, is used to enforce the fact that the most morphologically similar atlases should carry more weight during the fusion process (Sabuncu et al., 2010). This work exploits the same idea, but for the propagation and fusion of continuous image intensities. The developed algorithm makes use of a pre-acquired set of aligned MR/CT image pairs from multiple subjects to propagate, in a voxel wise fashion, the CT intensities corresponding to similar MR images. This enables the synthesis of a patient-specific pseudo CT image, from which the attenuation map (μmap) is then generated.

The method and results presented in this chapter have been published in Burgos et al. (2013), Burgos et al. (2014a) and Burgos et al. (2014b).

3.1 Method

A diagram illustrating the proposed method in which a synthetic CT is obtained from a given MR image is shown in Figure 3.1.

3.1.1 MR-CT database preprocessing and inter-subject mapping

The atlas database consisted of pairs of T1-weighted MR and CT brain images. T1-w images were corrected for intensity non-uniformity following a non-parametric non-uniform intensity normalisation method (Sled et al., 1998). CT images were segmented to separate the head from the bed using thresholding and morphological operators.

For each subject, the MR image was affinely aligned to the CT using a symmetric approach (Modat et al., 2014) of the block matching algorithm developed by Ourselin et al. (2001). The block matching framework combines two stages in a multi-scale (coarse to fine) hierarchy. The first stage consists of finding for each block of the reference image the most similar block in the floating image. The

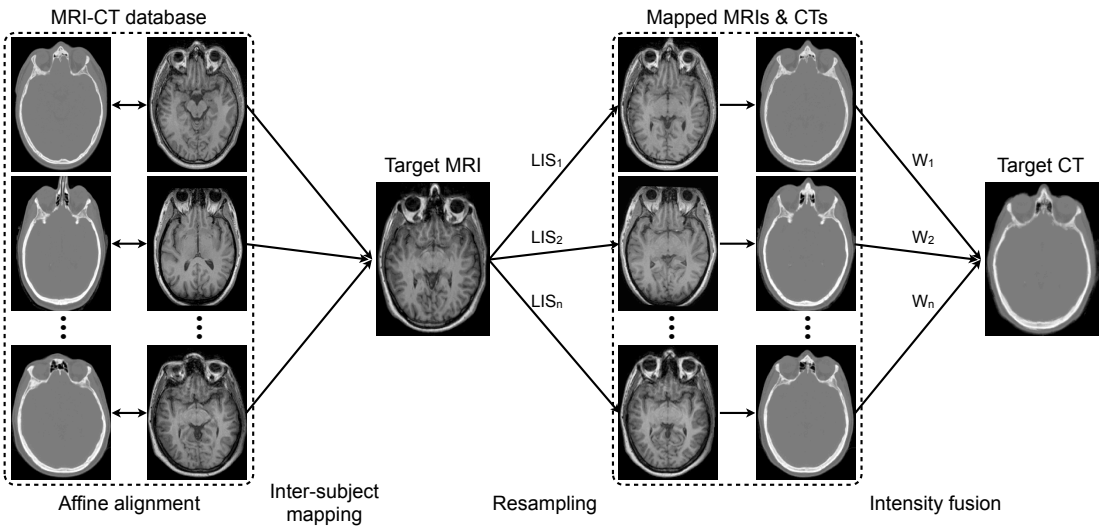

Figure 3.1: CT synthesis diagram for a given T1-w MR image. All the MR images in the atlas database are registered to the target MR image. The CTs in the atlas database are then mapped using the same transformation to the target MR image. A local image similarity measure (LIS) between the mapped and target MR images is converted to weights (W) to reconstruct the target CT.

similarity is assessed using the normalised cross correlation. The second stage consists of finding the global rigid transformation that best explains the local correspondences by mean of a least-trimmed squared regression. Even though this is an intra-subject alignment, a full affine registration was used to compensate for possible gradient drift and calibration in the MRI scans.

In order to synthesise the CT from a given MR image, one first needs to register all the MR images from the atlas database to the target MR image. This inter-subject coordinate mapping was obtained using a symmetric global registration followed by a cubic B-spline parametrised non-rigid registration, using normalised mutual information as a measure of similarity (Modat et al., 2010). All the CTs in the atlas database were then mapped to the target subject using the transformation that maps the subject's corresponding MR image in the atlas database to the target MR image. Through this registration and resampling procedure, one obtains a series of MR/CT pairs aligned to the MR image of the target subject.

3.1.2 CT synthesis

The proposed framework uses a local image similarity measure between the target MR image and the set of registered MR images as a metric of the underlying morphological similarity. Provided that the local image intensity is a good approximation of the local morphological similarity between subjects, I assume that if two MR images are similar at a certain spatial location, the two CT images will also be similar at this location.

3.1.2.1 Image/morphological similarity

The similarity measure monitors the local quality of match between the MR image of the target subject and each of the warped MR images from the atlas database. In this work, two similarity measures were tested: the convolution-based fast local normalised correlation coefficient (LNCC) proposed by Cachier et al. (2003) and the local normalised sum of square differences (LNSSD). The LNCC evaluates the quality of alignment between two images by calculating the correlation between the signals, with a

larger focus on high contrast regions, while the LNSSD characterises the differences in intensity between the two images, making it more susceptible to contrast problems.

Let the target subject's MR image be denoted by I^{MRI} and its corresponding unknown CT be denoted by I^{CT}. For each of the N atlases in the database, let the mapped MR and CT images of atlas n be denoted by J_n^{MRI} and J_n^{CT} respectively. The LNCC between I^{MRI} and J_n^{MRI} at voxel v is then given by

$$\mathrm{LNCC}_{n,v} = \frac{\langle I^{MRI}, J_n^{MRI} \rangle_v}{\sigma(I^{MRI})_v \, \sigma(J_n^{MRI})_v} \quad . \tag{3.1}$$

As in Cachier et al. (2003), the means and standard deviations at voxel v were calculated using a Gaussian kernel G_{σ_G} with standard deviation σ_G through convolution

$$\bar{I}_v = \left[G_{\sigma_G} * I \right]_v \qquad \sigma(I)_v = \sqrt{\overline{I^2}_v - \bar{I}_v^2}$$

$$\langle I, J \rangle_v = \overline{I \cdot J}_v - \bar{I}_v \cdot \bar{J}_v \quad ,$$

where $*$ denotes the convolution operator. High LNCC values indicate a better local match between the two MR images. The LNSSD is given by

$$\mathrm{LNSSD}_{n,v} = \left[G_{\sigma_G} * \left(\frac{I^{MRI} - \overline{I^{MRI}}}{\sigma(I^{MRI})} - \frac{J_n^{MRI} - \overline{J_n^{MRI}}}{\sigma(J_n^{MRI})} \right) \right]_v^2 \tag{3.2}$$

where G_{σ_G} is a Gaussian kernel with standard deviation σ_G. Low LNSSD values indicate a better local match between the two MR images.

A ranking scheme similar to the one proposed by Yushkevich et al. (2010) was used to compensate for registration inaccuracies, giving a larger weight to the images better registered to the target image. The LNCC and LNSSD at each voxel were ranked across all atlas images, with the rank being denoted by $R_{n,v}$. The ranks $R_{n,v}$ were then converted to weights by applying an exponential decay function

$$W_{n,v} = e^{-\beta R_{n,v}} \tag{3.3}$$

with $W_{n,v}$ being the weight associated with the n^{th} subject image at voxel v. With the ranking strategy, the sum and separation of the weights for different voxels are the same at every voxel location, which increases the algorithm's ability to discriminate between atlases in regions with low contrast and leads to better results.

3.1.2.2 Intensity fusion

Similarly to the label fusion framework suggested by Cardoso et al. (2012), an estimate of the target subject's CT can be obtained by a spatially varying weighted averaging. The weights $W_{n,v}$ were used to reconstruct the target CT image I^{CT} at voxel v as follows:

$$I_v^{CT} = \frac{\sum_{n=1}^{N} W_{n,v} \cdot J_{n,v}^{CT}}{\sum_{n=1}^{N} W_{n,v}} \quad . \tag{3.4}$$

3.1.3 Attenuation map

To obtain the μmap, the CT values expressed in HU were converted to linear attenuation coefficients in cm^{-1} by a piecewise linear transformation (Burger et al., 2002)

$$\mu = \begin{cases} \mu_{\text{water}} \left(1 + \frac{I^{CT}}{1000}\right) & I^{CT} \leq 0 \text{ HU} \\ \mu_{\text{water}} \left(1 + \frac{I^{CT}}{1000} \frac{\rho_{\text{water}}(\mu_{\text{bone}} - \mu_{\text{water}})}{\mu_{\text{water}}(\rho_{\text{bone}} - \rho_{\text{water}})}\right) & I^{CT} > 0 \text{ HU} \end{cases} \tag{3.5}$$

where μ_{water} and μ_{bone} represent the attenuation coefficients at the PET 511 keV energy for water and bone respectively and ρ_{water} and ρ_{bone} represent the attenuation coefficients at the CT energy (120 keV) respectively. These values were set to $\mu_{\text{water}} = 0.096$ cm^{-1}, $\mu_{\text{bone}} = 0.172$ cm^{-1}, $\rho_{\text{water}} = 0.158$ cm^{-1} and $\rho_{\text{bone}} = 0.326$ cm^{-1}. The synthetic CT image was then smoothed using a Gaussian filter with a kernel standard deviation of 2 voxels ($1.172 \times 1.172 \times 2.5$ mm^3) to approximate the PET's point spread function (PSF), and resampled to the PET's discretisation grid. This method is widely accepted to generate attenuation maps from CT images, as an alternative to methods exploiting transmission scans, when the subject does not present metal implants. The transformation accuracy can be improved by adjusting the attenuation coefficient of water to the scanner used (Burger et al., 2002; Carney et al., 2006; Ay et al., 2011).

3.2 Validation and results

3.2.1 Data

Two distinct datasets were used in this work. The first dataset is used for the optimisation of the parameters and the second dataset for the validation. Subjects from the first and second datasets were part of a dementia study and an epilepsy study, respectively, and do not present unusual anatomy.

3.2.1.1 Parameter optimisation

The dataset dedicated to the parameter optimisation was composed of 18 pairs of brain T1-weighted MR and CT images. The T1-weighted MR images (3.0 T; TE=2.9 ms, TR=2200 ms, TI=900 ms; flip angle 10°; voxel size $1.1 \times 1.1 \times 1.1$ mm^3) were acquired on a Siemens Magnetom Trio scanner; the CTs (voxel size $0.586 \times 0.586 \times 2.5$ mm^3, 120 kVp, 300 mA) on a GE Discovery ST PET/CT scanner.

3.2.1.2 Validation

The dataset used for the validation was composed of 56 brain T1-weighted MRIs, CTs, and ultra-short echo time (UTE)-based μmaps, 41 reconstructed PET images, and 16 PET sinograms. The T1-weighted MR images (3.0 T; TE/TR/TI, 2.63 ms/1700 ms/900 ms; flip angle 9°; voxel size $0.53 \times 0.53 \times 1.1$ mm^3), UTE-based μmaps (voxel size $1.562 \times 1.562 \times 1.562$ mm^3) and PET sinograms (radiopharmaceutical: FDG) were acquired on a Siemens Biograph mMR hybrid PET/MR scanner; the CTs (voxel size $0.586 \times 0.586 \times 1.25$ mm^3, 120 kVp, 300 mA) and reconstructed PETs (radiopharmaceutical: FDG; voxel size $1.953 \times 1.953 \times 3.27$ mm^3) on a GE Discovery ST PET/CT scanner. 250 MBq of FDG were administered half an hour before the 15-minute PET/CT examination. The patients were then transferred to the PET/MR scanner for a 15-minute PET acquisition.

3.2.2 Parameter optimisation

The morphological similarity between the target MR image and each of the registered MR images from the atlas database was assessed using a local image similarity measure. For both the LNCC and LNSSD metrics, two parameters were optimised using a leave-one-out cross validation on the 18 subjects from the first dataset: the standard deviation of the Gaussian kernels used in equations 3.1 and 3.2 (σ_G, expressed in voxels)

$$\sigma_G = \begin{bmatrix} 1 & 3 & 5 & 7 & 9 \end{bmatrix} ,$$

and β from equation 3.3 whose value influences the repartition of the weights

$$\beta = \begin{bmatrix} 1 & 0.5 & 0.25 & 0.1 & 0.01 \end{bmatrix} .$$

The weighted sum tends to the mean when β is small.

Using only the MR image of the subject, a pseudo CT image ($I = I^{CT}$) was generated using the proposed method. This synthetic CT was then compared to the reference CT ($R = R^{CT}$). The metric employed to measure the synthesis error was the MAE, defined as

$$\text{MAE} = \frac{\sum_v |I_v - R_v|}{V} , \tag{3.6}$$

where V is the number of voxels in the region of interest. This cost function was estimated between the reference CT and the pseudo CT for every subject in the optimisation dataset. The average values of MAE over all subjects are shown in Figure 3.2. The optimisation focused on two regions: the full head and the skull region, obtained setting a threshold at 100 HU. The skull region is important as bones have the highest attenuation coefficients and can induce large errors.

Results

For both the full head and the skull region, the LNCC with $\sigma_G = 3$ voxels gives the smallest error. $\beta = 0.5$ is the skull optimum and guarantees smoother images. With these parameters, the average MAE is 113 HU for the full head and 240 HU for the skull region. A large range of parameters was tested in the optimisation, all showing small differences in the results. The existence of a plateau in terms of accuracy in the parameter space means that small changes in parameters result in a very similar pseudo CT and indicates that the method is robust to the choice of parameters. For this reason, and to avoid being influenced by other factors, I chose to optimise the parameters using the CT synthesis accuracy rather than the PET reconstruction accuracy.

3.2.3 Validation scheme

In order to validate the algorithm with the previously optimised parameters, but on a completely independent dataset, the performance of the proposed synthesis algorithm was run against reference data for 56 subjects. I also compared it to two other methods: a UTE-based method obtained through MR image segmentation and a simplified atlas-based method.

The UTE-based method relies on two UTE images to segment the head into three tissue classes

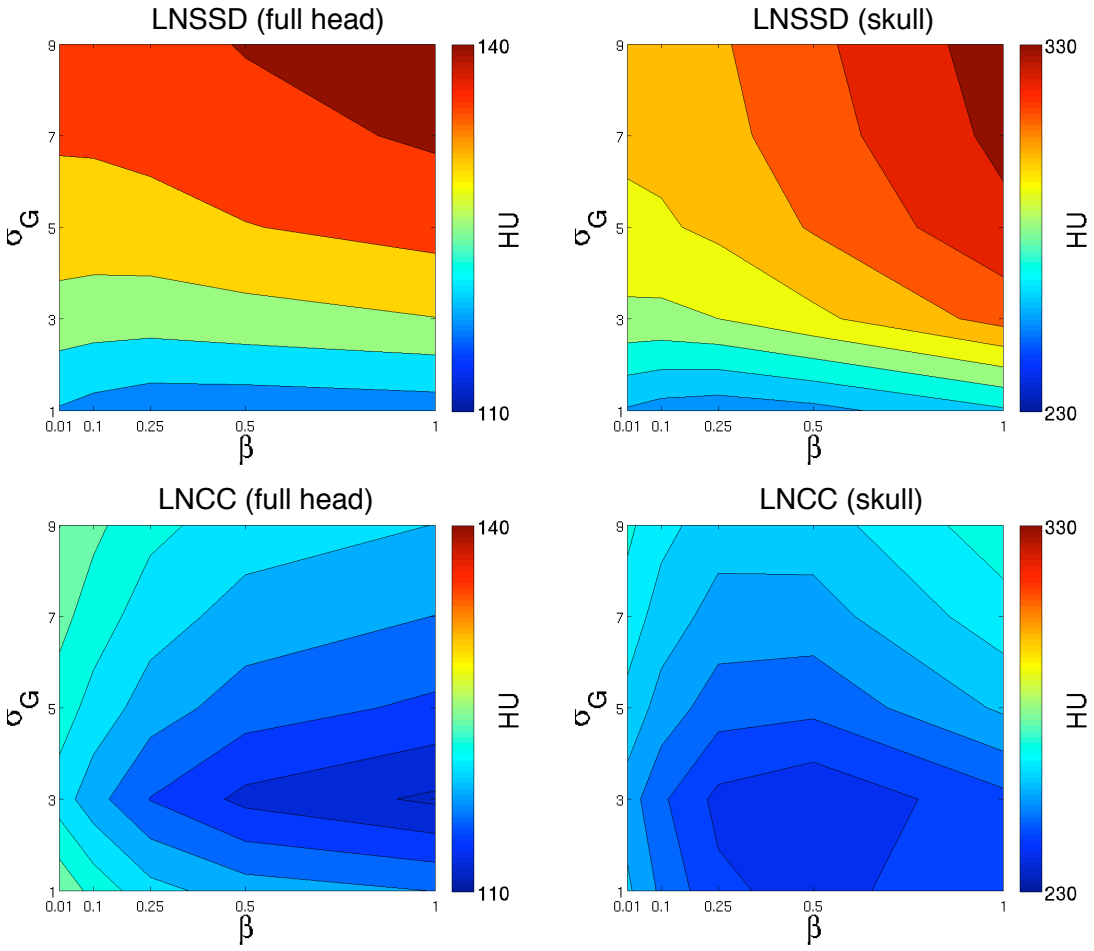

Figure 3.2: Average MAE between the reference CT and the pseudo CT generated using the LNCC and LNSSD as similarity metrics for varying values of σ_G and β. The best parameters are obtained for the LNCC, with $\sigma_G = 3$ and $\beta = 0.5$, giving an average MAE of 113 HU for the full head and 240 HU for the skull region of interest.

(bone, air and soft tissue). A prototype version of this method, only made available to early users of the Siemens Biograph mMR hybrid PET/MR scanners, was used in this work. In the following, when the values assigned to the classes are expressed in HU, the image is referred to as UTE CT, and when the values correspond to linear attenuation coefficients in cm^{-1}, the image is called UTE μmap and matches the PET's PSF and voxel size.

The second method is based on atlases. As in the proposed method, the database of MR and CT image pairs is non-rigidly registered to the target MR image. A global similarity measure, the normalised cross-correlation (NCC), is computed over the full image field of view between each warped MR image and the target MR image to select the most similar atlas to the target. The NCC is defined as

$$\text{NCC}_n = \frac{1}{V} \frac{\langle I^{MRI} - \overline{I^{MRI}}, J_n^{MRI} - \overline{J_n^{MRI}} \rangle}{\sigma(I^{MRI})\,\sigma(J_n^{MRI})} \quad , \tag{3.7}$$

where $\bar{I}$ is the mean and $\sigma(I)$ the standard deviation of image I. The CT corresponding to the selected MR image, the 'best atlas' CT (baCT), is then converted into attenuation map (baCT μmap), as in the proposed method.

Table 3.1: For 56 subjects: Average and SD of the MAE and ME between the reference CT and the pseudo CT, best-atlas CT and UTE CT (left); Average and SD of the rMAE and rME between the reference CT μmap and the pseudo CT, best-atlas CT and UTE μmaps (right). CV for the MAE and rMAE are also presented.

		CT (HU) - Head			μmap (%) - Head		
		pCT	baCT	UTE	pCT	baCT	UTE
MAE	Average	118	160	208	6.8	9.1	13.0
	SD	17	29	24	1.3	1.4	1.4
	CV	14%	18%	12%	19%	15%	11%
ME	Average	-7.6	8.4	-136	-1.1	-0.3	-9.3
	SD	21	27	34	1.5	2.0	2.6

The quantitative validation consisted of three steps:

1. A pseudo CT was synthesised from each subject's MR image following the proposed method. The pCT, baCT and UTE CT were compared to the subject's reference CT image at the original resolution, validating the accuracy of the CT synthesis.

2. The pCT, baCT and UTE CT were converted to attenuation maps using equation 3.5, smoothed to approximate the PET's PSF and resampled to the PET's discretisation grid, to validate how accurate the synthetic CT was at the resolution relevant for PET reconstruction.

3. The PET image was reconstructed from the original or simulated sinogram using the pCT μmap generated using the proposed method, the baCT μmap and the UTE μmap, and compared with the reference PET reconstructed using the CT-based μmap, validating the accuracy of the PET attenuation correction.

The field of view of the MR images contained the head and neck of the subject while, in the CT field of view, only the head was visible. After alignment of the two modalities, the analysis was limited to a mask defined where both image modalities provide information. All quantitative assessments were performed using a leave-one-out cross-validation scheme.

3.2.4 Results

3.2.4.1 Pseudo CT accuracy

Following the proposed method, a pseudo CT was generated using only the MR image of the subject, and then compared to the reference CT. The MAE, as defined in equation 3.6, and the ME defined as

$$\mathrm{ME} = \frac{\sum_v (I_v - R_v)}{V} \quad , \tag{3.8}$$

were calculated between the reference CT and the pseudo CT for every subject in the validation dataset. Contrary to the MAE, which provides information about reconstruction error and deviations from the expected values, the ME provides information about an inherent bias in the methodology. The MAE and ME were also computed between the best-atlas CT and the reference CT, and between the UTE CT and the reference CT. The average $\pm$ standard deviation (SD) MAEs and MEs, measured in Hounsfield

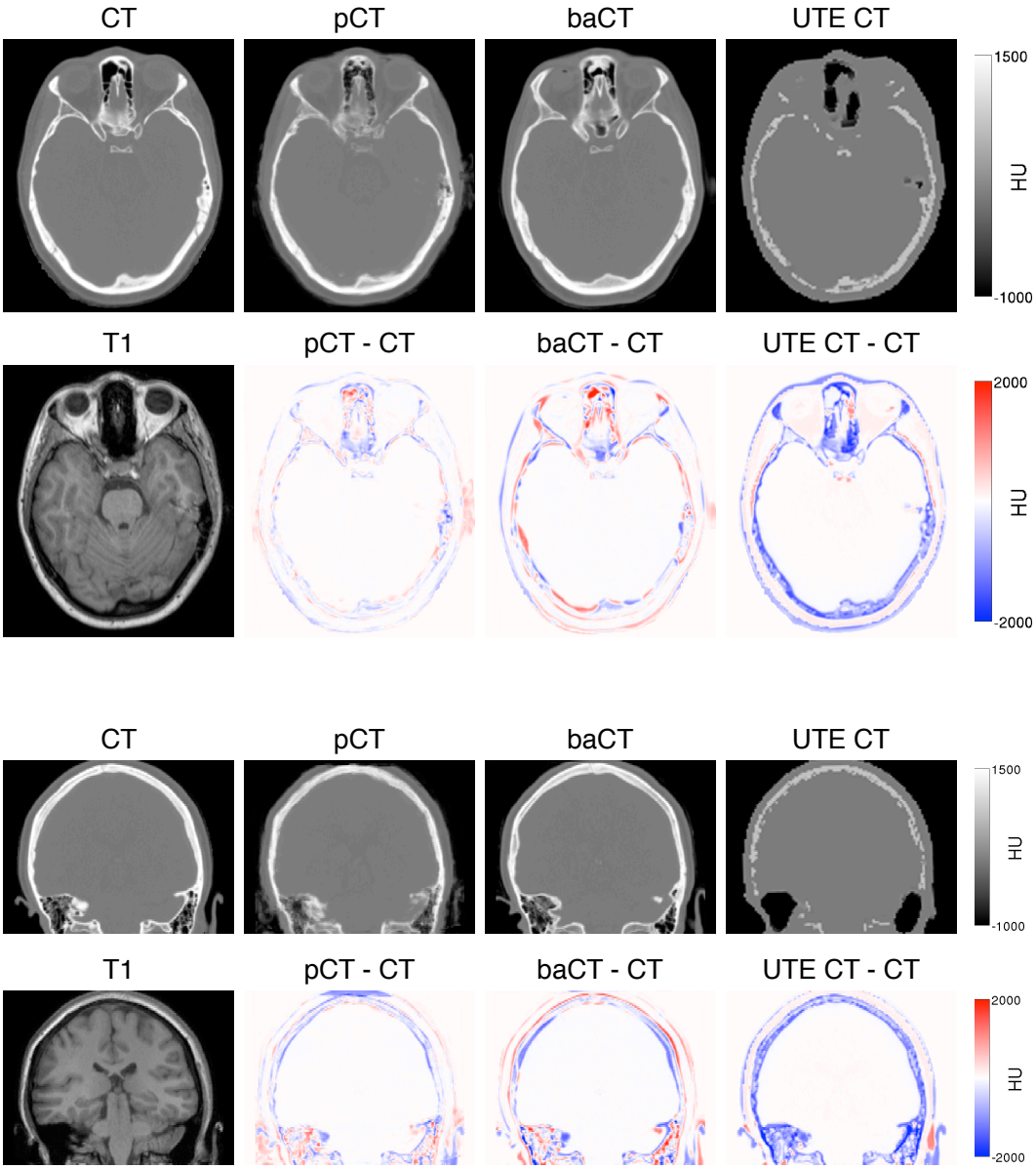

Figure 3.3: For subject 1, from left to right: The acquired CT, the pCT generated by the proposed method, the baCT and the UTE CT (top); the acquired T1, the difference between the pCT and the CT, the difference between the baCT and the CT, and the difference between the UTE CT and the CT (bottom).

units, across all the subjects in the validation dataset are presented in Table 3.1. The coefficients of variation (CV) for the MAE and rMAE are also presented. The average $\pm$ SD absolute error obtained with the pseudo CT method (118 $\pm$ 17 HU) is 1.4 times smaller than the error obtained with the best-atlas method (160 $\pm$ 29 HU) and 1.8 times smaller than the error obtained with the UTE method (208 $\pm$ 24 HU). A paired t-test was used to confirm that the improvement is statistically significant ($p < 10^{-6}$) when the proposed method was employed instead of the best-atlas and UTE-based methods. Examples of reference CT, pseudo CT, best-atlas CT, UTE CT and difference images are presented in Figure 3.3 for a representative subject (subject 1) whose results were close to the average results.

3.2.4.2 Attenuation map accuracy

The relative MAE (rMAE) between the reference μmap ($R = R^{\mu\text{-}map}$) and the pseudo CT μmap ($I = I^{\mu\text{-}map}$) and the relative ME (rME), respectively defined as

$$\text{rMAE} = 100 * \frac{\sum_v |I_v - R_v|}{\sum_v R_v} \quad \text{and} \quad \text{rME} = 100 * \frac{\sum_v (I_v - R_v)}{\sum_v R_v} \ , \tag{3.9}$$

were used to assess the attenuation map synthesis accuracy. The rMAE and rME were also computed between the best-atlas CT μmap and the reference CT μmap, and between the UTE μmap and the reference CT μmap. The average $\pm$ SD rMAEs and rMEs, measured in percentages, across all the subjects in the validation dataset are presented in Table 3.1. The average $\pm$ SD absolute error obtained with the pseudo CT method ($6.8 \pm 1.3\%$) is 1.3 times smaller than the error obtained with the best-atlas method ($9.1 \pm 1.4\%$) and half of the error obtained with the UTE method ($13.0 \pm 1.4\%$). The paired t-test shows a statistically significant improvement ($p < 10^{-6}$) with the proposed method. Examples of reference CT μmap, pseudo CT μmap, best-atlas CT μmap, UTE μmap and difference images are presented in Figure 3.4.

3.2.4.3 PET accuracy

A hardware μmap containing the bed visible in the PET/CT scans, previously extracted from the original CT μmap, was added to the human μmaps (CT, pCT, baCT and UTE μmaps). Due to the unavailability of the raw PET data for most of the subjects, I made use of the PET reconstruction provided by the PET/CT scanner. To reconstruct the PET image with the different μmaps, I followed a projection/reconstruction technique similar to Hofmann et al. (2008). The original PET image and the CT μmap were projected to obtain simulated sinograms. The scatter sinogram was estimated using a Single Scatter Simulation algorithm (Watson, 2000). The attenuation and scatter corrections were subsequently removed from the original simulated PET sinogram producing a non-corrected PET sinogram. The non-corrected PET sinogram was then reconstructed using the CT, pCT, baCT or UTE μmap to correct for attenuation and scatter. The PET image reconstructed using the CT μmap was considered as the reference PET. The iterative reconstruction and scatter estimation were performed using STIR (Thielemans et al., 2012). An ordered subsets expectation maximisation (OSEM) algorithm with three iterations of 21 subsets was used. Effects of PSF and random coincidences were not included and post-reconstruction smoothing was not applied.

Results of PET reconstructions using different attenuation maps and difference images are displayed in Figure 3.5. The rMAE was computed between the reference PET and the pCT, baCT, and UTE PETs for the brain region. Results are shown in Table 3.2. The average $\pm$ SD rMAE obtained using the pCT μmap ($2.87 \pm 0.90\%$) is 1.5 times smaller than the error obtained using the baCT μmap ($4.30 \pm 1.16\%$) and four times smaller than the error obtained using the UTE μmap ($11.86 \pm 2.09\%$), which represents a statically significant improvement ($p < 10^{-6}$) in reconstruction error.

A common practice in the neuro-imaging community is to normalise PET images using a reference region (Minoshima et al., 1995; Lee et al., 2012). For this application, I used the mean PET value in the pons, manually segmented from the T1-w image, to normalise the PET images of each subject, allowing

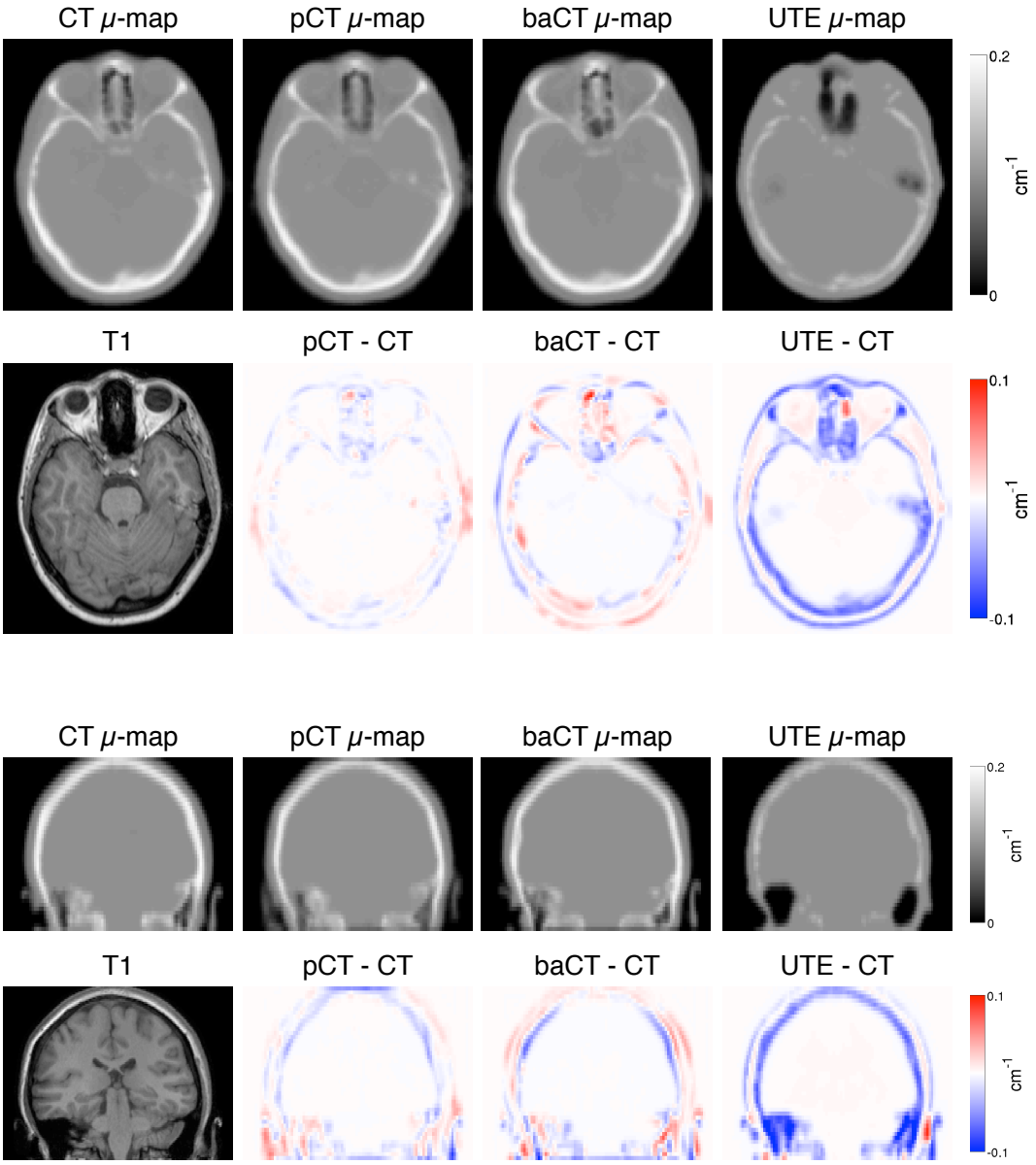

Figure 3.4: For subject 1, from left to right: CT μ-map, pCT μ-map generated by the proposed method, baCT μ-map and UTE μ-map (top); T1, difference between the pCT and CT μ-maps, difference between the baCT and CT μ-maps, and difference between the UTE and CT μ-maps (bottom).

for a comparable range of values. The average $\pm$ SD rMAE obtained for the brain region using the pCT μmap (2.99 $\pm$ 0.98%) is 1.6 times smaller than the error obtained using the baCT μmap (4.76 $\pm$ 1.79%) and 2.6 times smaller than the error obtained using the UTE μmap (7.70 $\pm$ 1.98%), which represents a statically significant improvement ($p < 10^{-6}$). The boxplots in Figure 3.6 show that the proposed method is less prone to produce outlier results compared to the best-atlas and UTE methods. We note that while the results obtained for the proposed and best-atlas methods do not vary significantly depending on the normalisation of the PET images, the mean absolute error obtained with the UTE method decreases when the PET images are normalised.

In order to assess the performance of the proposed method in areas close to the skull, I also analysed results in the grey matter region, which was segmented from the T1-w image and propagated to the PET

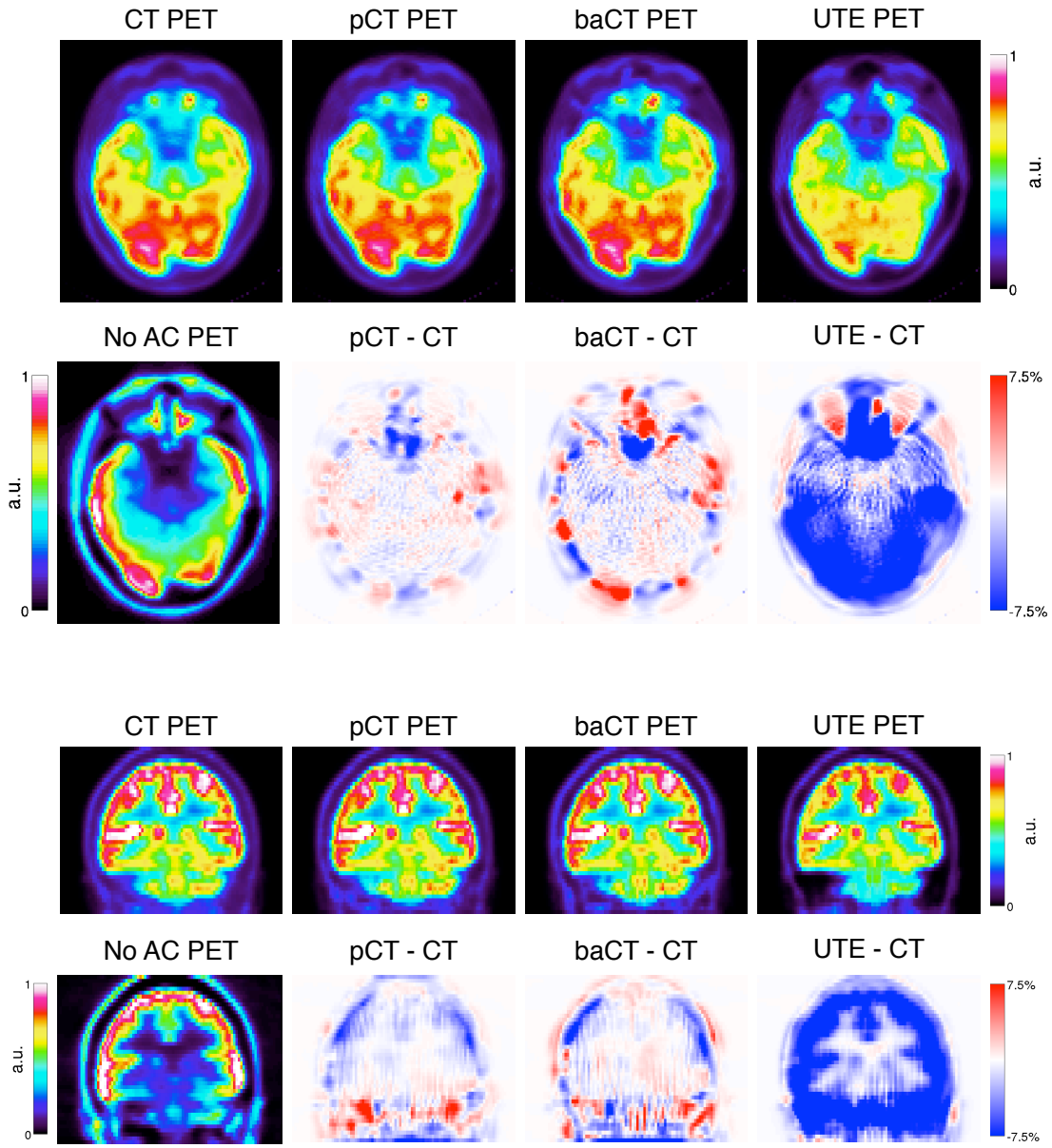

Figure 3.5: For subject 1, from left to right: The reference FDG PET, the pCT PET, the baCT PET and the UTE PET (top); the non corrected PET, the difference between the pCT and CT PETs, the difference between the baCT and CT PETs, and the difference between the UTE and CT PETs (bottom).

images (Cardoso et al., 2011). The average $\pm$ SD rMAE obtained using the pCT μmap (2.98 $\pm$ 0.97%) is significantly smaller ($p < 10^{-6}$) than the error obtained using the baCT μmap (4.80 $\pm$ 1.80%) and the UTE μmap (7.27 $\pm$ 1.90%). These results are similar to the ones obtained in the brain region.

3.2.4.4 PET bias analysis

The main goal when correcting for attenuation is to be able to perform an accurate quantitative analysis of PET data. In order to analyse the bias introduced by the different attenuation correction methods in the PET images, the rME was computed between the reference PET and the pCT, baCT, and UTE PETs for the brain region. The rME results indicate a reduced bias when the proposed method is used (0.17 $\pm$ 2.11%) compared to the best-atlas (0.78 $\pm$ 2.88%) and UTE-based (-11.78 $\pm$ 2.13%) methods.

Table 3.2: For 41 subjects, average and SD of the rMAE and rME between the reference CT PET and the pseudo CT, best-atlas CT and UTE PETs, before and after normalisation, for the brain and grey matter (GM) regions.

		PET (%) - Brain			Normalised PET (%) - Brain			Normalised PET (%) - GM		
		pCT	baCT	UTE	pCT	baCT	UTE	pCT	baCT	UTE
MAE	Average	2.87	4.30	11.86	2.99	4.76	7.70	2.98	4.80	7.27
	SD	0.90	1.16	2.09	0.98	1.79	1.98	0.97	1.80	1.90
	CV	31	27	18	33	38	26	33	38	26
ME	Average	0.17	0.78	-11.78	0.98	1.08	-0.50	0.99	1.17	-0.81
	SD	2.11	2.88	2.13	1.69	3.44	4.91	1.71	3.48	4.80

The Kolmogorov-Smirnov test was used to determine if the bias introduced by the different attenuation correction methods came from a normal distribution with 0 mean, thus assessing if the mean error was significantly different from 0. Furthermore, as the relative mean errors were Gaussian distributed (according to the Kolmogorov-Smirnov test), the F test was used to determine if the variance of the bias differs between methods. All tests were performed at 0.1% significance level.

In contrast with the baCT and UTE μmaps, where the rME was found to differ significantly from zero, the rME is not significantly different from zero when the pCT μmap is used to correct for attenuation. The variances of the three methods are not significantly different.

When normalised, regardless of the μmap used to correct for attenuation, the bias ($<$1.2%) is significantly different from zero. However, the variance of the rME is significantly lower when the proposed method is employed instead of the best-atlas or UTE method.

I also performed a linear regression with the expression $y = \alpha x + \beta$ where x corresponds to the reference, non-normalised, PET and y to either the non-corrected, pCT, baCT, or UTE PET. The averages and SDs of the regression coefficients α and β, and the coefficient of determination R^2, are presented in Table 3.3. R^2 values show a better fit to the reference PET when the pCT μmap is used to correct for attenuation instead of the baCT or the UTE μmaps. Figure 3.7 shows the joint histograms, averaged across 41 subjects, of the pCT, baCT, UTE and non-corrected PETs against the reference PET. We note

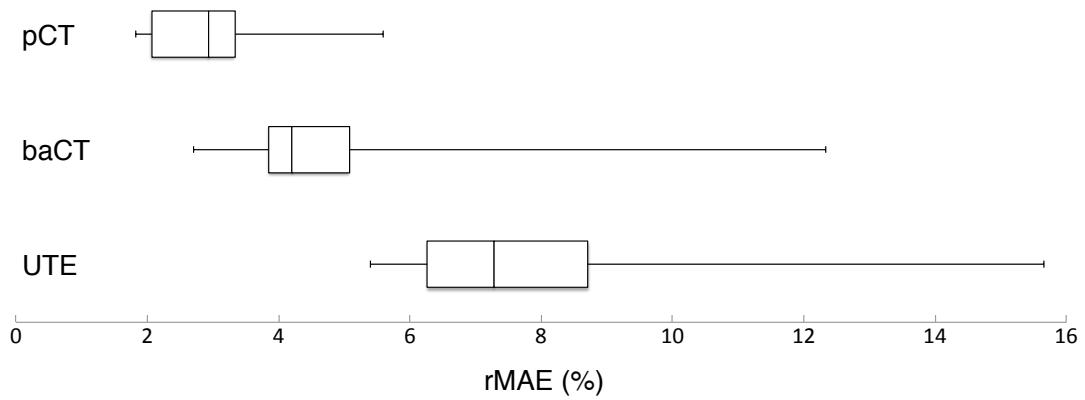

Figure 3.6: For 41 subjects: boxplots displaying the median, the lower and upper quartiles and the minimum and maximum of the rMAE calculated between the reference CT PET and the pseudo CT, best-atlas CT and UTE PETs in the brain after normalisation. Similar results were obtained in the grey matter region.

Table 3.3: For 41 subjects: Average ± SD of the regression coefficients and R^2 values computed in the brain area for the proposed (pCT), best-atlas (baCT) and UTE-based (UTE) methods, and without correction (No AC). Note the increase in R^2 with the proposed approach when compared to other methods.

	pCT	baCT	UTE	No AC
α	1.009 ± 0.021	1.018 ± 0.028	0.905 ± 0.033	0.088 ± 0.007
β	-83.0 ± 153.4	-111.8 ± 242.3	-317.9 ± 390.1	-374.65 ± 120.0
R^2	0.988 ± 0.005	0.973 ± 0.014	0.944 ± 0.014	0.601 ± 0.048

that the pseudo CT method outperforms the UTE method and that the variance is reduced when the PET is corrected by the pCT instead of the baCT μmap.

Finally, the PET images from the 41 subjects were mapped to a common space via a CT-based groupwise registration (Rohlfing et al., 2001; Modat et al., 2014). The average and standard deviation of the difference maps computed between the normalised reference PETs and the normalised PETs reconstructed with the pseudo CT, best-atlas and UTE μmaps, across all the subjects, are presented in Figure 3.8. We note that, while the average of the difference between the reference and both the pCT PETs and baCT PETs is similar, the standard deviation of the difference between the reference and pCT

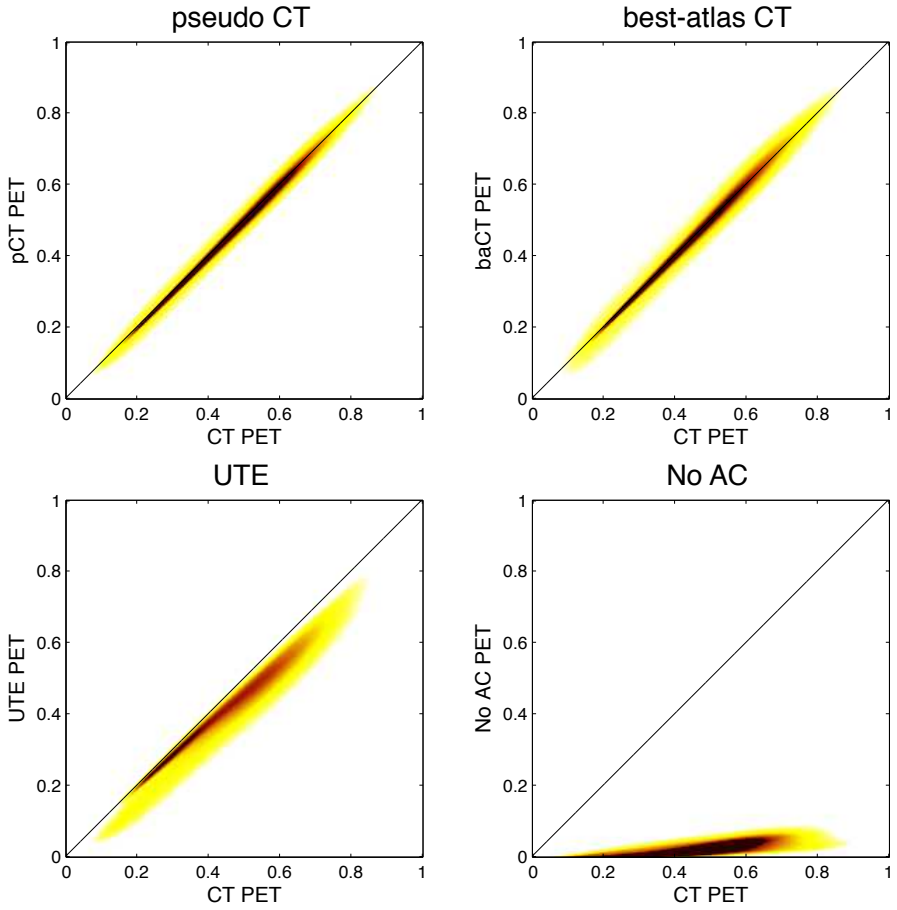

Figure 3.7: Joint histograms in the brain area, averaged across 41 subjects, between the CT and pCT PETs (top left), the CT and baCT PETs (top right), the CT and UTE PETs (bottom left), and the CT and non corrected PETs (bottom right). Images are min/max scaled between 0 and 1. Note the reduced variance when the PET is corrected using the proposed method compared to the best-atlas method.

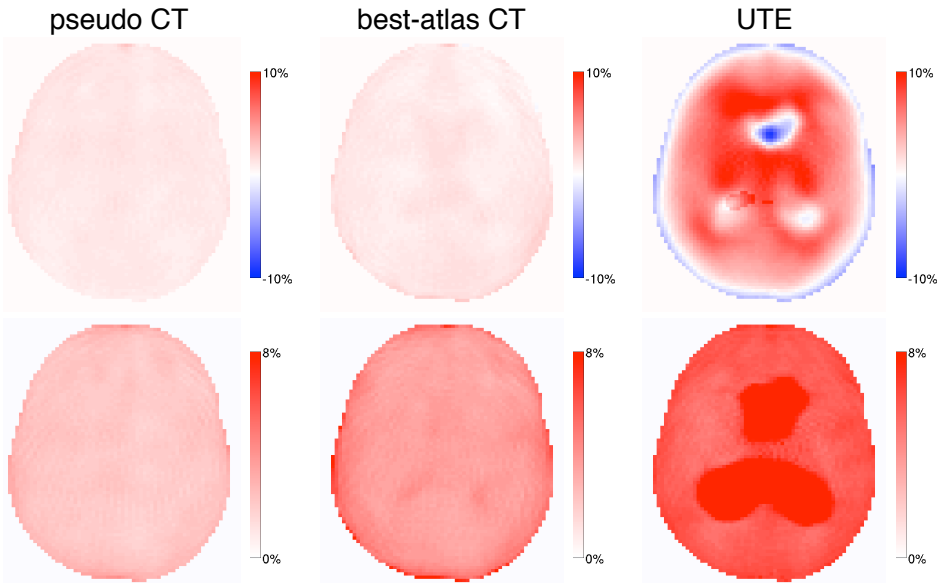

Figure 3.8: Average over 41 subjects (top) and standard deviation (bottom) of the difference between the normalised reference PET and the normalised PETs reconstructed with the pseudo CT, best-atlas and UTE μmaps.

PETs (2.36%) is lower than between the reference and baCT PETs (3.97%).

3.2.4.5 PET reconstruction from original sinogram data

As a final test for the performance of the method, I used an off-line version of the Siemens Healthcare reconstruction software (made available for this project) on PET/MR data for 16 subjects from the validation dataset. The default settings for OSEM (three iterations of 21 subsets, Gaussian post-filtering) were used. I reconstructed PET images from the real sinograms using the CT, pCT, baCT and the UTE μmaps to correct for attenuation. Results are shown for a subject in Figure 3.9. The UTE-based method underestimates the quantity of bone which leads to a global underestimation of the activity in the PET image. Compared to the proposed method, the best-atlas method sometimes fails to accurately delineate the bone, such as in the skull (yellow arrows) and sinus areas (green arrow), which results in a local underestimation of the PET activity. The rMAE and rME, presented in Table 3.4, as well as the joint histograms displayed with their associated coefficients of determination in Figure 3.10, agree with the results presented in the previous section.

Table 3.4: Average and SD of the relative MAE and relative ME between the reference CT PET and the pseudo CT, best-atlas CT and UTE PET images reconstructed from original sinogram.

		PET (%) - Brain		
		pCT	baCT	UTE
MAE	Average	2.35	3.03	12.7
	SD	0.71	0.49	1.55
	CV	30	16	12
ME	Average	0.70	0.88	-12.6
	SD	1.32	1.45	1.60

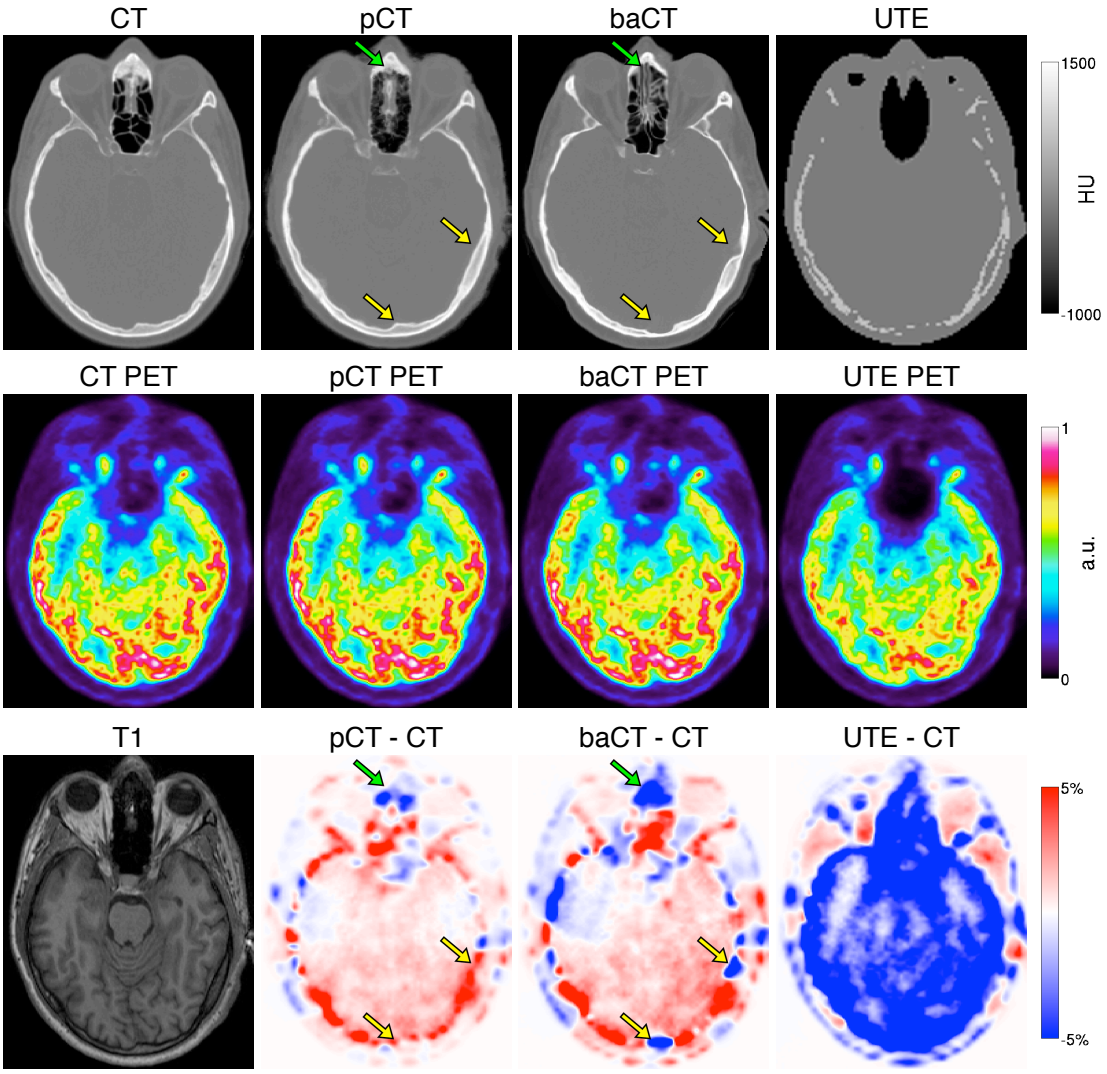

Figure 3.9: From left to right: The CT μ-map, the pCT μ-map generated by the proposed method, the baCT μmap and the UTE μ-map (top row). The reference FDG PET, pCT PET, baCT PET and UTE PET reconstructed with the off-line Siemens Healthcare software (middle row). The T1, the difference between the pCT and CT PETs, the baCT and CT PETs and the UTE and CT PETs (bottom row).

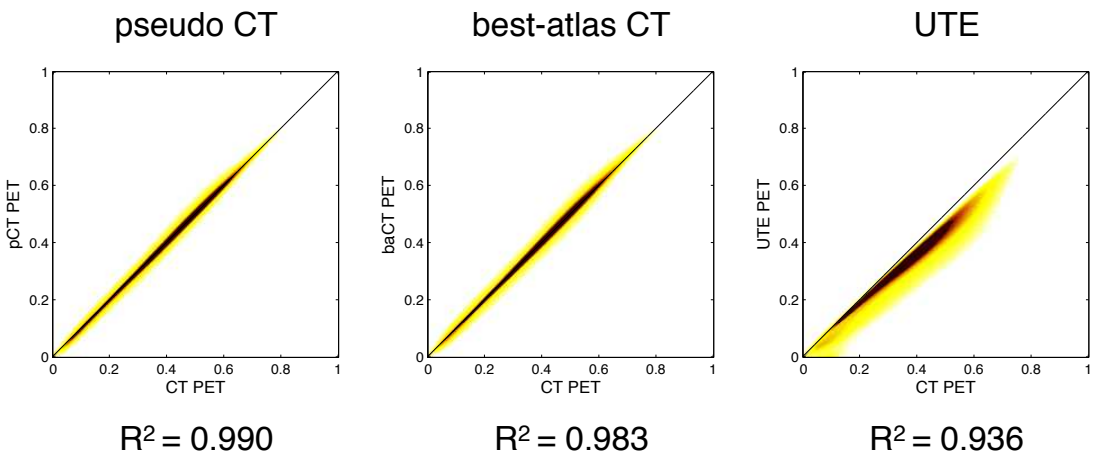

Figure 3.10: Joint histograms, averaged across 16 subjects, between the CT and pseudo CT PETs, the CT and best-atlas CT PETs, and the CT and UTE PET images reconstructed from original sinogram, with their corresponding coefficient of determination R^2.

3.3 Discussion

Following the principle of multi-atlas information propagation, the proposed method synthesises a CT from an MR image which is then processed to obtain an attenuation map used in the PET reconstruction.

Two separate datasets were used for the optimisation and the validation of the method to reduce bias. I compared my solution to a simpler atlas-based method and to a prototype version of a UTE-based method made available to early users of the Siemens Biograph mMR hybrid PET/MR scanners. The results presented in Table 3.1 demonstrate that the absolute error estimated between the pseudo CT and the original CT is significantly smaller compared to the other methods. Difference images in Figure 3.3 reveal that errors are concentrated at the skull/soft-tissue, skull/air and soft-tissue/air boundaries, and that the amount of bone is underestimated when the UTE-based method is used. We also notice in Figure 3.3 that the synthetic CT images are not as sharp as the ground-truth subject's CT at the original resolution. However, this problem is greatly reduced at the voxel size and PSF of the PET image as shown in Figure 3.4. At this resolution, the results show a significant improvement when the proposed method is used compared to the best-atlas and UTE-based methods. Difference images of reconstructed PET images from simulated data in Figure 3.5 show that the UTE-based correction underestimates the radionuclide uptake, even for the soft-tissues. This systematic underestimation is confirmed by the joint histogram Figure 3.7 and the linear regression coefficients in Table 3.3. When the PET is corrected with the pseudo CT or best-atlas μmap, the error is globally lower and mostly affects the skull and sinus areas. Finally, the error is significantly smaller with the pseudo CT method compared to the best-atlas CT method and the bias lower. After normalisation, the error obtained with the UTE-based method is reduced while it remains alike for the proposed and best-atlas methods. All correction methods introduce a bias but the variance of the bias is significantly lower when the pseudo CT method is used instead of the best-atlas or UTE method, as shown in Table 3.1 and Figure 3.8.

The use of the Siemens off-line reconstruction software demonstrates that the proposed method improves the results when applied in a clinical context compared to the method currently in use, as shown in Figure 3.9 and Table 3.4.

In a T1-weighted MR image of the head, cerebrospinal fluid, air and bone have similar intensities but distinct values in a CT image which impedes a one-to-one mapping from the observed MRI intensities to CT-like intensities. Exploiting the concept of morphological similarity between subjects, as an alternative to the one-to-one intensity mapping, improves the synthesis accuracy in boundary areas such as air and bone in the nasal sinuses. The low intensities of bone and air also make the segmentation of MR images challenging (Martinez-Möller et al., 2009; Schleyer et al., 2010; Catana et al., 2010; Keereman et al., 2010; Berker et al., 2012; Yang and Fei, 2013), even after correction of several artefacts (Aitken et al., 2014). The proposed method does not require any segmentation of MR images and thus allows the synthesis of a continuous valued attenuation map and avoids large misclassifications.

However, atlas-based methods also have limitations as relying on a database implies the need of a representative population. But, even if morphological variabilities of the skull are limited, in the case where the target subject presents abnormalities, the non-rigid registration should be able to capture

them. Further experiments with subjects presenting abnormal anatomies are required to validate this expectation. While a large number of registrations can leave room for errors to confound the mapping in a single atlas method, the proposed multi-atlas strategy can compensate for most registration problems by combining the local atlas selection and consensus estimation steps. The more accurate results reached when the proposed method is used, compared to the best-atlas method, demonstrate the advantages of synthesising CTs at a local scale instead of a global scale.

Current limitations of the method are due to the limited anatomical information of CT and T1-weighted MR images. A database with multimodal data including T1-weighted, T2-weighted and UTE sequences would improve the registration and the image similarity estimates, and could provide additional information, such as bone density. Clinical information (patient's gender, age, weight or ethnicity) could also be used to specify the bone density more accurately (Marshall et al., 2013).

This work is focused on brain applications and further experiments are required to validate the method in other regions of the body. The technique could, in theory, be applied to other body parts as long as the morphological variability is represented in the database and the registration between MRI pairs is sufficiently accurate.

3.4 Conclusion

This chapter presents a CT and attenuation map synthesis algorithm based on a multi-atlas information propagation scheme. Compared to state-of-the-art image synthesis techniques, the proposed technique does not assume any explicit mapping between the intensities of the image pairs, as it relies only on their correct pre-alignment. While the sharpness of the synthetic CT images is lower than the reference subject's CT at the original resolution, this problem is greatly reduced at the resolution of the PET image. Overall, the proposed algorithm provides a significant improvement in PET reconstruction accuracy when compared to a simplified atlas-based or UTE-based correction.

Chapter 4

Effect of scatter correction when comparing attenuation maps

As we have seen in the introduction chapter, in PET imaging correcting for photon attenuation is an essential requirement to accurately quantify the radionuclide uptake. For PET/MR imaging, in the absence of a transmission source or CT image, alternative MR-based methods are being developed. Due to the challenge of delineating bone in MR images, these attenuation maps can be inaccurate and lead in some cases to a strong spatial bias of the PET activity, as shown for instance in Dickson et al. (2014). Scatter correction is another key component for the quantitative analysis of PET images. Various authors have quantified the effect of an imprecise attenuation map on the final reconstructed PET image, but its influence on scatter correction has usually been ignored.

In this chapter, I propose to investigate, using simulations, the effect of imperfect attenuation maps on the scatter correction. I focus on three μmaps: a μmap derived from a CT image, considered as the reference, and two MR-based methods: a segmentation-based approach and the multi-atlas approach from the previous chapter. These results have been published in Burgos et al. (2014c).

4.1 Method

4.1.1 MR-based attenuation correction

4.1.1.1 Segmentation-based Approach

The UTE-based method, a prototype version implemented on the first software versions of the Siemens Biograph mMR hybrid PET/MR scanners, is based on the segmentation of a ultrashort echo time (UTE) sequence which enables the differentiation of three tissue classes (bone, air and soft tissue). Predefined attenuation coefficients are then assigned to each tissue class.

4.1.1.2 Multi-atlas approach

The multi-atlas CT synthesis method, described in detail in the previous chapter, relies on a pre-acquired set of aligned MR/CT image pairs from multiple subjects forming an MR-CT database. To generate the CT from a target MR image, each MR image from the database is deformed to the target MR image using affine followed by non-rigid registration. The CT images in the database are then mapped using the

same transformation to the target MR image. A local image similarity measure between the target MR image and the set of registered MR images from the database is used as a surrogate of the underlying morphological similarity, under the assumption that if two MR images are similar at a certain spatial location, the two CT images will also be similar at this location. Finally, the set of registered CTs is fused using a voxel-wise weighting scheme, generating a pseudo CT (pCT). To obtain the μmap, the CT values expressed in HU are converted to linear attenuation coefficients in cm^{-1} by a piecewise linear transformation (Burger et al., 2002), as done in the previous chapter (see eq 3.5).

4.1.2 Scatter correction

In this work, scatter was estimated using a Single Scatter Simulation (SSS) algorithm Watson (2000) and scaled using a tail-fitting strategy, as implemented in STIR (Thielemans et al., 2012). The SSS algorithm consists of using the emission and attenuation information to model single Compton scattering. The estimated scatter is then scaled to fit the tails of the sinogram, obtained from the attenuation map, where it is assumed that the signal is only coming from scattered events. Finally, the scatter estimation and image reconstruction steps are combined in an iterative process as follows:

1. Reconstruction of an initial estimate of the emission data
2. Single scatter estimation using the SSS algorithm
3. Tail-fitting
4. Correction of emission data: the estimated scatter is subtracted from the emission data
5. Reconstruction of the emission data, and back to step 2

4.1.3 PET simulation and reconstruction

PET images were reconstructed with different μmaps following a projection/reconstruction technique, as described in the previous chapter (3.2.4.3). To assess the effect of imperfect μmaps on the scatter correction, a reference PET image with accurate scatter correction is required. The ideal scatter correction is obtained from the PET/CT scanner and relies on the reference CT μmap. I detail a first simulation and reconstruction process where the scatter is estimated from the different μmaps and a second process where the scatter is estimated from the reference CT μmap in the PET/CT scanner.

4.1.3.1 Process with μmap-specific scatter correction

As input for the simulations, I used the CT and reconstructed PET images provided by a PET/CT scanner. The non-corrected PET sinogram S, equivalent to the measured data, was obtained by removing the attenuation and scatter corrections from the original simulated PET sinogram. PET images were then reconstructed using the CT, pCT or UTE μmap to correct for attenuation and scatter, i.e. the scatter was computed from the PET sinogram and the estimated μmap:

Simulation:

Input: True emission image E_T, true μmap μ_T
Output: Simulated PET sinogram S
1: Forward project E_T
2: Simulate attenuation from μ_T
3: Simulate scatter with SSS from μ_T and E_T
4: Combine to obtain simulated PET sinogram S

Reconstruction:

Input: Simulated PET sinogram S and other μmap μ_O
Output: Reconstructed PET image
1: Estimate attenuation from μ_O
2: Estimate scatter from S and μ_O
3: Run OSEM using S and the output of 1 and 2

The PET simulation and reconstruction process with μmap-specific scatter correction ($SC_{\mu map}$) is detailed in Fig. 4.1.

Image reconstruction was performed using an OSEM algorithm with three iterations of 21 subsets using the STIR package (Thielemans et al., 2012). The scatter estimate was incorporated as a background term in the forward model, i.e. in the denominator of the OSEM update. Effects of PSF and random coincidences were not included and post-reconstruction smoothing was not applied.

4.1.3.2 Process with ideal scatter correction

For the second strategy, the same process was followed but without scatter in both the simulation and reconstruction. These images can be interpreted as being reconstructed with perfect scatter elimination, but an approximate attenuation map. The simulated PET sinogram S' was produced by removing only the attenuation correction from the original PET sinogram. PET images were then reconstructed using the different μmaps to correct for attenuation only:

Simulation:

Input: True emission image E_T, true μmap μ_T
Output: Simulated PET sinogram S'
1: Forward project E_T
2: Simulate attenuation from μ_T
3: Combine to obtain simulated PET sinogram S'

Reconstruction:

Input: Simulated PET sinogram S' and other μmap μ_O
Output: Reconstructed PET image
1: Estimate attenuation from μ_O
2: Run OSEM using S' and the output of 1

The PET simulation and reconstruction process with ideal scatter correction (SC_{ideal}) is summarised in Fig. 4.2.

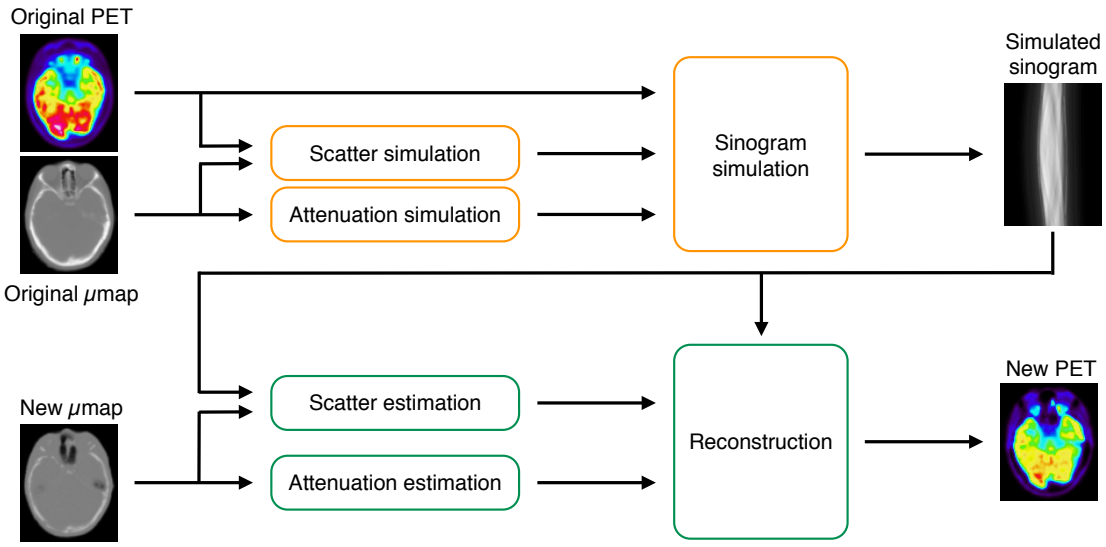

Figure 4.1: PET simulation and reconstruction process with μmap-specific scatter estimation.

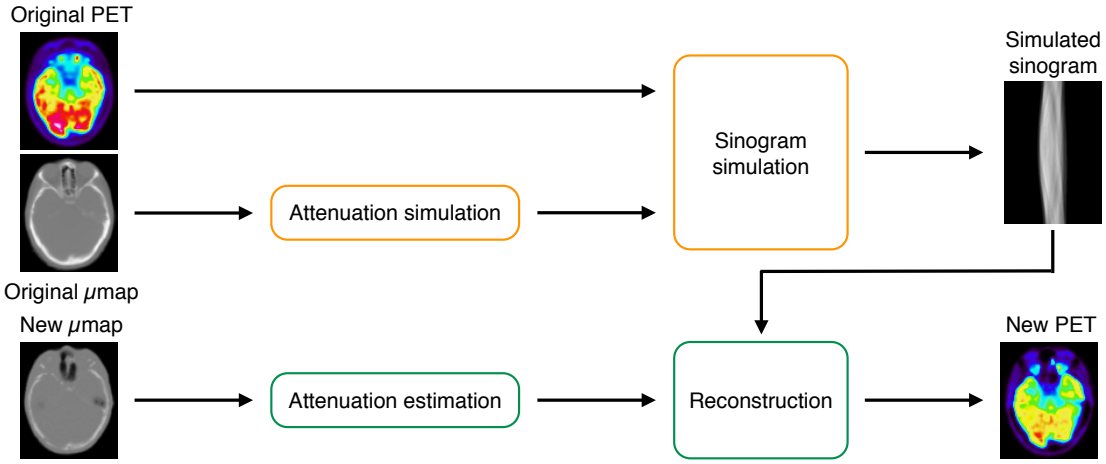

Figure 4.2: PET simulation and reconstruction process with ideal scatter estimation.

4.2 Results

For the three μmaps considered (CT, pCT and UTE-based), PET images were obtained using the simulation and reconstruction processes with both the μmap-specific and ideal scatter corrections.

Data

41 brain T1-w MRIs, CTs, UTE-derived μmaps and reconstructed PETs were used. These were the same data used in the previous chapter (section 3.2.1.2). The T1-w MRIs (3.0 T; TE/TR/TI, 2.63 ms/1700 ms/900 ms; flip angle 9°; voxel size 0.53 × 0.53 × 1.1 mm^3) and UTE μmaps (voxel size 1.562 × 1.562 × 1.562 mm^3) were acquired on a Siemens Biograph mMR hybrid PET/MR scanner; the CTs (voxel size 0.586 × 0.586 × 1.25 mm^3, 120 kVp, 300 mA) and reconstructed PETs (radiopharmaceutical: FDG; voxel size 1.953 × 1.953 × 3.27 mm^3) on a GE Discovery ST PET/CT scanner.

4.2.1 Effect of wrong μmap on scatter correction

In a first instance, I analysed, for the three μmaps, the difference between PET images simulated and reconstructed following the ideal scatter estimation process and PET images simulated and reconstructed following the μmap-specific scatter process. To do so, the relative mean absolute error, defined as $\text{rMAE} = 100 * \sum_v |I_v - J_v| / \sum_v J_v$, and the relative mean error, $\text{rME} = 100 * \sum_v (I_v - J_v) / \sum_v J_v$, were computed between the $\text{SC}_{\mu\text{map}}$ PET (I) and SC_{ideal} PET (J) images. Results obtained in the head and brain regions are shown in Table 4.1. Regardless of the μmap used, the rMAE between $\text{SC}_{\mu\text{map}}$ and SC_{ideal} PET images was small (less than 1% in the brain). Examples of μmaps and PET images are presented in Fig. 4.3 for a representative subject.

Table 4.1: For 41 subjects: Average and SD of the rMAE and rME between $\text{SC}_{\mu\text{map}}$ and SC_{ideal} PET images, for images reconstructed with three attenuation maps, in the full head and brain regions.

		Head			Brain		
		CT	pCT	UTE	CT	pCT	UTE
rMAE (%)	Average	1.27	1.37	1.45	0.81	0.85	0.88
	SD	0.14	0.15	0.16	0.07	0.08	0.08
rME (%)	Average	-0.92	-0.91	-0.81	-0.58	-0.59	-0.54
	SD	0.12	0.15	0.14	0.06	0.08	0.08

To localise the effects of the attenuation and scatter corrections, the PET images from the 41 subjects

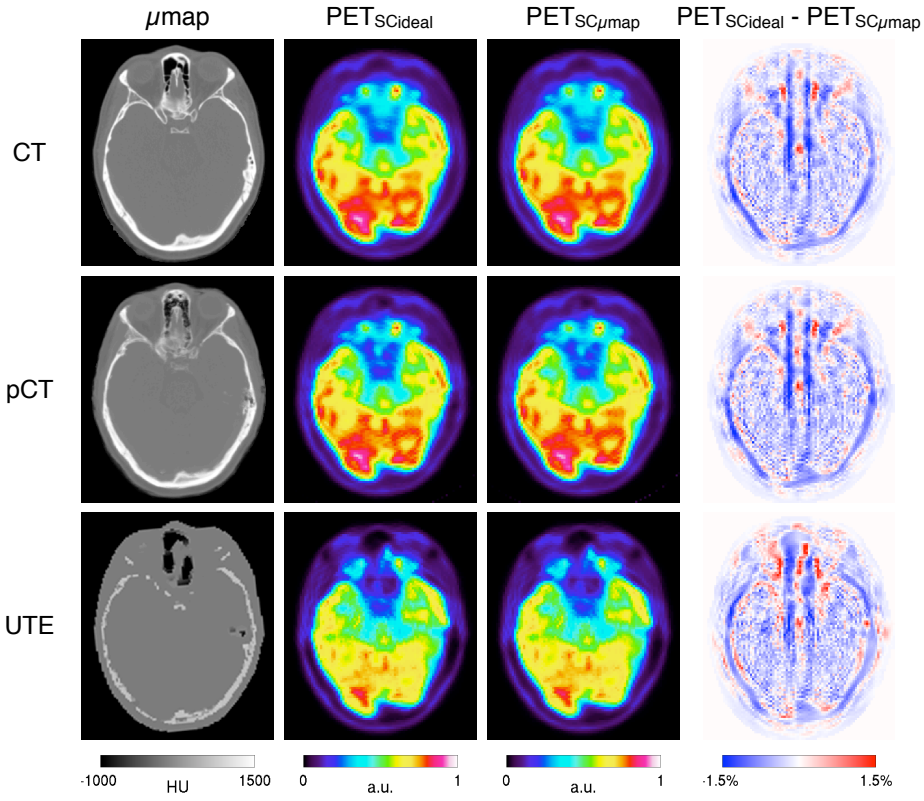

Figure 4.3: Example of μmap, PET image obtained with ideal (SC_{ideal}) and μmap-specific ($\text{SC}_{\mu\text{map}}$) scatter estimation and difference between SC_{ideal} and $\text{SC}_{\mu\text{map}}$ PETs, for the ground truth CT (top), the pseudo CT (middle) and the UTE μmaps (bottom).

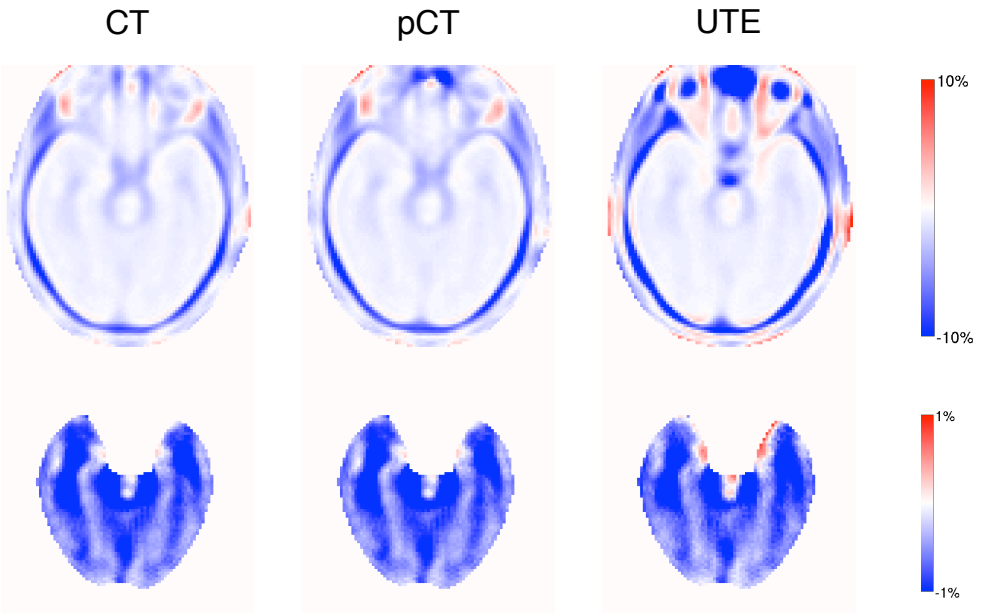

Figure 4.4: Difference, averaged over 41 subjects, between the PETs reconstructed with the ideal scatter correction and the PETs reconstructed with the μmap-specific scatter correction, for three attenuation maps, in the whole head (top) and brain region (bottom).

were mapped to a common space via a CT-based groupwise registration Rohlfing et al. (2001); Modat et al. (2014). Fig. 4.4 presents the difference, averaged across the 41 subjects, between $SC_{\mu map}$ and SC_{ideal} PET images, for the CT, pCT and UTE μmaps. These images confirmed the results presented in Table 4.1.

4.2.2 Effect of including scatter when comparing μmaps

In a second instance, I studied the effect of different scatter estimation processes when comparing MR-based μmaps to the reference CT μmap. The rMAE and rME were calculated for every subject between the reference PET (J), reconstructed using the CT μmap, and the PET images reconstructed using the pCT and UTE μmaps (I), for the head and brain regions. Results are shown in Table 4.2. Regardless of the scatter correction, the average rMAE obtained in the brain using the pCT μmap was four times smaller than the error obtained using the UTE μmap. For the subject shown in Fig. 4.3, I computed the difference between the CT and pCT PET images and between the CT and UTE PET images for both scatter estimation processes. The images are displayed in Fig. 4.5.

Using the groupwise analysis described in the previous section, averaged difference maps were computed between the reference PETs and the PETs reconstructed with the pCT and UTE μmaps, for both scatter estimation processes (Fig 4.6). As expected, regardless of the scatter estimation method, the difference between the reference and pCT PETs was lower than between the reference and UTE PETs, as the pCT-based attenuation provides more realistic μmaps.

Table 4.2: For 41 subjects: Average and SD of the rMAE and rME between the reference CT PET and both the pCT and UTE PETs, for the μmap-specific and ideal scatter processes, in the full head and brain regions.

		Head				Brain			
		$SC_{\mu map}$		SC_{ideal}		$SC_{\mu map}$		SC_{ideal}	
		pCT	UTE	pCT	UTE	pCT	UTE	pCT	UTE
rMAE (%)	Average	5.60	14.67	5.77	14.73	2.89	11.86	2.95	11.85
	SD	1.69	1.98	1.68	1.95	0.91	2.09	0.88	2.08
rME (%)	Average	-1.07	-13.71	-1.09	-13.61	0.15	-11.78	0.14	-11.74
	SD	2.58	2.15	2.52	2.14	2.12	2.13	2.10	2.13

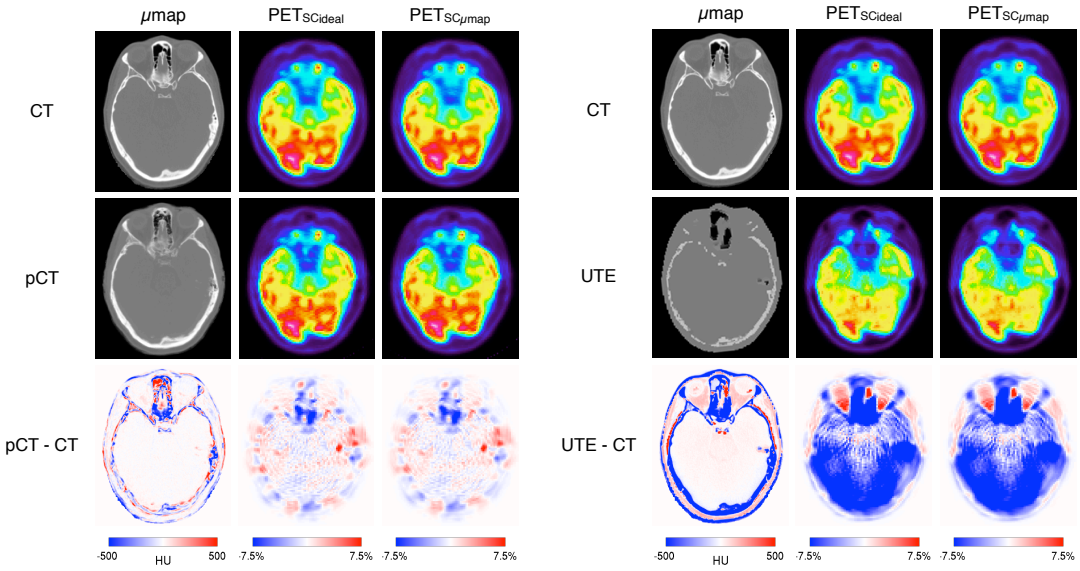

(a) pCT **(b)** UTE

Figure 4.5: Examples of MR-based μmaps ((a): pCT μmap, (b): UTE μmap), PET images corrected for attenuation using the CT μmap, PET images corrected for attenuation using the MR-based μmap, for the μmap-specific scatter estimation and the ideal scatter estimation, and difference images.

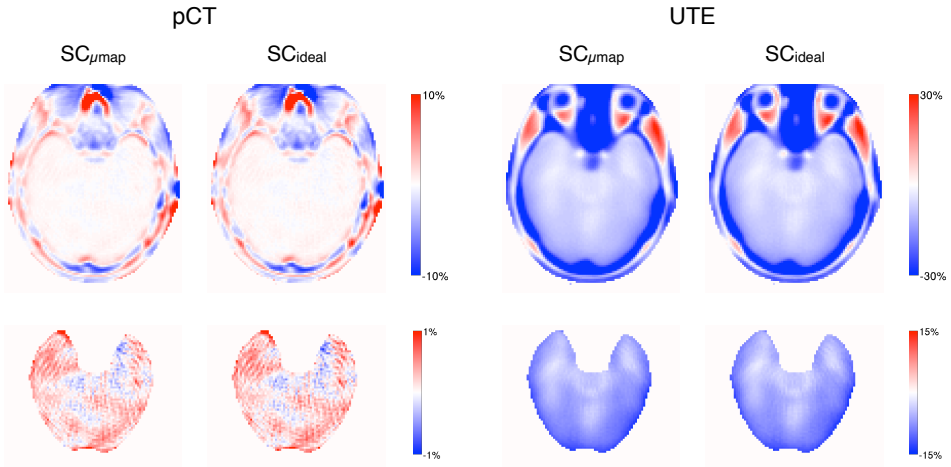

Figure 4.6: Average over 41 subjects of the difference between the PETs reconstructed with the ground truth CT μmap and the PETs reconstructed with the pCT μmap (left) or the UTE μmap (right), for both μmap-specific and ideal scatter estimation, in the whole head (top) and brain region (bottom).

4.3 Conclusion

This chapter presents an analysis of the effects of imperfect attenuation maps on the scatter correction. Regardless of the μmap used in the reconstruction, the difference on PET images between μmap-specific and ideal scatter estimation is small, particularly in the brain region (maximum average difference of 0.88% for the worst method). More importantly, the relative error between attenuation correction methods does not change depending on the scatter estimation method included in the simulation and reconstruction process. This means that the effect of errors in the μmap on the PET image is dominated by the attenuation correction, while the scatter estimate is relatively unaffected. Therefore, while scatter correction improves reconstruction accuracy, it is unnecessary to include scatter in the simulation when comparing different attenuation correction methods.

The current analysis used FDG brain images. The conclusions could be different for tracers such as F-DOPA with uptake in specific regions, or for the thorax.

Chapter 5

CT synthesis: building the optimal database

The CT synthesis method presented in chapter 3 strongly relies on the database of T1-w MR and CT images. In this chapter, I want to determine if an optimal number of atlases exists and, as suggested by Marshall et al. (2013), if demographic characteristics such as the subject's gender and age have an influence on the accuracy of the pseudo CT generated. Finally, based on these results, I want to determine if the synthesis can be improved by pre-selecting atlases as a means to deal with large databases. I will assess if this pre-selection should be based on demographic characteristics or on the images themselves.

5.1 Data acquisition and database processing

5.1.1 Data

The dataset considered in this chapter is composed of 92 brain T1-weighted MR and CT images. 70 subjects were part of an epilepsy study while 22 took part in a dementia study. None of the subjects present abnormalities affecting the skull. For the epilepsy study, the T1-weighted MPRAGE MR images (3.0 T; TE/TR/TI, 2.63 ms/1700 ms/900 ms; flip angle 9°; voxel size 0.53 $\times$ 0.53 $\times$ 1.1 mm^3) were acquired on a Siemens Biograph mMR hybrid PET/MR scanner and the CT images (voxel size 0.59 $\times$ 0.59 $\times$ 1.25 mm^3, 120 kVp, 300 mA) on a GE Discovery ST PET/CT scanner. For the dementia study, the T1-weighted MPRAGE MR images (3.0T; TE/TR/TI, 2.9 ms/2200 ms/900 ms; flip angle 10°; voxel size 1.1 $\times$ 1.1 $\times$ 1.1 mm^3) were acquired on a Siemens Magnetom Trio scanner and the CT images (voxel size 0.59 $\times$ 0.59 $\times$ 2.5 mm^3, 120kVp, 300mA) on a GE Discovery ST PET/CT scanner.

The dataset comprises 46 females (F) and 46 males (M), with an average age of 42.1 years (F: 41.3, M: 42.8, no significant difference). The age distribution is displayed in Figure 5.1.

5.1.2 Database processing

For each subject, the MR image was mapped to the CT dataset using an affine registration (Modat et al., 2010). The MR image from the all the subjects were then mapped to a common coordinate frame via an affine groupwise registration (Rohlfing et al., 2001; Modat et al., 2014). Finally, the transformations were applied to the MR-CT pairs by updating their image coordinate system, forming a database of MR and CT images aligned in a common space.

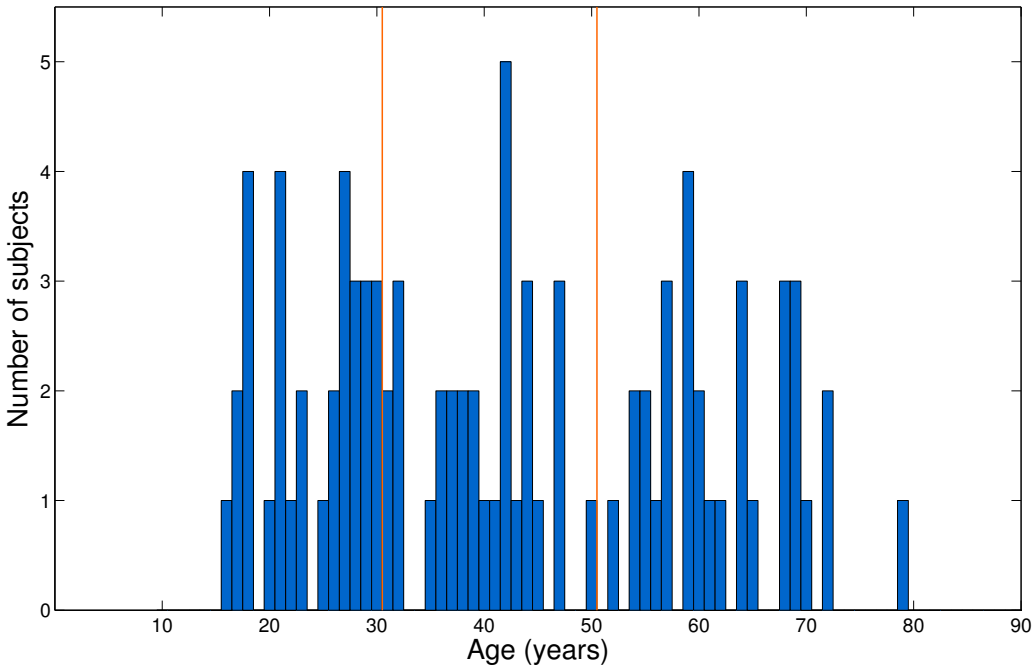

Figure 5.1: Age distribution of the 92 subjects used in the different experiments.

5.2 Optimal number of atlases

In this section, I evaluate how changes in the size of the MR-CT database influence the synthesis accuracy. For each number of atlases studied, $N_A = [1\ 2\ 5\ 10\ 15\ 20\ 25\ 30\ 35\ 40\ 45\ 50]$, 150 pseudo CTs were synthesised by selecting both the targets and atlases randomly. For each of the 30 repetitions, five targets were randomly selected from the pool of 92 subjects and the atlases were randomly picked from the remaining subjects.

The mean absolute error and the mean error, defined as $\text{MAE} = \frac{1}{N_R}\sum_{v\in R}|pCT_v - CT_v|$ and $\text{ME} = \frac{1}{N_R}\sum_{v\in R}(pCT_v - CT_v)$, were then calculated between the reference CT and each of the pseudo CTs, in a region of interest R comprising N_R voxels. This region of interest is limited to a mask defined by segmenting the head from the background using both the reference CT and T1 images. Statistical significance was assessed using a paired t-test at the 5% significance level.

Figure 5.2 displays the average MAE and ME obtained for the different sizes of database. The absolute error decreases as the number of subjects in the database increases, which confirms the intuition that adding subjects to the database improves the chances of finding subjects similar to each other. Once the database reaches 15 subjects, the bias appears to be limited and stable.

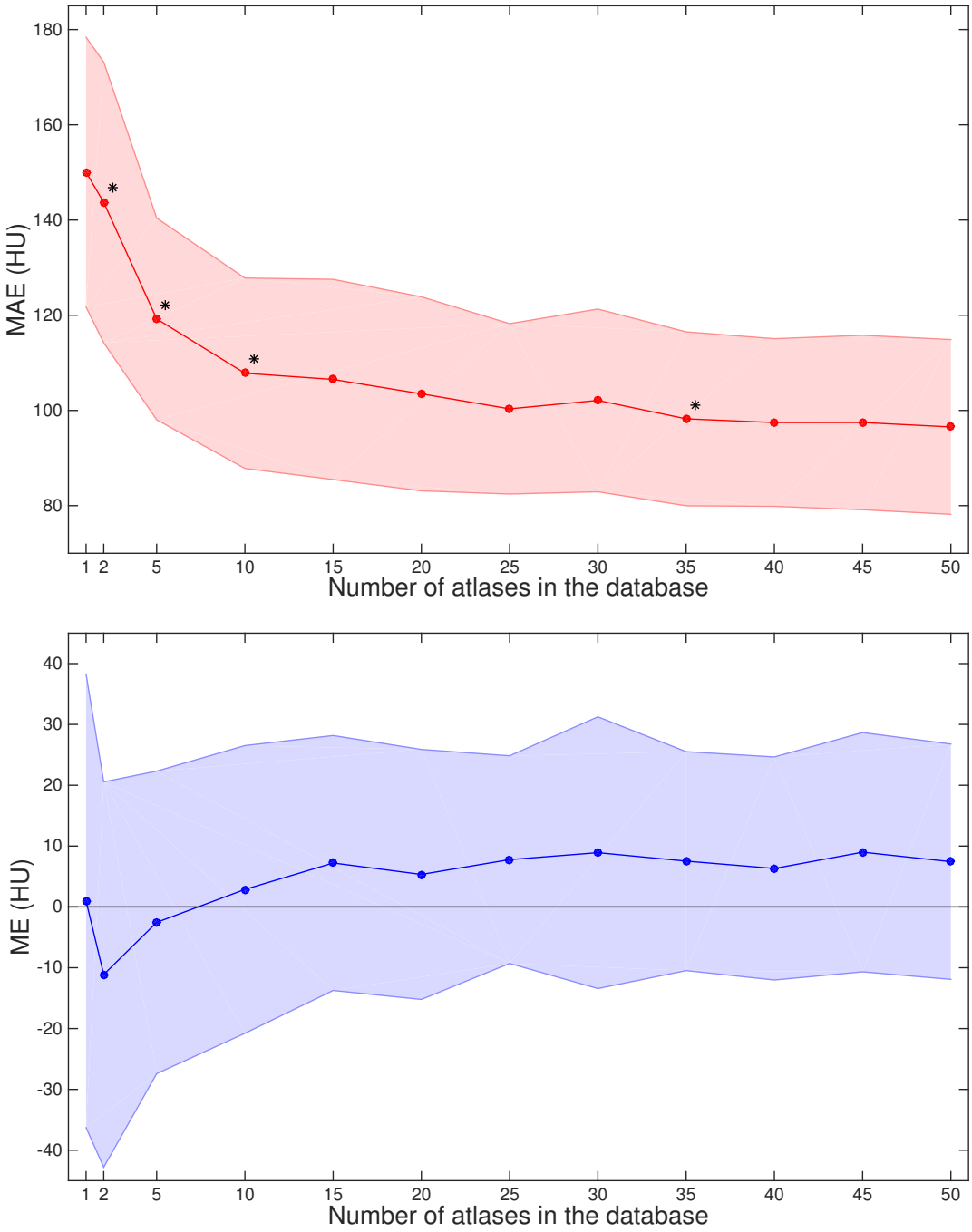

Figure 5.2: Average (solid line) ± SD (shaded areas) of the MAE (top) and ME (bottom) computed between the reference CT and each of the pseudo CTs as a function of the number of subjects in the MR-CT database. The black stars indicate a significant improvement ($p < 0.05$) between the current and previous measurements.

5.3 Dependence on demographic features

5.3.1 Age

Based on the age distribution (Figure 5.1), I divided the 92 subjects into three groups: below 30 years old, between 30 and 50, and above 50, thus creating three sub-databases: - 30, 30 - 50 and + 50. Details regarding the three groups are provided in the table below.

Table 5.1: Gender and age characteristics of the subjects forming the three age-specific sub-databases.

	- 30	30 - 50	+ 50
Number of subjects (females)	31 (19)	30 (12)	31 (15)
Median age (years)	25.0	40.5	61.0
Mean $\pm$ SD age (years)	23.9 ± 4.6	39.8 ± 5.2	62.5 ± 6.6

To explore the influence of the age of the subjects forming the MR-CT database on the synthesis accuracy, I generated three pseudo CTs for each target using the three sub-databases following a cross-validation scheme. This scheme is a generalisation of balanced repeated K-fold cross-validation. When $N = A - n$ subjects of each age category were to be used as atlases (per database) in L repeats, the n to be held out for testing were randomly selected in the following way: each subject was given an integer counter, initially zero, representing the number of times they had been left out so far. To select the n of each age category at each repeat in sequence, as many subjects as possible (up to n) with the minimum counter value were drawn (randomly without replacement). Then, if that number was less than n, subjects with the higher counter value were drawn. All subjects drawn had then their counters incremented by one. In this way, only two counter values exist at any time. When $Lq = A/n$ for integer q and $L = A/n$, this is equivalent to balanced K-fold cross-validation fully repeated q times.

The mean absolute differences computed between the reference CT and the pseudo CTs obtained from the three sub-databases are plotted for each target age group in Figure 5.3. The MAE is lower when the pseudo CT is generated using the database whose age range matches the target's age and increases when the age difference between the target and the atlases augments.

5.3.2 Gender

The influence of the atlases' gender on the synthesis accuracy was evaluated by creating three sub-databases: only females (23 subjects, average age: 55.8 years), only males (23 subjects, average age: 55.5 years) and mixed (combination of the female and male databases). To reduce the variability introduced by differences in the subjects' age, only the subjects above 40 years old were selected. I then generated three pseudo CTs for each target using the three sub-databases following a cross-validation scheme, as described in the previous section.

The mean absolute differences computed between the reference CT and the pseudo CTs obtained from the three sub-databases are plotted for both the female and male targets in Figure 5.4. The MAE is lower when the pseudo CT is generated using the database whose gender matches the target's gender and increases when the database is formed of both genders and of the opposite gender. Note that the

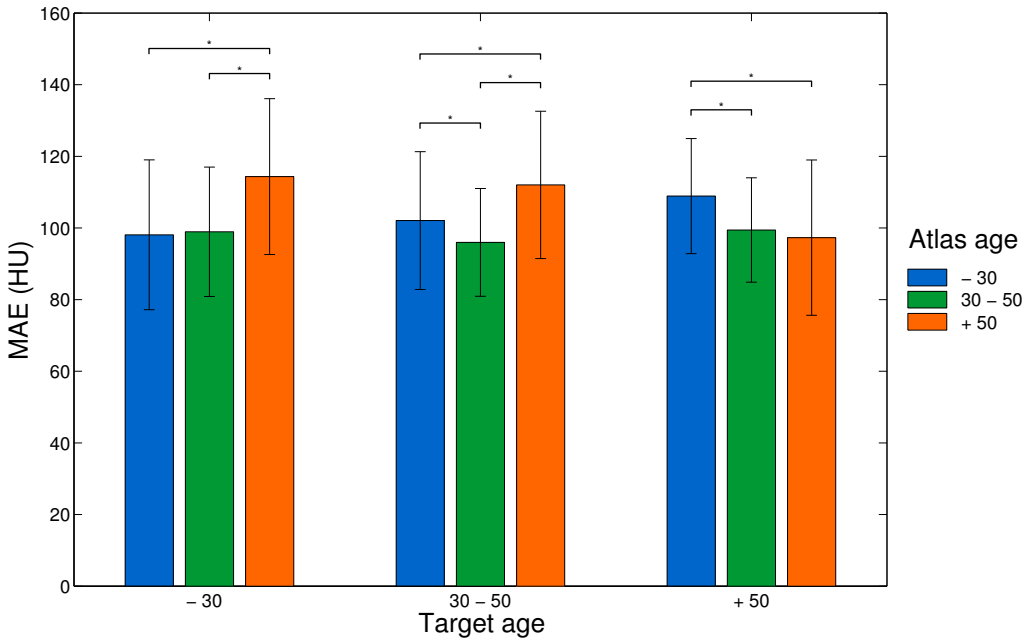

Figure 5.3: Bar plots displaying the averaged MAE computed between the reference CTs and the pseudo CTs obtained from databases covering three age ranges. The error bars represent twice the standard deviation and the stars indicate a significant improvement ($p < 0.05$) between two measurements.

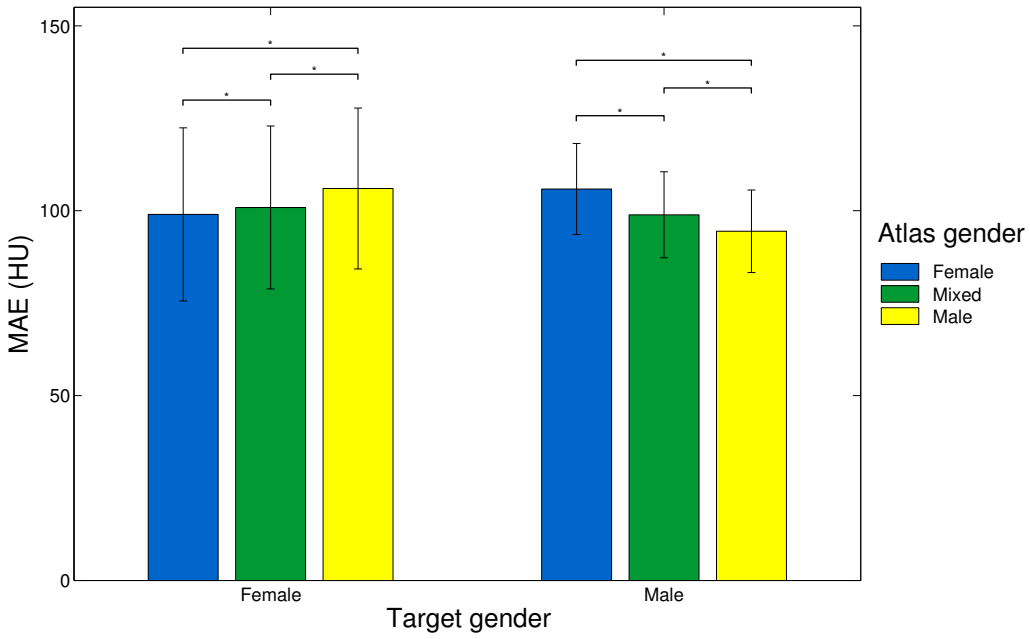

Figure 5.4: Bar plots displaying the averaged MAE computed between the reference CTs and the pseudo CTs obtained from a female only, male only or mixed database. The error bars represent twice the standard deviation and the stars indicate a significant improvement ($p < 0.05$) between two measurements. Note the larger the standard deviations for the female targets.

standard deviation, no matter the database, is higher for the female targets than for the male targets. This difference can be explained by the fact that the skull bone density of males remains constant during lifetime, while the female skull bone density slowly decays (Schulte-Geers et al., 2011), thus potentially introducing more variability in the female subjects.

5.4 Atlas pre-selection

We saw in section 5.2 that increasing the number of subjects in the database improves the synthesis accuracy. However, increasing the number of atlases reduces the computational efficiency. The results in section 5.3 showed that the demographic characteristics of the subjects forming the MR-CT database influence the quality of the pseudo CTs. To improve the synthesis while limiting the computational cost, I propose to pre-select the subjects forming the database, strategy that has shown benefits in the context of multi-atlas segmentation of brain images (Aljabar et al., 2009). In this section, I explore if the pre-selection should be based on the demographic features or if it could be extracted from the images themselves.

5.4.1 Pre-selection strategies

For all the targets defined in section 5.2 for $N_A = 20$ atlases, I synthesised pseudo CTs using three pre-selection strategies, based either on the demographic characteristics of the targets (gender, age) or directly on the MR images.

Feature-based pre-selection using demographic data In the feature-based pre-selection, only the atlases of the same gender as the target were selected. The 20 atlases closest in terms of age to the target were then picked.

Image-based pre-selection using global image similarity The image-based strategy selects the atlases according to their global morphological similarity to the target, as assessed by a global similarity measure, the normalised cross-correlation (NCC). An atlas from the database was first affinely aligned to the target. Because all the atlases are aligned with each other (section 5.1.2), this transformation was used to align all the atlases to the target. The NCC was then computed between each aligned atlas J_n and the target I as follows:

$$\text{NCC} = \frac{1}{N_x} \sum_x \frac{\left(I(x) - \overline{I}\right)\left(J_n(x) - \overline{J_n}\right)}{\sigma(I)\,\sigma(J_n)} \tag{5.1}$$

where N_x is the number of voxels x in I and J_n, $\overline{I}$ is the average of I and $\sigma(I)$ its standard deviation. Finally, the 20 atlases with the highest NCC were picked.

Feature + Image-based pre-selection The last pre-selection strategy consists of combining the feature- and image-based approaches. Thirty-two atlases were first selected based on their gender and age as described above. The NCC was then computed between the 32 atlases and the target. Finally, the 20 atlases with the highest NCC were selected.

Results The average $\pm$ SD of the MAE and ME computed between the reference CT and the pseudo CTs are presented in Table 5.2 for the different pre-selection strategies. Note that the random pre-selection is described in section 5.2. When pre-selecting atlases based on their demographic characteristics or morphology, the MAE significantly decreases when compared to a random pre-selection. No significant differences were found between the pre-selection strategies. Instead, a correlation coefficient of 0.937 was found between the feature- and image-base strategies.

Table 5.2: Average ± SD of the MAE and ME computed between the reference CT and the pseudo CTs synthesised from 20 atlases pre-selected using different strategies.

	Random	Feature	Image	Feature + Image
MAE (HU)	103.5 ± 20.3	95.0 ± 19.1	93.8 ± 17.5	94.4 ± 19.3
ME (HU)	5.4 ± 20.5	2.3 ± 14.5	4.3 ± 15.7	3.4 ± 15.4

5.4.2 Pre-selection depending on the number of atlases

To further explore the benefits of pre-selecting the atlases forming the MR-CT database based on a subject-specific criterion, I synthesised pseudo CTs for different database sizes, as done in section 5.2. I chose the pre-selection strategy leading to the lowest MAE when $N_A = 20$ according to Table 5.2, the image-based pre-selection. The average MAE and ME displayed in Figure 5.5 show that, no matter the number of atlases selected, the image-based pre-selection produces more accurate results than the random pre-selection. We can also see that, with the pre-selection, the results converge to a plateau value once the database contains 15 atlases.

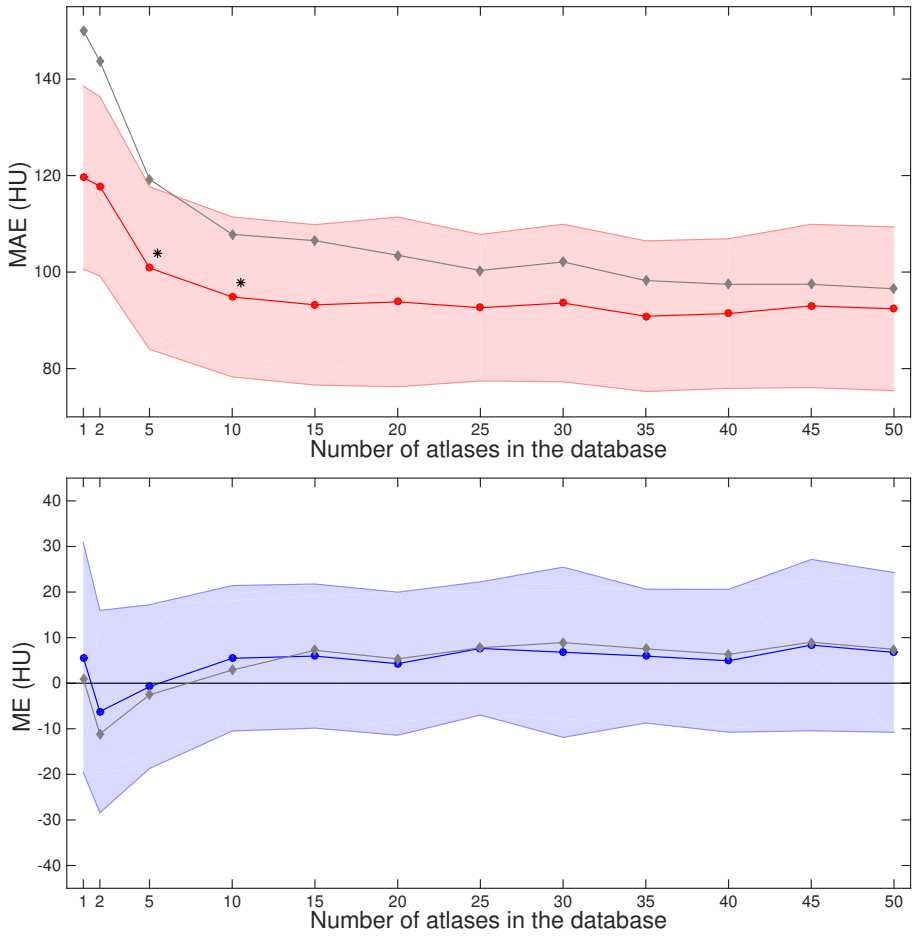

Figure 5.5: Average (solid line) ± SD (shaded areas) of the MAE (top) and ME (bottom) computed between the reference CT and each of the pseudo CTs synthesised following the image-based pre-selection strategy as a function of the number of subjects in the MR-CT database. The black stars indicate a significant improvement between the current and previous measurements. The grey curves correspond to the results obtained by randomly selected the atlases, as previously displayed in Figure 5.2.

5.5 Conclusion

The CT synthesis method presented in chapter 3 depends on an MR-CT database. Having a database as representative as possible is crucial to guarantee accurate and robust CT synthesis results. In this chapter, I have confirmed that increasing the number of atlases in the database reduces the synthesis error, and demonstrated that the synthesis accuracy increases when target and atlases share similar demographic features (gender and age).

As dealing with a very large database would dramatically increase the computational cost, I proposed to pre-select atlases based on their demographic features and/or directly on their structural MR images. The three target-specific pre-selection strategies led to a reduced synthesis error when compared to a random pre-selection. The results obtained with the feature-based and image-based strategies were highly correlated, which suggests that T1-w MR images can act as a surrogate for the demographic features. Another advantage is that the image-based pre-selection does not require any metadata, important when dealing with anonymised data. Finally, the value itself of the normalised cross-correlation used for the image-based pre-selection could be exploited to detect if a new subject is not well represented in the database and raise a warning.

These results suggest that, when the database is large enough, pre-selecting atlases based on their global morphological similarity with the target can help improve the synthesis accuracy while maintaining a reasonable computational time. Note that small databases appear to be more strongly dependent on the demographic features and selection processes than the large databases.

Chapter 6

CT synthesis: novel similarity metric and MRI contrasts

While providing an accurate CT synthesis, the MR-based attenuation correction method presented in chapter 3 suffers from several limitations. First, because most PET/MR and PET/CT scanners have different gantry sizes, the field of view of the MR images usually contains the head and neck of the subject, while in the CT FOV only the head is visible, which can lead to mismatching information when images from the two modalities are aligned. A similar mismatch can occur with the inter-subject mapping. This problem is illustrated in Figure 6.1. If the mismatch between FOVs is not taken into account in the registration and image similarity estimation processes, severe underestimation of the μmap can occur. Second, the algorithm relies on high resolution T1-w brain images, which might not always be available to perform attenuation correction and whose low intensities in the bone/air/CSF interfaces might limit the inter-subject registration accuracy.

In this chapter, I build upon the CT synthesis method previously developed and propose two main improvements: enabling a better estimation of the local image similarity and extending the algorithm to other MRI contrasts. Some of the methods and results presented have been published in Burgos et al. (2015a).

6.1 Novel metric

6.1.1 Convolution-based ROI-LNCC

Due to different acquisition FOVs, the inter-subject mapping and resampling processes introduce areas where no information is available, which can lead to severe underestimation of the μmap. Those areas have to be accounted for when the similarity measure is computed and during the intensity fusion process. To do so, I extended the convolution-based local normalised correlation coefficient (LNCC) method by Cachier et al. (2003) to irregular regions-of-interest.

Let the target subject's MR image be denoted by I^{MRI} and, for each of the N atlases in the database, let the mapped MR images of atlas n be denoted by J_n^{MRI}. The ROI-LNCC between I^{MRI} and J_n^{MRI} at voxel v is then given by

$$\text{ROI-LNCC}_{n,v} = \frac{\langle I^{MRI}, J_n^{MRI} \rangle_v}{\sigma(I^{MRI})_v \, \sigma(J_n^{MRI})_v} \quad . \tag{6.1}$$

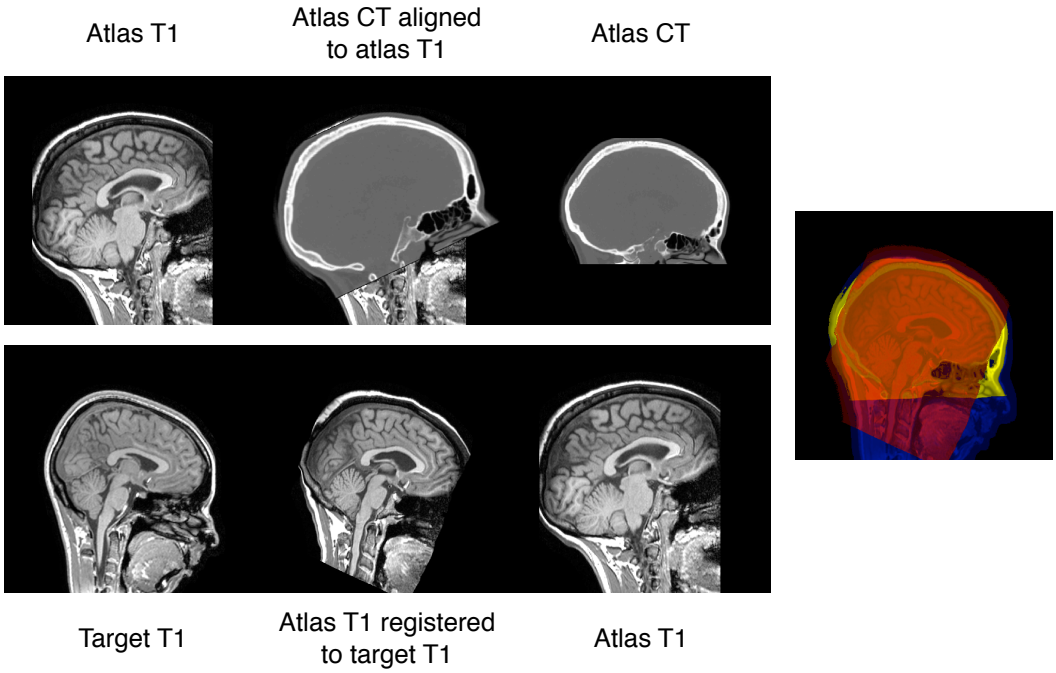

Figure 6.1: Left: Both the intra-subject CT to MRI mapping (top) and inter-subject MRI to MRI mapping (bottom) can lead to mismatching information. Right: The fusion must be restricted to the area where the target T1 (blue), the atlas T1 (red) and atlas CT (yellow) coincide.

Let Ω be a density function of size M equal to 1 where the fields of view overlap, and 0 otherwise. The means and standard deviations at voxel v were calculated using a Gaussian kernel G_{σ_G} with standard deviation σ_G through density normalised convolution

$$\bar{I}_v = \frac{\left[G_{\sigma_G} * I\right]_v}{\left[G_{\sigma_G} * \Omega\right]_v} \qquad \sigma(I)_v = \sqrt{\overline{I^2}_v - \bar{I}_v^2} \qquad \langle I,J\rangle_v = \overline{I \cdot J}_v - \bar{I}_v \cdot \bar{J}_v \ ,$$

where $*$ denotes the convolution operator and $G_{\sigma_G} * \Omega$ represents a density normalisation term that compensates for areas with missing information. As the values of LNCC are only valid within the bounds of the FOV, LNCC values outside the FOV were set to $-\infty$. The ROI-LNCC at each voxel was then ranked across all atlas images and the ranks were converted to weights by applying an exponential decay function. These weights were used in a spatially varying weighted averaging to reconstruct the target CT (chapter 3).

6.1.2 Impact of the novel metric on the synthesis accuracy

T1-weighted MRI data and T1/CT database building

Twenty-two sets of T1-weighted MRI and CT brain images were used to build the MR-CT database and validate the method. The T1-w MPRAGE (3.0T; TE/TR/TI, 2.9ms/2200ms/900ms; flip angle 10°; voxel size 1.1 × 1.1 × 1.1 mm^3) MR images were acquired on a Siemens Magnetom Trio scanner and the CT (voxel size 0.59 × 0.59 × 2.5 mm^3, 120kVp, 300mA) images on a GE Discovery ST PET/CT scanner. To build the database, the T1-w image of each subject was corrected for intensity non-uniformity (Sled et al., 1998) and affinely aligned to CT image.

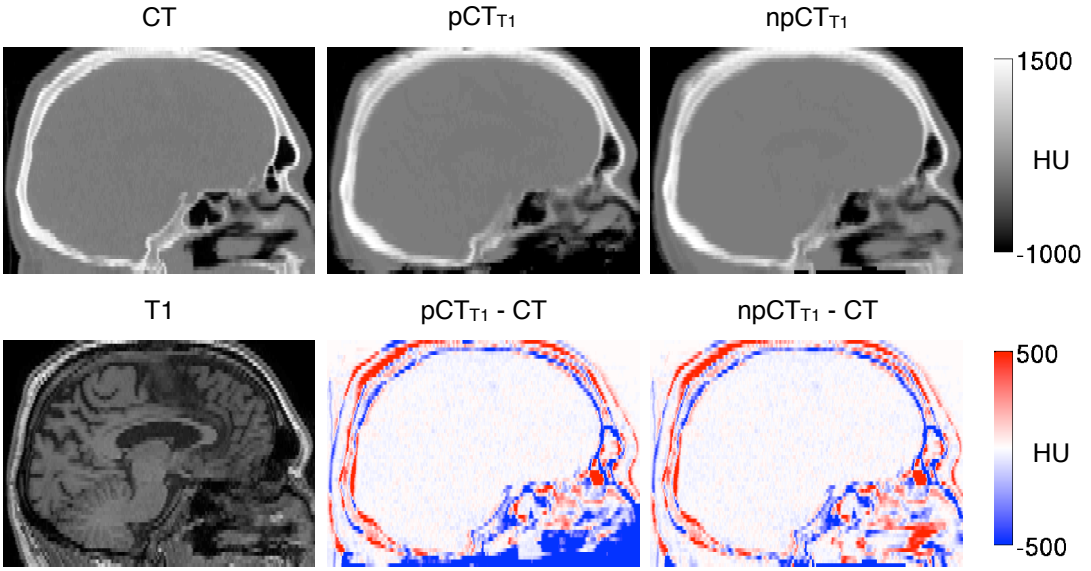

Figure 6.2: For a representative subject, the reference CT,the pseudo CTs synthesised using the LNCC (pCT$_{T1}$) and the ROI-LNCC (npCT$_{T1}$) (top); and the acquired T1 and difference images between the pseudo CTs and the reference CT (bottom).

6.1.2.1 Algorithmic comparison

The performances of the LNCC and ROI-LNCC were compared with reference data for 22 subjects following a leave-one-out cross-validation scheme. For each subject, two pseudo CTs were synthesised using a database of 21 subjects:

- pCT$_{T1}$ using the method described in chapter 3 given the T1 image;
- npCT$_{T1}$ using the ROI-LNCC on the T1 image;

For every subject, the mean absolute error and the mean error, defined as

$$\text{MAE} = \frac{1}{N_R}\sum_{v\in R}|pCT_v - CT_v| \qquad \text{and} \qquad \text{ME} = \frac{1}{N_R}\sum_{v\in R}(pCT_v - CT_v) \ ,$$

were calculated between the reference CT and each of the pseudo CTs, in a region of interest R comprising N_R voxels. This region of interest was limited to a mask defined by segmenting the head from the background using the reference CT. Statistical significance was assessed using the paired, one-tailed, Wilcoxon signed-rank test.

To localise the error and bias introduced by each approach, the reference CTs and pseudo CTs from the 22 subjects were mapped to a common space via a groupwise registration (Rohlfing et al., 2001; Modat et al., 2014). Difference maps were then computed between the reference CT and the pseudo CTs and averaged across all the subjects. Results are presented using a mean intensity projection: the mean value along a projection line is assigned to the pixel represented on the projected image.

6.1.2.2 Results

The average and standard deviation (SD) of the MAEs and MEs computed in the full head are presented in Table 6.1. Using the ROI-LNCC (section 6.1.1) instead of the classical LNCC (chapter 3) significantly ($p < 10^{-4}$) decreased the MAE. An example of reference CT and pseudo CTs is presented in Figure 6.2.

Table 6.1: Average ± SD of the MAE and ME computed for the full head between the reference CT and the pseudo CTs synthesised from a T1-w MR image using the LNNC (pCT_{T1}) and the ROI-LNCC ($npCT_{T1}$), and from a T2-w MR image using the ROI-LNCC ($npCT_{T2}$).

	pCT_{T1}	$npCT_{T1}$	$npCT_{T2}$
MAE (HU)	122.2 ± 21.5	91.4 ± 10.5	91.1 ± 8.3
ME (HU)	-38.7 ± 22.2	3.0 ± 16.2	6.5 ± 17.0

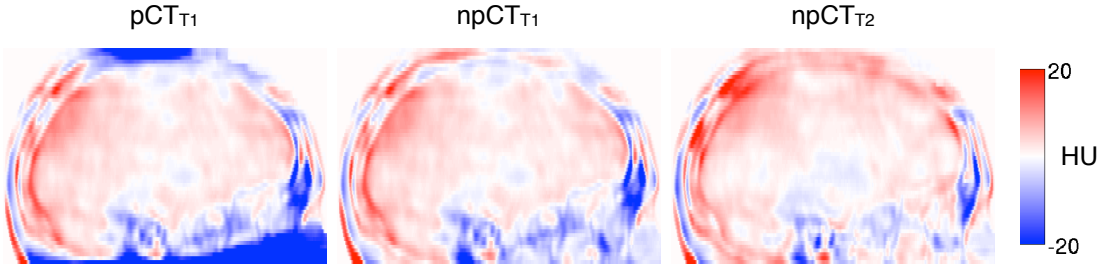

Figure 6.3: Mean intensity projection of the difference, averaged over 22 subjects, between the reference CT and the pseudo CTs synthesised from a T1-w MR image using the LNNC (pCT_{T1}) and the ROI-LNCC ($npCT_{T1}$), and from a T2-w MR image using the ROI-LNCC ($npCT_{T2}$).

The difference maps computed between the reference CT and the pseudo CTs, and averaged across all the subjects, are presented in Figure 6.3. Large errors at the top and bottom of the head, when the LNCC from chapter 3 was used, disappeared when the FOVs were properly handled.

6.2 Novel MRI contrasts

6.2.1 Synthesis from T2-weighted MR images

The algorithm described in chapter 3 relies on the ability to accurately register T1-w brain images from different subjects, a process that can be challenging in areas with low intensities, such as the sinuses and the bone/dura/CSF boundary. Contrary to T1-w MR images, where bone, air and CSF have low intensities, T2-w MR images allow the differentiation of the high CSF intensities from the low intensities of bone and air.

T2-weighted MRI data and T2/CT database building

On top of the 22 sets of T1-weighted MRI and CT brain images detailed in section 6.1.2, 22 T2-weighted MRI (3.0T; TE/TR, 401ms/3200ms; flip angle 120°; voxel size 1.1 × 1.1 × 1.1 mm^3) of the same subjects were available. The T2-w image of each subject was corrected for intensity non-uniformity (Sled et al., 1998) and affinely aligned to the CT image to extend to MR-CT database.

Comparison between T1-based and T2-based CT synthesis

Leave-one-out cross-validation was used to synthesise a pseudo CT ($npCT_{T2}$) for each subject in the dataset using the ROI-LNCC described in section 6.1.1 given the T2 image.

The average and SD of the MAEs and MEs computed in the full head are presented in Table 6.1. Synthesis from a T2-w image achieves similar accuracy as synthesis from a T1-w image. An example of pseudo CTs obtained from a T1-w and a T2-w image is displayed in Figure 6.4. The synthesis in the

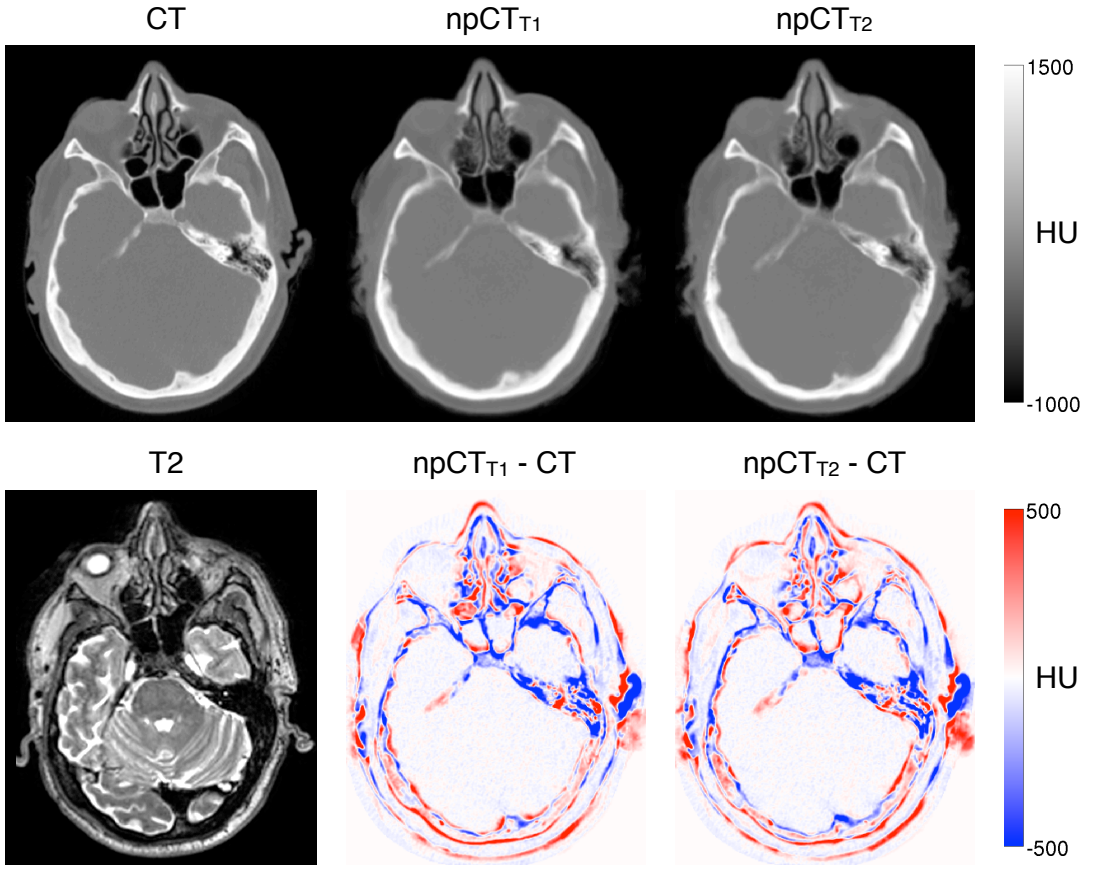

Figure 6.4: For a representative subject, the reference CT,the pseudo CTs synthesised from a T1-w (npCT$_{T1}$) and a T2-w (npCT$_{T2}$) MR image (top); and the acquired T2 and difference images between the pseudo CTs and the reference CT (bottom).

sinus region appears slightly more accurate when based on the T2. This is confirmed by the difference maps computed between the reference CT and the pseudo CTs and averaged across all the subjects, which are presented in Figure 6.3. With the T2, the mean error is lower in the sinus and frontal regions when compared with the T1 but it is higher in the occipital region.

6.2.2 Synthesis from LAVA-Flex images

If a volumetric T1-w image is acquired during most MRI protocols, this is not an obligation. However, during PET/MR acquisitions, sequences dedicated to attenuation correction are systematically acquired. This is for example the case of the liver accelerated volume acquisition (LAVA)-Flex on the SIGNA PET/MR system (GE Healthcare). LAVA-Flex is a 3D fast spoiled gradient echo imaging technique that, similarly to the Dixon sequence, generates four low resolution images (water-only, fat-only, in-phase and out-of-phase) in a single acquisition lasting less than 20 s. In this section, I assess if the multi-atlas CT synthesis method is able to generate accurate results from low resolution LAVA-Flex images. This work was done in collaboration with Dr. Tetsuro Sekine and Dr. Gaspar Delso from the University of Zurich, Switzerland.

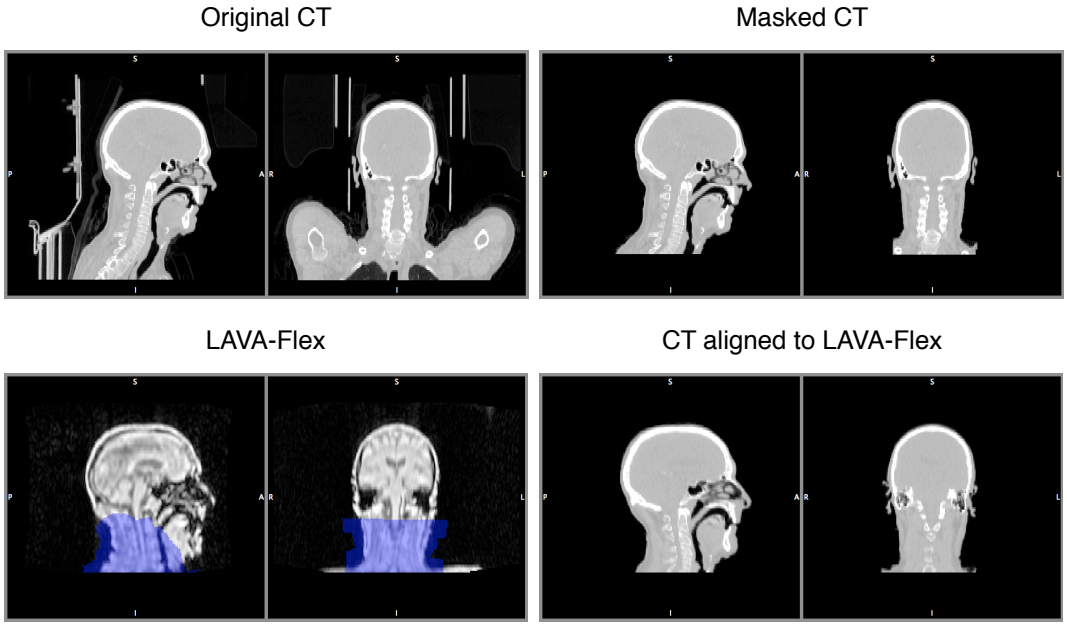

Figure 6.5: LAVA-Flex/CT database building. The original CT image is masked to remove the bed and arms and facilitate the affine alignment to the LAVA-Flex image. The CT is non-rigidly aligned to the MR image in the neck area (blue) to compensate for changes in position between the PET/CT and PET/MR acquisitions.

LAVA-Flex data

Twenty-three sets of LAVA-Flex and CT brain images were used to build the LAVA-CT database and to validate the method. The LAVA-Flex images (TR 4 ms, TE 2.23 ms, flip angle 5 degrees, slice thickness 5.2 mm with 2.6 mm overlap, 120 slices, pixel size 1.95×1.95 mm^2, acquisition time: 18 s) were acquired on a GE SIGNA TOF PET/MR scanner and the CT images (120 kV, 15 to 80 mA with automatic dose modulation, rotation time 0.5 s, helical thickness 3.75 mm, pitch 39.37 mm/rot, matrix size 512×512, slice thickness 3.3 mm, pixel dimensions 1.4×1.4 mm^2) on a GE Discovery 690 TOF PET/CT scanner.

6.2.2.1 Method

Building the LAVA-Flex/CT database The LAVA-Flex images were first corrected for intensity non-uniformity. The preprocessing of the CT images consisted of extracting the head from the bed and removing the arms when visible in the FOV to later facilitate the alignment to the LAVA-Flex image. To do so, I performed an affine groupwise registration on all the CT images and created in the group space a rough mask excluding the bed and arms. This mask was transported back to each subject's space and applied to the CT image. I then used morphological operators to refine the masks, and finally checked and rectified each CT image slice by slice.

To build the database, the CTs were first affinely aligned to the LAVA images. To account for the different positions between the PET/CT and PET/MR acquisitions, the alignment between the CT and LAVA-Flex images was refined using a non-rigid registration limited to the neck region to preserve the skull. The main steps of the database building are illustrated in Figure 6.5.

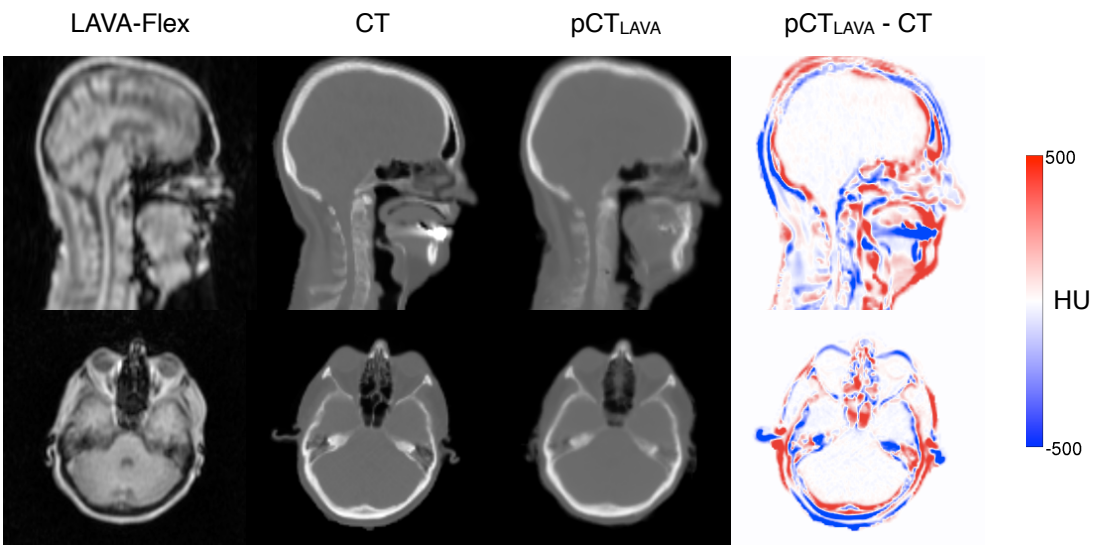

Figure 6.6: For a representative subject, the LAVA-Flex image, the reference CT, the pseudo CT synthesised from the LAVA-Flex image, and the difference image between the pseudo CT and the reference CT.

Inter-subject mapping and intensity fusion As in section 3.1, the inter-subject coordinate mapping between the LAVA-Flex images from the database and the target was obtained using a symmetric global registration followed by a cubic B-spline parametrised non-rigid registration, using normalised mutual information as a measure of similarity (Modat et al., 2010). The CTs were then mapped to the target using the same transformation and fused according to the morphological similarity between the atlas and target MR images, assessed using the ROI-LNCC.

6.2.2.2 Results

For each of the 23 subjects in the LAVA-Flex dataset, I synthesised a pseudo CT (pCT_{LAVA}) following a leave-one-out scheme. On average, the MAE computed between the reference CT and the pseudo CT was 106 $\pm$ 9 HU and the ME -1 $\pm$ 13 HU. The error is higher than the error obtained when synthesising from T1-w or T2-w images. This is explained by the lower resolution of the LAVA-Flex images and by the fact that, contrary to the T1-w and T2-w images, the neck, where most of the errors are located, is largely visible in the LAVA-Flex images. An example is displayed in Figure 6.6.

6.3 Robustness to different MRI contrasts

We have seen in the previous sections that several MRI sequences are suited for the synthesis of CT images. In all the scenarios studied, target and MR atlases shared the same contrast. However, in practice, a database matching the target contrast might not always be available. In this section, I evaluate how differences in MRI contrast between target and atlases affect the synthesis accuracy.

The experiments described here also rely on the dataset of 22 subjects with T1-w, T2-w and CT images used to create the T1/CT database (section 6.1.2) and the T2/CT database (section 6.2.1). In order to assess the effects of using atlases with a different MRI contrast than the target MR image, I synthesised four pseudo CTs for each subject:

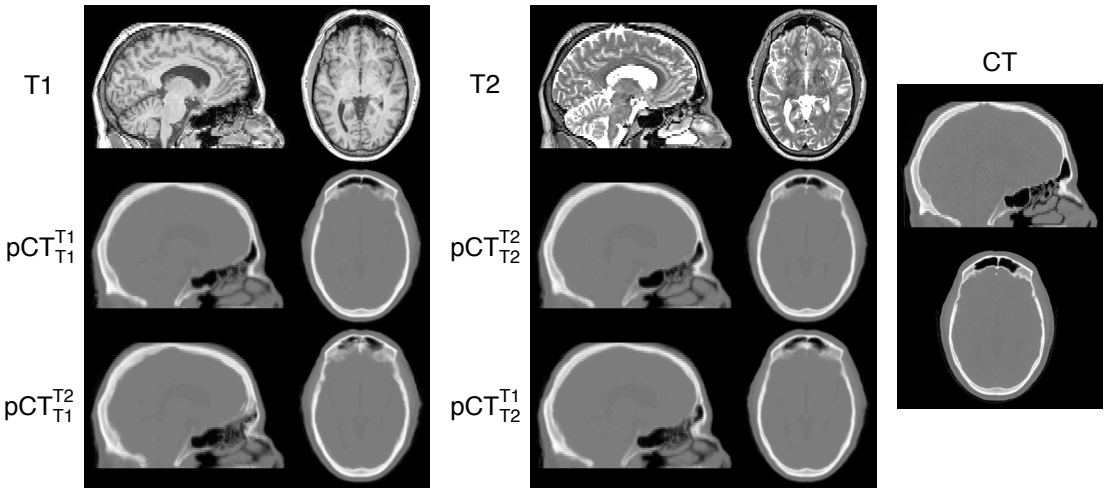

Figure 6.7: Example of pseudo CTs synthesised from a T1-w MR image using the T1/CT database (pCT^{T1}_{T1}) and the T2/CT database (pCT^{T2}_{T1}), and from a T2-w MR image using the T2/CT database (pCT^{T2}_{T2}) and the T1/CT database (pCT^{T1}_{T2}).

- pCT^{T1}_{T1}, obtained from the T1-w MR image using the T1/CT database;
- pCT^{T2}_{T1}, obtained from the T1-w MR image using the T2/CT database;
- pCT^{T2}_{T2}, obtained from the T2-w MR image using the T2/CT database;
- pCT^{T1}_{T2}, obtained from the T2-w MR image using the T1/CT database;

Note that pCT^{T1}_{T1} and pCT^{T2}_{T2} are identical to $npCT_{T1}$ and $npCT_{T2}$, respectively, but were renamed for clarity.

The MAE and ME were computed for each subject between the reference CT and the pseudo CTs. The results averaged across all the subjects are displayed in Table 6.2.

Table 6.2: Average $\pm$ SD of the MAE and ME computed for the full head between the reference CT and the pseudo CTs synthesised from a T1-w MR image using the T1/CT database (pCT^{T1}_{T1}) and the T2/CT database (pCT^{T2}_{T1}), and from a T2-w MR image using the T2/CT database (pCT^{T2}_{T2}) and the T1/CT database (pCT^{T1}_{T2}).

	pCT^{T1}_{T1}	pCT^{T2}_{T1}	pCT^{T2}_{T2}	pCT^{T1}_{T2}
MAE (HU)	91.4 ± 10.5	120.2 ± 15.8	91.1 ± 8.3	100.8 ± 11.3
ME (HU)	3.0 ± 16.2	-0.1 ± 16.2	6.5 ± 17.0	-8.6 ± 16.7

As expected, the synthesis error increases when the targets and atlases do not share the same contrast. We note that this increase is larger when the synthesis is based on the target T1 image (27%) than when it is based on the T2 image (10%). This difference is visible on the pseudo CTs obtained for a representative subject displayed in Figure 6.7. When comparing pCT^{T1}_{T2} with pCT^{T1}_{T1} and pCT^{T2}_{T2}, the skull appears less sharp but its thickness is almost identical. However, for pCT^{T2}_{T1} the skull is thicker and the sinuses not well defined.

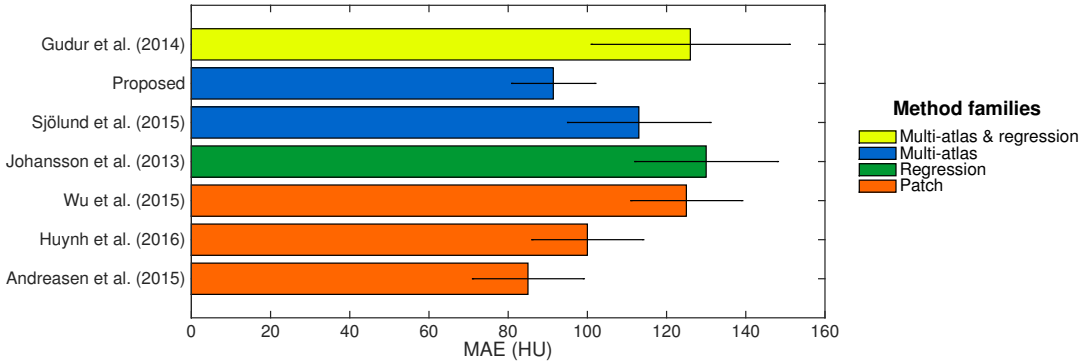

Figure 6.8: Bar plots displaying the averaged MAE obtained with different atlas-based methods. The error bars represent twice the standard deviation. 'Proposed' refers to the results presented in section 6.1.2.2.

6.4 Discussion

In this chapter, I first presented a strategy to improve the CT synthesis accuracy at the borders of the field of view. With the proposed similarity measure extending the convolution-based local normalised correlation coefficient to irregular regions of interest, the FOV mismatches between target and atlas images are taken into account, which enables the absolute synthesis error to drop by 30% (from 122 to 91 HU).

Similar synthesis errors were obtained with other atlas-based methods. Andreasen et al. (2015), Huynh et al. (2016) and Wu et al. (2015) developed patch-based methods and obtained average MAEs of 85 $\pm$ 14 HU (five subjects), 100 $\pm$ 14 HU (16 subjects) and 125 $\pm$ 14 HU (13 subjects), respectively. Using a Gaussian mixture regression, Johansson et al. (2013) obtained an average $\pm$ SD MAE of 130 $\pm$ 18 HU (nine subjects). Sjölund et al. (2015) reported an average MAE of 113 $\pm$ 18 HU obtained for ten subjects using a multi-atlas method where the pseudo CT was created by computing the voxel-wise median of the deformed CTs. Combining multi-atlas and regression methods, Gudur et al. (2014) reported an average MAE of 126 $\pm$ 25 HU (eight subjects). Performances of the different methods are summarised in Figure 6.8.

I also extended the CT synthesis method to other MRI sequences: the T2-w and LAVA-Flex. T2-w images provide slightly different anatomical information than T1-w images as in a T1-w image bone, air and CSF all have low intensities while in a T2-w image the CSF appears bright. Similar synthesis accuracy was obtained when pseudo CTs were generated from a T1-w or a T2-w image. In this study, both the T1-w and T2-w were high-resolution images (1 mm^3). If at least one such image is usually acquired during a PET/MR examination, this is not mandatory. However, sequences dedicated to attenuation correction are always acquired. For this reason, I assessed the ability of the method to synthesise pseudo CTs from low resolution ($2 \times 2 \times 2.6$ mm^3) LAVA-Flex images. I showed that if the synthesis error is higher than when using T1-w or T2-w images, it is possible to obtain accurate pseudo CTs from LAVA-Flex images.

Finally, I showed that while better synthesis results are obtained when the target and atlas MR images share the same contrast, satisfactory pseudo CTs can be obtained from target MR images whose contrast does not match the contrast of the MR atlases in the database.

Chapter 7

CT synthesis: combining multiple MRI contrasts

In the previous chapter, we saw that the multi-atlas CT synthesis method was able to generate pseudo CT images from different MRI sequences such as T1-w, T2-w or LAVA-Flex. As T1-w and T2-w MR images provide complementary information to describe the underlying subject's anatomy and are often routinely acquired in clinical practice, I propose to extend the algorithm to multi-contrast data by combining information from both sequences at the registration and image similarity stages. I also show that the suggested improvements bring the methodology close to its theoretical limits. Some of the methods and results have been published in Burgos et al. (2015a).

7.1 Method

Data

Twenty-two sets of T1-weighted MRI, T2-weighted MRI and CT brain images were used for the validation, as described in the previous chapter (sections 6.1.2 and 6.2.1). Both the T1-w and T2-w are volumetric scans with 1.1 mm^3 isotropic voxels.

7.1.1 Exploiting MRI multiple contrasts

The single contrast algorithm presented in chapters 3 and 6 relies on the ability to accurately map T1-w or T2-w brain images from different subjects, a challenging process in low-contrast areas. As T1-w and T2-w MR images complement one another to describe the subject's morphology, I propose to combine information from both contrasts at the registration and image similarity stages.

To do so, the T2 image is affinely aligned and resampled to the T1 image to form a T1-T2 pair. The inter-subject coordinate mapping between T1-T2 pairs is obtained using a symmetric global registration followed by a cubic B-spline parametrised non-rigid registration, using a multivariate normalised mutual information as implemented in NiftyReg (Modat et al., 2010). All the CTs in the database are then mapped to the target subject using the transformation that maps the subject's corresponding MRI pair in the database to the target MR image. The multivariate ROI-LNCC (MV-ROI-LNCC) used for the local atlas ranking procedure is derived from the ROI-LNCC introduced in the previous chapter (section 6.1.1)

and defined as

$$\text{MV-ROI-LNCC}_n = \text{ROI-LNCC}\left(I^{T1}, J_n^{T1}\right) + \text{ROI-LNCC}\left(I^{T2}, J_n^{T2}\right) \quad . \tag{7.1}$$

7.1.2 Influence of the resolution

In the dataset used in this chapter, the resolution of both the T1 and T2 images is high (1.1 mm isotropic), which might not always be the case in clinical practice. To study the impact of the T2 resolution on the accuracy of the pseudo CT synthesised from a T1-T2 pair, T2 images were downsampled to two thirds (1.65 mm^3) and half (2.2 mm^3) of their resolution. To simulate a 2D acquisition, common in clinical setting, the T2 images were also downsampled in the z direction: $1.1 \times 1.1 \times 5$ mm^3. Once downsampled, the T2 images were affinely aligned to the T1 image and resampled to its discretisation grid to create the new T1-T2 pairs. Pseudo CTs were then synthesised from each pair.

7.1.3 Exploring the theoretical performance plateau

To explore the intrinsic limit of the proposed methodology, a pseudo CT, called theoretical best, is synthesised from the subject's T1-T2 pair as in section 7.1.1, except for the local similarity measure which is computed between the mapped CTs and the subject's original CT. The similarity between the mapped CTs and the real CT should provide the upper limit of performance of the proposed algorithm, as it removes the transitivity assumption between MRI and CT similarity, which states that if two MR images are similar at a certain spatial location, the two CT images will also be similar.

7.2 Validation and results

7.2.1 Algorithmic comparison

The performance of the synthesis algorithm from multi-contrast MR images was compared with reference data for 22 subjects following a leave-one-out cross-validation scheme. For each subject seven pseudo CTs were synthesised:

- pCT_{T1} using the ROI-LNCC on the T1 image;
- pCT_{T2} using the ROI-LNCC on the T2 image;
- $\text{pCT}_{\text{T1,T2}}$ using the MV-ROI-LNCC on the T1-T2 pair of images, T2 at full resolution;
- $\text{pCT}_{\text{T1,T2}^{2/3}}$ using the MV-ROI-LNCC on the T1-T2 pair of images, T2 at two third of its initial resolution;
- $\text{pCT}_{\text{T1,T2}^{1/2}}$ using the MV-ROI-LNCC on the T1-T2 pair of images, T2 at half its initial resolution;
- $\text{pCT}_{\text{T1,T2}^{\text{2D}}}$ using the MV-ROI-LNCC on the T1-T2 pair of images, T2 anisotropic resolution simulating a 2D acquisition;
- pCT_{TB} using the theoretical best approach as described in section 7.1.3.

As in the previous chapter, the mean absolute error (MAE) and the mean error (ME) were calculated for every subject between the reference CT and each of the pseudo CTs in a region defined by segmenting the head from the background using the reference CT. Statistical significance was assessed using the paired, one-tailed, Wilcoxon signed-rank test. Finally, to localise the error and bias introduced

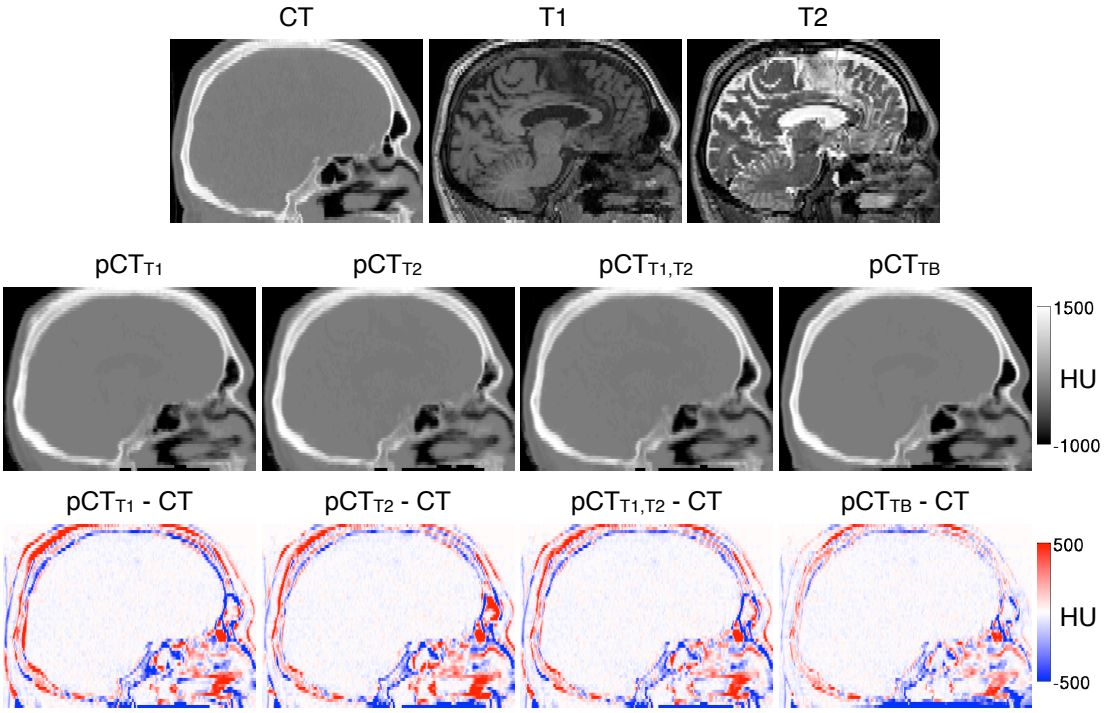

Figure 7.1: Example for a representative subject of the reference CT,T1 and T2 images (top), the different pseudo CTs (middle), and the difference images between the pseudo CTs and the reference CT (bottom).

by some of the approaches, difference maps were computed between the reference CT and the pseudo CTs, previously mapped to a common space (section 6.1.2.1), and averaged across all the subjects.

7.2.2 Results

An example of original CT and pseudo CTs is displayed in Figure 7.1. The average and standard deviation (SD) of the MAEs and MEs computed in the full head are presented in Table 7.1. The significance tests between the different methods are summarised in Figure 7.2.

We first note that synthesising CT images from multiple contrasts (pCT$_{T1,T2}$) significantly reduces the MAE ($p < 10^{-4}$) when compared with single contrast synthesis (pCT$_{T1}$ and pCT$_{T2}$). However, the improvement obtained by exploiting multiple contrasts depends on the initial resolution of the images. When the resolution of the T2 image is lower than the resolution of the T1 image, meaning that its contribution to the synthesis process is limited, the MAE obtained is between the error obtained when using two high-resolution images and the error obtained when using only one contrast. The resolution of the second image forming the pair, here the T2, needs to be at least 2/3 of the resolution of the main image, the T1, to reach a significant improvement ($p < 10^{-4}$). The MAE obtained with the theoretical best is 25% lower than the error obtained with the multi-contrast approach (pCT$_{T1,T2}$).

The difference maps computed between the original CT and the pseudo CTs, and averaged across all the subjects, are presented in Figure 7.3. We note that combining multiple contrasts tends to reduce the bias. Regardless of the method applied, the largest errors are now mostly located in the sinus area and at the bone/dura/CSF boundary.

Table 7.1: Average ± SD of the MAE and ME computed for the full head between the original CT and the pseudo CTs synthesised from a T1-w (pCT_{T1}), a T2-w (pCT_{T2}) or combinations of T1-w and T2-w ($pCT_{T1,T2^{2D}}$, $pCT_{T1,T2^{1/2}}$, $pCT_{T1,T2^{2/3}}$, $pCT_{T1,T2}$) MR images, and the theoretical best (pCT_{TB}).

		pCT_{T1}	pCT_{T2}	$pCT_{T1,T2^{2D}}$	$pCT_{T1,T2^{1/2}}$	$pCT_{T1,T2^{2/3}}$	$pCT_{T1,T2}$	pCT_{TB}
MAE	Average	91.4	91.1	92.2	91.2	87.4	85.4	66.2
	SD	10.5	8.3	8.1	7.7	7.8	7.7	6.5
ME	Average	3.0	6.5	3.7	5.4	7.1	3.5	0.4
	SD	16.2	17.0	16.0	16.1	15.8	15.3	15.5

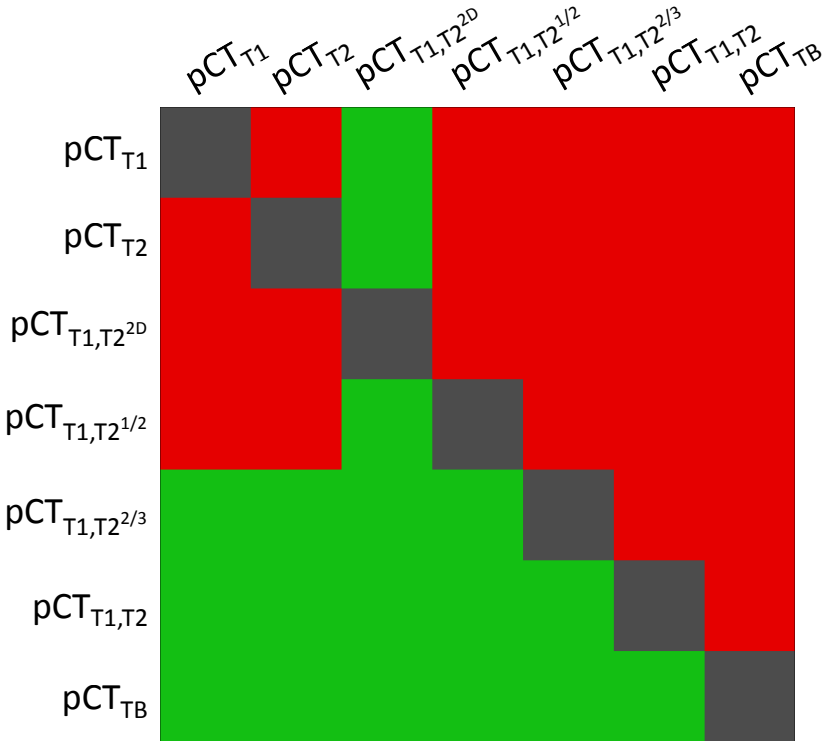

Figure 7.2: Results of the one-tailed Wilcoxon signed-rank test at the 5% significance level for the MAE computed between the reference CT and each of the pseudo CTs. The colour green indicates a significant decrease in MAE for the row method when compared to the column method, while the red indicates that the difference in MAE is not significant.

7.3 Discussion

In this chapter, I extended the method developed in chapters 3 and 6 to multi-contrast MRI data, allowing the introduction of complementary information. I showed that one can synthesise CT from T1 images, T2 images, but also combinations of MRI contrasts. Combining complementary information describing the underlying subject's anatomy, at both the registration and image similarity stages, reduces the ill-posedness of the problem. As a consequence, the CT synthesis error decreases. When analysing the results of the CT synthesis, we note that the errors are mostly located in the sinus area and at the bone/dura/CSF boundaries (Figure 7.3), regions with a low tissue discriminative power. I also showed that combining multiple contrasts brings the proposed methodology close to its theoretical limits.

In clinical practice, two high-resolution volumetric images might not always be available. We saw

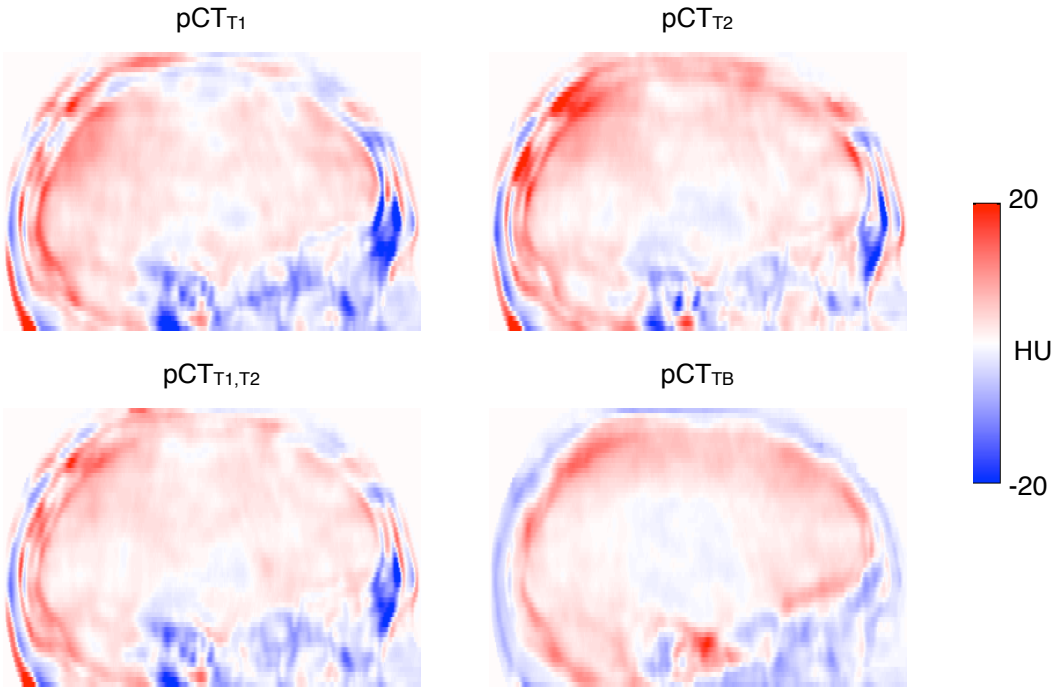

Figure 7.3: Mean intensity projection of the difference, averaged over 22 subjects, between the reference CT and the pseudo CTs synthesised from a T1-w (pCT$_{T1}$), a T2-w (pCT$_{T2}$) or a combination of T1-w and T2-w pCT$_{T1,T2}$) MR images, and the theoretical best (pCT$_{TB}$).

that if the resolution of the T2 image is lower than the resolution of the T1 image, its contribution to the synthesis process is limited but still improves the synthesis accuracy. The quality of the results obtained is between the quality reached when using two high-resolution images and the quality reached when only using one contrast.

The proposed method not only gives more accurate and robust results but also opens up new possibilities of improvement through the exploitation of multi-contrast data. The ability to use different combinations of MRI contrasts brings flexibility to the proposed methodology, which is essential in a clinical context.

Chapter 8

Attenuation map validation on FDG and Florbetapir PET images

In this chapter, I validate, using two different PET tracers, the CT synthesis algorithm based on the multi-contrast multi-atlas information propagation scheme presented in chapters 6 and 7. The method was validated with 22 subjects with various dementia syndromes, who had MR imaging and two PET/CT scans with different tracers: ^{18}F-FDG and ^{18}F-florbetapir (Aβ), on consecutive days. The PET reconstruction accuracy was assessed, for both tracers, by comparing the reference PET images, corrected for attenuation using the CT-based μ-map, to the PET images corrected using the proposed method. I analysed results across the full brain but also in regions of particular interest, e.g. when studying dementia. These results have been published in Burgos et al. (2015a).

8.1 Method

8.1.1 Data

Twenty-two sets of ^{18}F-FDG PET, ^{18}F-florbetapir PET, CT and MR brain images were used in order to validate our attenuation correction method. The cohort was composed of five individuals with posterior cortical atrophy, five with semantic dementia, four with progressive nonfluent aphasia, three with logopenic progressive aphasia and five healthy controls. Nine individuals were amyloid positive and 13 amyloid negative. Each individual attended for three imaging sessions on three consecutive days. At the first visit, MR imaging was acquired on a 3T Siemens Magnetom Trio scanner (Siemens Healthcare, Erlangen, Germany) and includes a T1-weighted (3.0 T; TE/TR/TI, 2.9 ms/2200 ms/900 ms; flip angle 10°; voxel size 1.1 $\times$ 1.1 $\times$ 1.1 mm^3) and a T2-weighted (3.0 T; TE/TR, 401 ms/3200 ms; flip angle 120°; voxel size 1.1 $\times$ 1.1 $\times$ 1.1 mm^3) volumetric scans. For the second and third visits, imaging was performed on a GE Discovery ST PET/CT scanner (GE Healthcare systems, Waukesha, WI), providing CT (voxel size 0.59 $\times$ 0.59 $\times$ 2.5 mm^3, 120 kVp, 300 mA) and PET (voxel size 1.95 $\times$ 1.95 $\times$ 3.27 mm^3) images. For visit two, images were acquired for 10 minutes, 50 minutes after injection of $\sim$200 MBq ^{18}F-florbetapir; for visit three, images were acquired for 20 minutes, 30 minutes after injection of $\sim$185 MBq ^{18}F-FDG. The local ethics committee approved the study and all subjects gave written, informed consent.

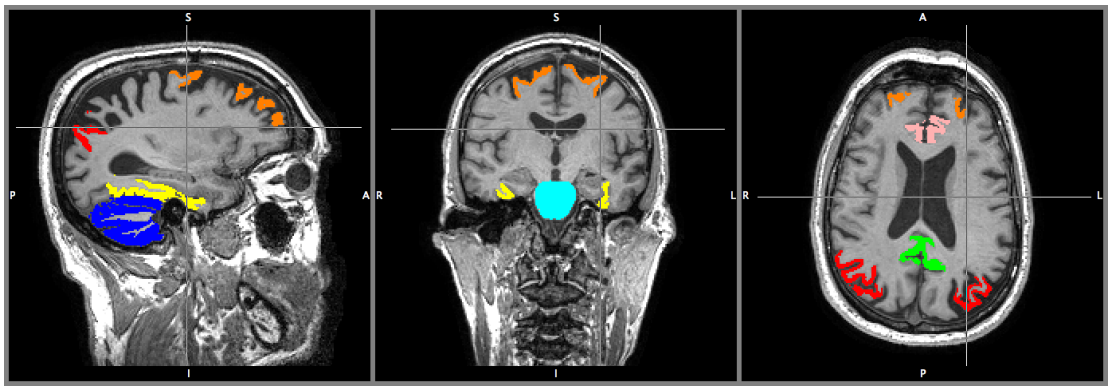

Figure 8.1: Regions used for the PET intensity normalisation and analysis. The pons (light blue), cerebellar grey matter (blue), angular gyrus (red), superior frontal gyrus (orange), fusiform gyrus (yellow), posterior cingulate gyrus (green) and anterior cingulate gyrus (pink) are superimposed on a T1-w MR image.

Because of the separate PET and MRI acquisitions, sequences used for MR-based attenuation correction, such as Dixon or UTE sequences, were not acquired and thus were not available for comparison.

8.1.2 Validation on FDG and Florbetapir images

The aim of this chapter is to validate following a leave-one-out strategy the MR-based attenuation correction method described in chapters 6 and 7 for two different PET tracers. To do so, pseudo CT (pCT) images, synthesised from MR images, were used during the reconstruction of PET images to correct for attenuation.

A common practice in the neuroimaging community is to normalise PET images using a reference region (Minoshima et al., 1995; Wong et al., 2010). For the FDG PETs, the mean uptake value in the pons (Minoshima et al., 1995) was used to normalise the PET images of each subject, thus allowing for a comparable range of values. For the florbetapir PETs, the mean value in the cerebellar grey matter (Wong et al., 2010) was used. These reference regions were extracted from parcellated T1-weighted MR images. The parcellations were obtained from a multi-label propagation and fusion algorithm, as implemented in NiftySeg and described in (Cardoso et al., 2015). All subjects forming the database were controls with associated structural parcellation of 143 key structures as provided by Neuromorphometrics for the MICCAI 2012 Grand Challenge on label fusion[1]. The inter-subject coordinate mapping was obtained using a symmetric global registration followed by a cubic B-spline parametrised non-rigid registration using local normalised cross-correlation as a measure of similarity and a final grid spacing of $5 \times 5 \times 5$ voxels, as implemented in NiftyReg (Modat et al., 2010).

Once the PET images were normalised, the analysis consisted in providing quantitative regional assessment of the mean absolute error and the mean voxel bias between the PET images corrected with the method proposed and the PET images corrected with the reference CT images. The full brain region, posterior cingulate gyrus, angular gyrus, superior frontal gyrus, fusiform gyrus and anterior cingulate gyrus, regions relevant to dementia pathologies, were obtained from the parcellated T1-weighted MR images (Figure 8.1).

[1] https://masi.vuse.vanderbilt.edu/workshop2012/index.php/Challenge_Details

8.1.3 PET reconstruction

I used the PET images provided by the PET/CT scanner as input for a simulation technique. To evaluate the effect of different μmaps on the PET images, I followed a projection/reconstruction technique described in chapter 3. The original PET image and the reference CT μmap were projected to obtain simulated sinograms. The scatter sinogram was estimated using a Single Scatter Simulation algorithm (Watson, 2000). Projection data were rescaled to account for attenuation and the estimated scatter sinogram was added to produce a non-corrected sinogram, similar to the data acquired by the PET/CT scanner. The non-corrected PET sinogram was then reconstructed with both scatter estimation and attenuation correction based on the reference CT or pseudo CT μmaps. The PET image reconstructed using the reference CT μmap was considered as the reference PET. An ordered subsets expectation maximisation (OSEM) algorithm with three iterations of 21 subsets was used. Effects of PSF and random coincidences were not included and post-reconstruction smoothing was not applied. The simulation and reconstruction were performed using STIR (Thielemans et al., 2012).

8.1.4 Algorithmic comparison

The performance of the proposed synthesis algorithm was compared with reference data for 22 subjects following a leave-one-out cross-validation scheme. For each subject, and both PET tracers, three pseudo CTs were synthesised using a database of 21 subjects as described in chapters 6 and 7:

- pCT_{T1} using the ROI-LNCC on the T1 image (section 6.1);
- pCT_{T2} using the ROI-LNCC on the T2 image (section 6.2.1);
- $\text{pCT}_{\text{T1,T2}}$ using the MV-ROI-LNCC on the T1-T2 pair of images (section 7.1.1).

In order to preserve the alignment of the CT and PET images, the two PET/CT acquisitions were considered independently, meaning that I created two MR-CT databases: one with the CT images from the ^{18}F-FDG PET/CT scan and the MR images; and another one with the CT images from the ^{18}F-florbetapir PET/CT scan and the MR images.

For both the FDG and florbetapir tracers, the simulated PET data were reconstructed using the different pCT μmaps, and compared with the reference PET reconstructed using the CT-based μmap, validating the accuracy of the PET attenuation correction.

I first computed the relative MAEs and ME, defined respectively as

$$\text{rMAE} = 100 * \frac{|\text{PET}_{\text{pCT}} - \text{PET}_{\text{CT}}|}{\text{PET}_{\text{CT}}} \qquad \text{and} \qquad \text{rME} = 100 * \frac{\text{PET}_{\text{pCT}} - \text{PET}_{\text{CT}}}{\text{PET}_{\text{CT}}} \quad ,$$

between the reference PET (PET_{CT}), corrected for attenuation with the CT-based μmap, and each of the PETs corrected with the synthetic μmaps (PET_{pCT}), in the reference regions. This analysis aims at characterising the presence of error and bias in the reference regions.

In order to provide a quantitative regional assessment of the error and bias after normalisation by the reference region, for both the FDG and florbetapir tracers, I computed the relative MAEs and MEs between the normalised reference PET and each of the normalised PETs corrected with the synthetic μmaps. In order to assess the performance of the proposed method in areas relevant to dementia pathologies, I analysed results in the full brain region, but also in the posterior cingulate gyrus, angular

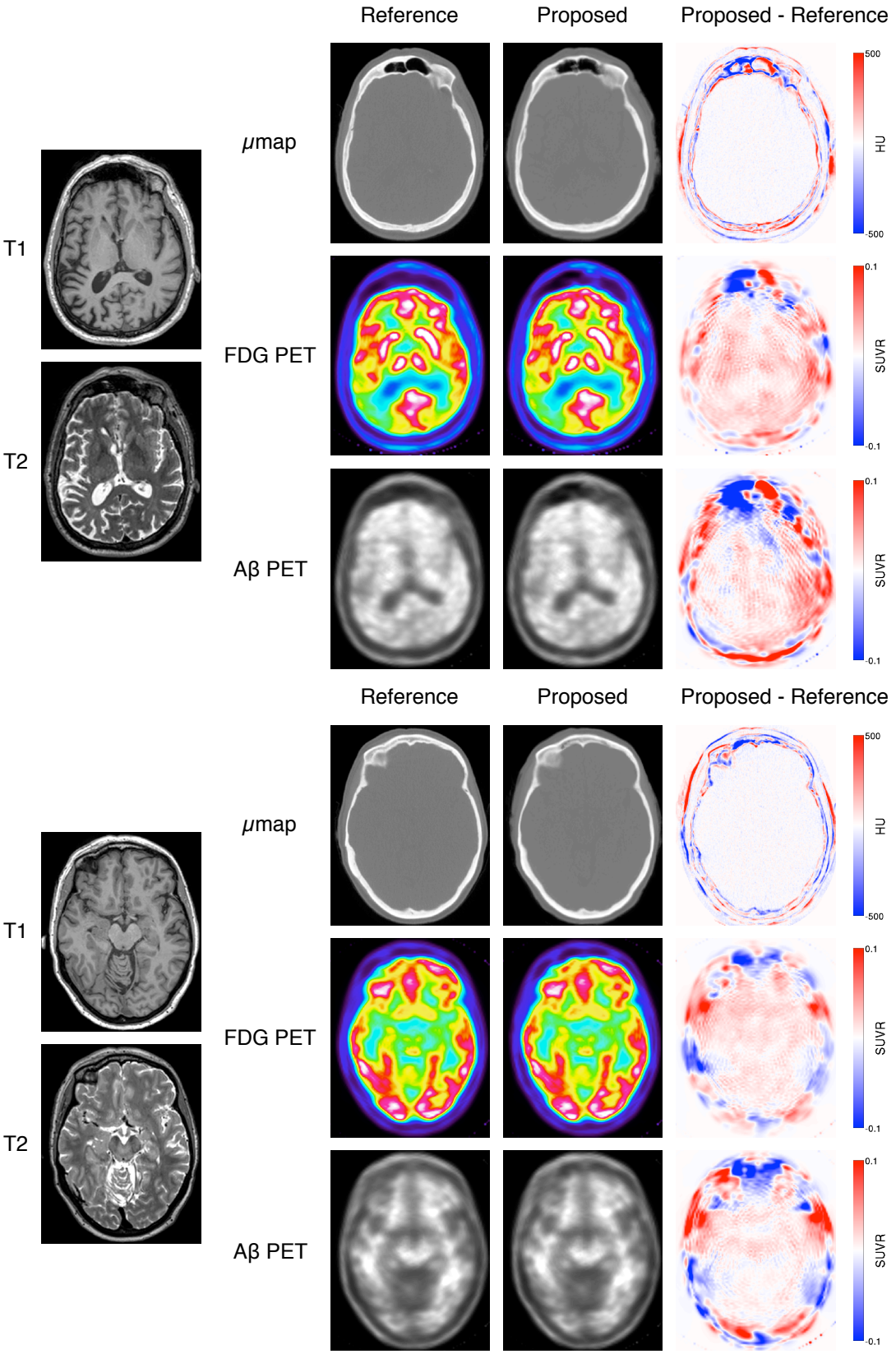

Figure 8.2: Example of CT (top row), ^{18}F-FDG PET (middle row) and ^{18}F-florbetapir (Aβ) PET (bottom row) images obtained from the reference and pseudo CTs, and difference images, for an amyloid positive (top) and an amyloid negative (bottom) subject.

gyrus, superior frontal gyrus, fusiform gyrus and anterior cingulate gyrus, which were propagated from the parcellated T1 image to the PET images (Cardoso et al., 2015). Statistical significance was assessed using the paired, one-tailed, Wilcoxon signed-rank test.

Finally, the PET images from the 22 subjects were mapped to a common space via a CT-based groupwise registration (Rohlfing et al., 2001; Modat et al., 2014). Difference maps were then computed between the reference PET and each of the PETs corrected with the pCT μmaps, and their average and standard deviation, across all the subjects, displayed using a mean intensity projection.

8.2 Results

Examples of PET images reconstructed with the CT-based and synthetic μmaps are presented in Figure 8.2. The average and SD of the rMAEs and rMEs are presented in Table 8.1. Results are also displayed with box plots in Figure 8.3 for the reference regions, Figure 8.4 for the brain region, and Figure 8.5 for the other ROIs.

Results in Table 8.1 and Figure 8.3 show that the errors in the reference regions are lower for the FDG PET than for the florbetapir PET. This can be explained by the fact that the regions surrounding the pons are better synthesised than those around the cerebellum, which is closer to the border of the FOV. In both cases the median error is less than 2%.

In all the regions analysed, combining multiple MRI contrasts reduces the rMAE when compared to single image synthesis (Table 8.1, Figures 8.4 & 8.5). In ROIs close to the skull (superior frontal gyrus, angular gyrus and fusiform gyrus), the mean rMAE does not exceed 2.8%, while in deeper structures (posterior cingulate gyrus and anterior cingulate gyrus) the mean rMAE is below 1.2%. A summary of the significance tests between the different methods is presented in Figure 8.6. For most ROIs, especially the ones near the skull, the multi-contrast approach significantly improves the synthesis accuracy.

In order to analyse the presence of bias in the PET images, I computed the rME between the reference PETs and the PETs corrected with the synthetic μmaps. In the full brain region, the rME results

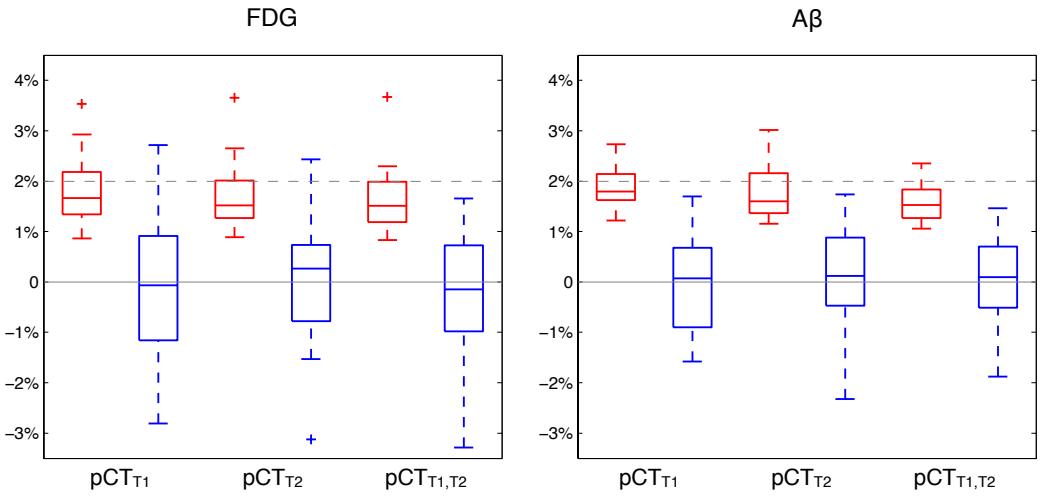

Figure 8.3: Boxplots displaying the median, lower and upper quartiles, minimum, maximum and outliers of the rMAE (red) and rME (blue) calculated between the reference PETs and the PETs corrected with the synthetic μmaps, in the reference regions.

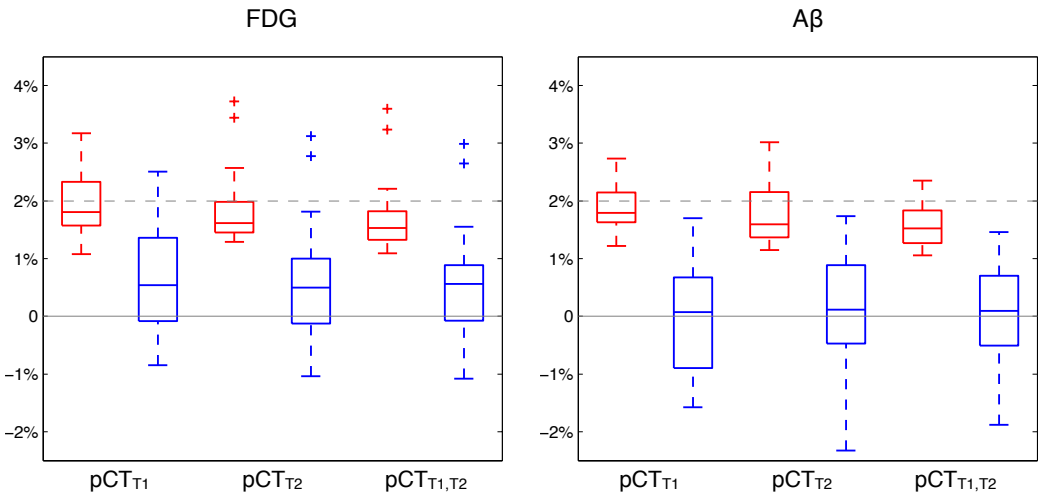

Figure 8.4: Boxplots displaying the median, lower and upper quartiles, minimum, maximum and outliers of the rMAE (red) and rME (blue) calculated between the reference PETs and the PETs corrected with the synthetic μmaps, in the brain region.

indicate a low bias: the rME is on average below 0.6% for the FDG tracer, and below 0.1% for the florbetapir tracer, with a standard deviation of 1% for both tracers. With the multi-contrast synthesis, the region presenting the greatest bias for the FDG tracer is the angular gyrus with an rME of 0.98 $\pm$ 2.17%. For the florbetapir tracer, the superior frontal gyrus presents the greatest bias, with an rME of -0.28 $\pm$ 1.34%.

Two outliers are visible on Figures 8.4 & 8.5. These are due to an unusual low bone density for one subject and to full frontal sinuses for the other.

The average and SD across all the subjects of the difference maps computed between the normalised reference PETs and PETs$_{pCT}$ are presented in Figure 8.7. None of the results present a systematic bias.

8.3 Discussion

Correcting for attenuation is an essential requirement to perform an accurate quantitative analysis of PET data. In this chapter, I jointly validated the proposed MR-based attenuation correction method on two different tracers using 22 subjects with dementia. Each subject underwent two PET/CT scans, with ^{18}F-FDG and ^{18}F-florbetapir tracers, providing reference CT and PET images, and an MRI scan providing T1-weighted and T2-weighted images. The evaluation was conducted both in the full brain and in ROIs relevant for dementia (posterior cingulate gyrus, angular gyrus, superior frontal gyrus, fusiform gyrus and anterior cingulate gyrus).

I extended the method from chapter 3 to multi-contrast MRI data, allowing the introduction of complementary information. Combining complementary information describing the underlying subject's anatomy, at both the registration and image similarity stages, reduces the ill-posedness of the problem. As a consequence, the CT synthesis error decreases, which leads to reduced errors when comparing PET images to the reference PETs.

I demonstrated that, for both tracers, in the brain region, the absolute error when comparing PET images corrected with the pseudo CTs to the reference PET images corrected using the original CT is

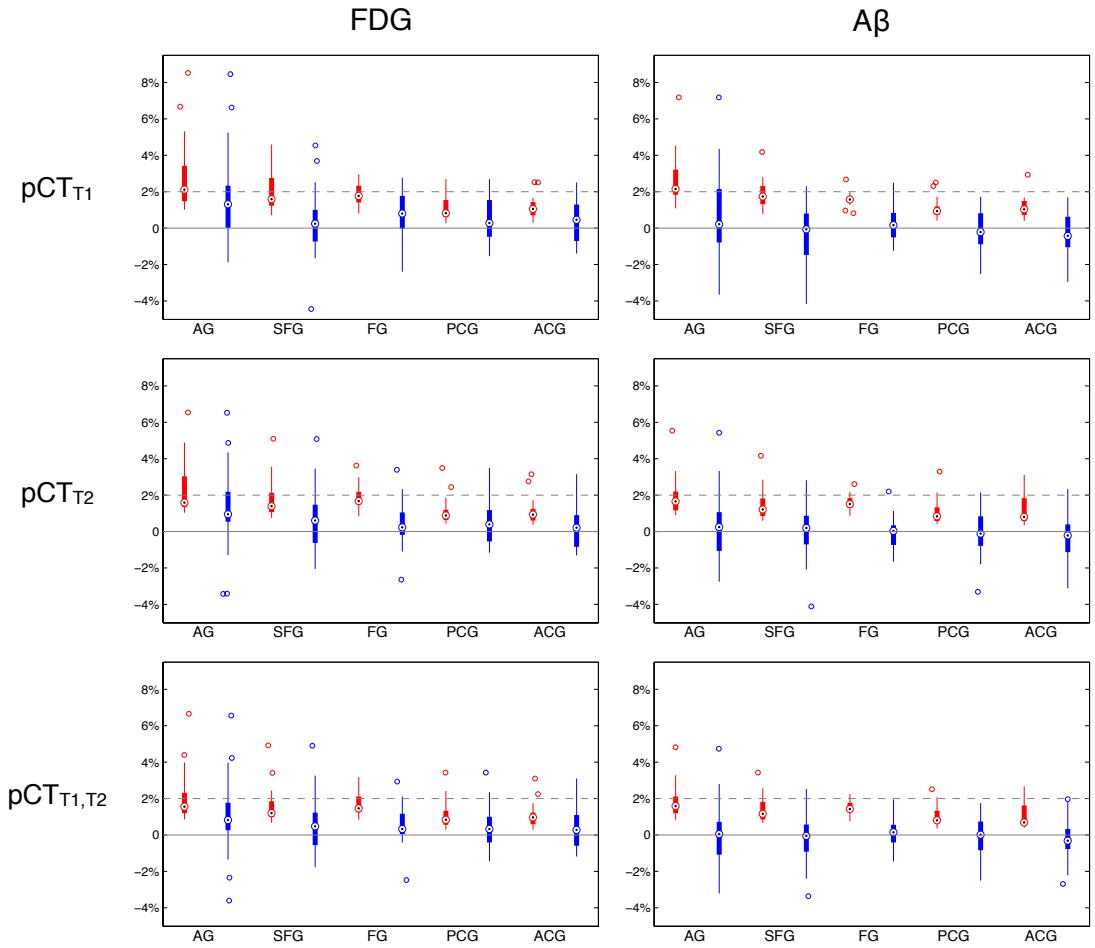

Figure 8.5: Boxplots displaying the median, lower and upper quartiles, minimum, maximum and outliers of the rMAE (red) and rME (blue) calculated between the reference PETs and the PETs corrected with the synthetic μmaps, in different ROIs: angular gyrus (AG), superior frontal gyrus (SFG), fusiform gyrus (FG), posterior cingulate gyrus (PCG) and anterior cingulate gyrus (ACG).

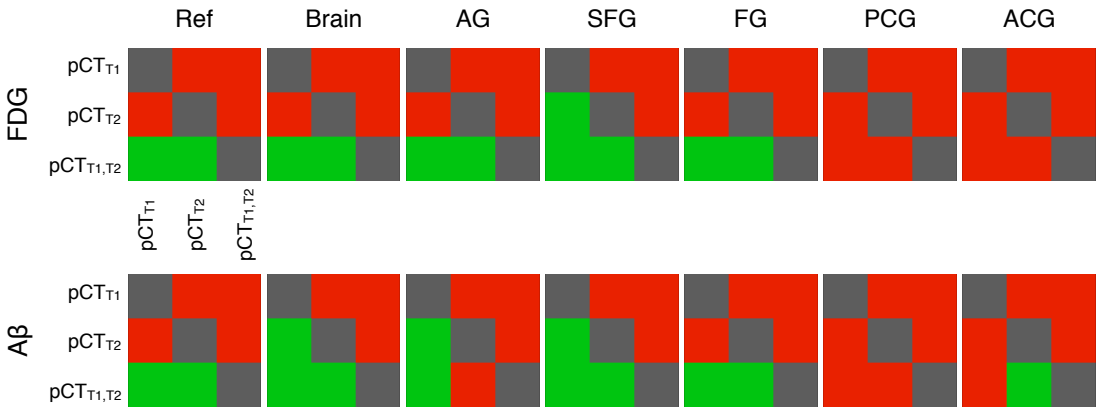

Figure 8.6: Results of the one-tailed Wilcoxon signed-rank test at the 5% significance level for the rMAE computed between the reference PET and each of the PETs corrected with the pCT μmaps in the reference regions, the full brain and five ROIs. The colour green indicates a significant decrease in rMAE for the row method when compared to the column method, while the red indicates that the difference in rMAE is not significant. Note that, for most ROIs, pCT$_{T1,T2}$ is significantly better.

Table 8.1: Average ± SD of the relative MAE and ME between the ^{18}F-FDG and ^{18}F-florbetapir PETs corrected with the CT-based μmaps and the PETs corrected with the synthetic μmaps in 7 ROIs: the reference region used for normalisation, the brain region, angular gyrus (AG), superior frontal gyrus (SFG), fusiform gyrus (FG), posterior cingulate gyrus (PCG) and anterior cingulate gyrus (ACG).

			pCT_{T1}	pCT_{T2}	$pCT_{T1,T2}$
FDG	Ref	rMAE (%)	1.79 ± 0.64	1.72 ± 0.62	1.64 ± 0.60
		rME (%)	-0.12 ± 1.37	0.09 ± 1.23	-0.15 ± 1.21
	Brain	rMAE (%)	1.96 ± 0.56	1.85 ± 0.64	1.71 ± 0.62
		rME (%)	0.58 ± 0.97	0.54 ± 1.08	0.56 ± 0.98
	AG	rMAE (%)	2.79 ± 1.91	2.32 ± 1.45	2.10 ± 1.41
		rME (%)	1.58 ± 2.69	1.17 ± 2.33	0.98 ± 2.17
	SFG	rMAE (%)	2.01 ± 1.17	1.66 ± 1.02	1.53 ± 1.01
		rME (%)	0.38 ± 1.95	0.69 ± 1.65	0.57 ± 1.58
	FG	rMAE (%)	1.83 ± 0.56	1.84 ± 0.63	1.68 ± 0.57
		rME (%)	0.71 ± 1.17	0.38 ± 1.27	0.55 ± 1.12
	PCG	rMAE (%)	1.11 ± 0.73	1.10 ± 0.74	1.06 ± 0.74
		rME (%)	0.50 ± 1.19	0.41 ± 1.24	0.44 ± 1.20
	ACG	rMAE (%)	1.14 ± 0.60	1.09 ± 0.69	1.05 ± 0.66
		rME (%)	0.36 ± 1.18	0.27 ± 1.21	0.39 ± 1.14
Florbetapir	Ref	rMAE (%)	2.02 ± 0.59	2.11 ± 0.74	1.93 ± 0.62
		rME (%)	0.42 ± 1.21	0.50 ± 1.36	0.39 ± 1.20
	Brain	rMAE (%)	1.87 ± 0.39	1.74 ± 0.48	1.60 ± 0.41
		rME (%)	0.04 ± 0.92	0.02 ± 0.99	-0.02 ± 0.87
	AG	rMAE (%)	2.67 ± 1.43	1.90 ± 1.05	1.82 ± 0.94
		rME (%)	0.68 ± 2.53	0.27 ± 1.91	0.06 ± 1.77
	SFG	rMAE (%)	1.86 ± 0.78	1.50 ± 0.85	1.38 ± 0.72
		rME (%)	-0.33 ± 1.66	-0.07 ± 1.54	-0.28 ± 1.34
	FG	rMAE (%)	1.57 ± 0.36	1.58 ± 0.41	1.49 ± 0.36
		rME (%)	0.25 ± 0.92	-0.02 ± 0.89	0.11 ± 0.85
	PCG	rMAE (%)	1.07 ± 0.53	1.09 ± 0.69	1.05 ± 0.59
		rME (%)	-0.11 ± 1.16	-0.15 ± 1.24	-0.17 ± 1.16
	ACG	rMAE (%)	1.11 ± 0.58	1.20 ± 0.82	1.04 ± 0.68
		rME (%)	-0.27 ± 1.16	-0.26 ± 1.37	-0.22 ± 1.17

on average less than 2% with less than 1% bias (Table 8.1). While in ROIs close to the skull (superior frontal gyrus, angular gyrus and fusiform gyrus), the mean MAE can be up to 2.8%, in deeper structures (posterior cingulate gyrus, and anterior cingulate gyrus), the mean MAE is below 1.2%. The variance in SUVR explained by the attenuation correction error is likely to be smaller than the intrinsic PET noise variance (Pajevic et al., 1998).

Similar results were obtained with segmentation methods based on UTE images able to generate patient-specific continuous linear attenuation coefficients in the bone region. Juttukonda et al. (2015) reported an average MAE in the brain of 2.55% ± 0.86% (PET tracer: florbetapir, 92 subjects) and Ladefoged et al. (2015) an average MAE of 3.4% ± 1.6% and an average ME of -0.1% ± 2.8% (PET tracer: FDG, 154 subjects). Using atlas-based methods, Navalpakkam et al. (2013) obtained an average MAE of 2.40% ± 3.69% (PET tracer: FDG, five subjects), Izquierdo-Garcia et al. (2014) reported an average MAE of 3.87% ± 5.0% and an average ME of -1.18% ± 6.21% (PET tracers: FDG and FET, 16 subjects), and Chen et al. (2015) reported an average MAE of 2.42% ± 1.0% (PET tracer: Aβ, 20

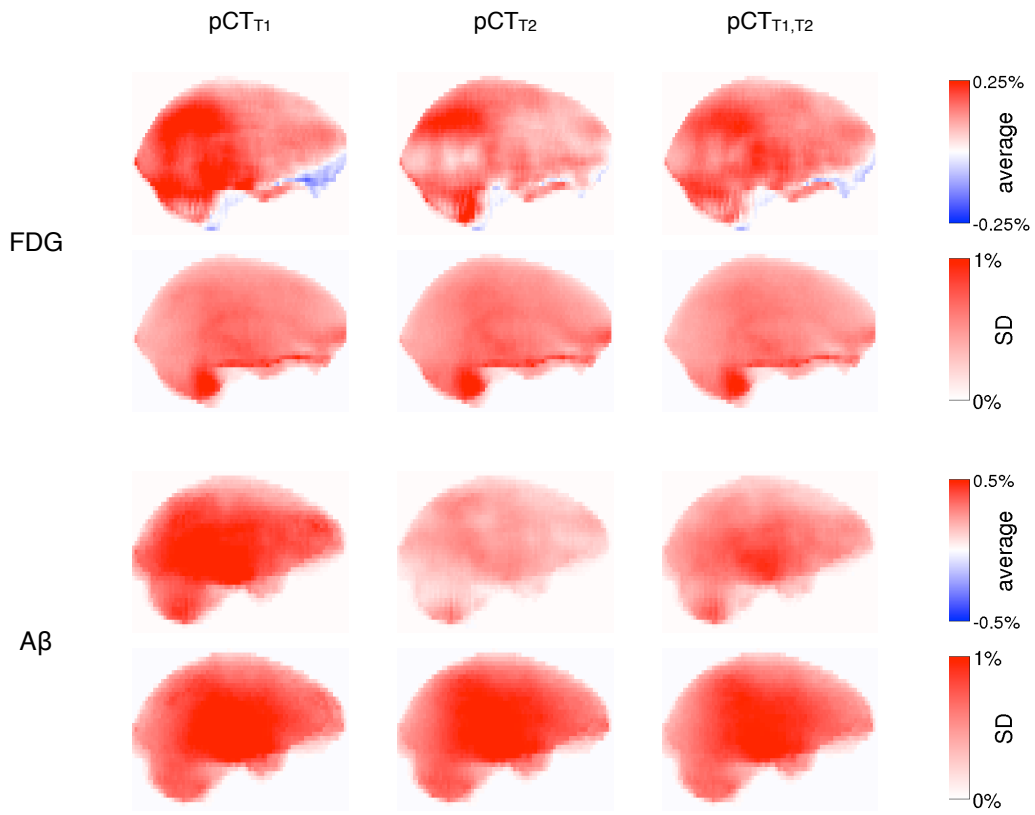

Figure 8.7: Mean intensity projection of the average and SD over 22 subjects of the difference maps. The difference maps were computed between the normalised ^{18}F-FDG (top) and ^{18}F-florbetapir (bottom) reference PETs and the PETs corrected with the synthetic μmaps.

subjects). Performances of the different methods are summarised in Figure 8.8.

To the best of my knowledge, this is the first time that an MR-based attenuation correction method has been jointly validated with two different PET tracers. The validation showed that, for both tracers, the PET images were accurately corrected for attenuation.

The proposed method does not require the acquisition of PET analysis specific MRI sequences, such as Dixon or UTE, which means that the acquisition protocol can be entirely dedicated to clinically-relevant sequences. In this chapter, I used T1 and T2 images as these sequences are usually acquired as part of many standard acquisition protocols, but the method could be extended to any combination of sequences providing enough structural information and structural contrast.

The scope of applications of the proposed methodology exceeds the field of PET/MR. For example, μmap synthesis methods can also be used to correct PET images for attenuation when the radiation dose needs to be kept to a minimum, such as for paediatric subjects. Using an appropriate database, a pseudo CT could be synthesised from an MR image acquired during a previous examination, then registered to the non corrected PET image and finally used to correct the PET data.

While this work was focused on brain applications using subjects who do not present unusual or highly abnormal skull anatomies, further experiments are required to validate the method on subjects with pathologies affecting regions critical for attenuation correction, such as the skull, and in other regions of the body. As long as the morphological variability is represented in the database and the

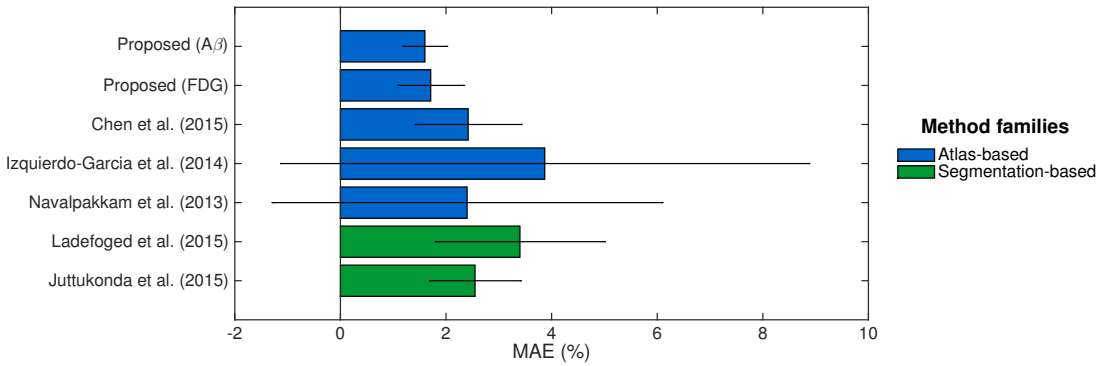

Figure 8.8: Bar plots displaying the averaged MAE obtained in the brain with different MR-based attenuation correction methods. The error bars represent twice the standard deviation. 'Proposed' refers to the results obtained by combining multiple MRI contrasts (T1-w and T2-w).

registration between MRI pairs is sufficiently accurate, the technique could, in theory, be applied to other body parts.

8.4 Conclusion

This chapter presents a validation on ^{18}F-FDG and ^{18}F-florbetapir PET tracers of the CT and attenuation map synthesis method detailed in chapters 6 and 7. The difference between the PET images corrected for attenuation with the CT-based μmaps and the PET images corrected using the synthetic μmaps is, on average, less than 2% for both tracers. The proposed method can be beneficial for clinical practice as it does not require the acquisition of task-specific MRI sequences.

Chapter 9

Subject-specific models for the analysis of pathological FDG PET data

In current clinical practice, fluorodeoxyglucose positron emission tomography (FDG PET) is commonly used to diagnose dementias. FDG uptake reflects glucose consumption, which is reduced by synaptic dysfunction and neuronal degeneration (Herholz, 2003). Different neurodegenerative diseases affect different areas of the brain, and localising abnormalities is essential for differential diagnosis (Nestor et al., 2003; Rabinovici et al., 2008; Crutch et al., 2012).

Cerebral glucose metabolism as measured by FDG PET can be semi-quantitatively evaluated either regionally or on a voxel-by-voxel basis. In regional analysis, the regional standardised uptake value ratio, defined as the average uptake in a region of interest (ROI) relative to a reference region (commonly the pons or cerebellar grey matter), is compared with the regional standardized uptake value (SUVR) expected in a normal control population. This analysis usually requires prior knowledge regarding the selection of relevant discriminant regions, limiting its use (Signorini et al., 1999). In voxel-wise analysis, a subject's PET image is usually aligned to a standardised group space to compare the metabolic activity of the spatially normalised scan on a voxel-by-voxel basis to a distribution obtained from normal control scans, e.g. to produce a Z-score (Drzezga et al., 2005). Exploratory in nature, voxel-wise techniques require less prior information than regional SUVR analysis, but their sensitivity is limited by inter-subject variability in non-pathological tracer uptake, making pathological effects harder to detect (Signorini et al., 1999). Furthermore, there is theoretical uncertainty regarding how to appropriately resample PET data to the group space, how to match the PET point spread function with the group-wise model under linear and non-linear transformations, and how to map the PET data to the group space in a biologically plausible manner.

In this chapter, I combine the advantages of both regional and voxel-wise approaches by analysing PET data in the original subject space (as in regional SUVR approaches) while still providing voxel-by-voxel statistics (as in group-wise approaches). This is achieved through a subject-specific PET model based on the propagation of morphologically-matched PET scans.

These methods and results have been published in Burgos et al. (2015b).

9.1 Method

In the following, four approaches analysing FDG PET images are explored: a regional analysis based on SUVR (section 9.1.3), a voxel-wise analysis in a group space (section 9.1.4), a voxel-wise analysis in the subject's space (section 9.1.5) and the proposed subject-specific analysis (section 9.1.6).

9.1.1 Data

Twenty-two sets of ^{18}F-FDG PET and T1-weighted MR brain images were used to evaluate the proposed methodology, here denoted validation dataset. This dataset was previously used in chapter 8. Of these subjects, five were diagnosed with posterior cortical atrophy (PCA), five with semantic dementia (SD), four with progressive non-fluent aphasia (PNFA), three with logopenic progressive aphasia (LPA) and five were healthy controls. The T1-weighted magnetisation-prepared rapid gradient-echo (3.0 T; TE/TR/TI, 2.9 ms/2200 ms/900 ms; voxel size 1.1 $\times$ 1.1 $\times$ 1.1 mm^3) scans were acquired on a 3T Siemens Magnetom Trio scanner (Siemens Healthcare, Erlangen, Germany). PET images (voxel size 1.95 $\times$ 1.95 $\times$ 3.27 mm^3) were acquired on a GE Discovery ST PET/CT scanner (GE Healthcare systems, Waukesha, WI) for 20 minutes, 30 minutes after injection of 185 MBq ^{18}F-FDG. The local ethics committee approved the study and all subjects gave written, informed consent.

To create fully independent healthy population statistics and to demonstrate the applicability of the proposed patient-specific modelling strategy to multi-site data, a dataset of 29 healthy controls with T1-weighted MR and ^{18}F-FDG PET images were selected from the ADNI2 database[1]. From here on, this dataset is referred to as the control dataset.

9.1.2 Data preprocessing

T1 images from the validation dataset were corrected for intensity non-uniformity following a nonparametric intensity non-uniformity normalisation method (Sled et al., 1998). The T1 images from both the validation and control datasets were then parcellated into 143 different regions using a multi-atlas propagation and fusion algorithm implemented in NiftySeg (Cardoso et al. (2015), see also section 8.1.2). PET images were intensity normalised using the mean uptake of the pons (Minoshima et al., 1995).

9.1.3 Regional analysis

Regional analysis consisted of computing the average standardised uptake in a region of interest to produce a regional SUVR (rSUVR) for each subject independently. This value is then compared with those obtained for normal controls (NC) by its expression as a Z-score, i.e.

$$Z_{\text{rSUVR}} = \frac{\text{rSUVR} - \mu^{\text{NC}}_{\text{rSUVR}}}{\sigma^{\text{NC}}_{\text{rSUVR}}} \ , \tag{9.1}$$

where $\mu^{\text{NC}}_{\text{rSUVR}}$ and $\sigma^{\text{NC}}_{\text{rSUVR}}$ are the mean and standard deviation of the 29 control subjects' rSUVRs.

9.1.4 Voxel-by-voxel analysis in the group space

For the voxel-by-voxel group-wise analysis, all image pairs from the control and the validation datasets were mapped to a common space defined through iterative group-wise non-rigid registration of the T1

[1] Imaging data were provided by the Alzheimer's disease neuroimaging initiative (http://adni.loni.ucla.edu/).

data (Rohlfing et al., 2001; Modat et al., 2014). PET images were brought to the group space by composing the rigid transformations between paired PET and T1 images and the non-rigid transformation between the native T1 images and the group space. After resampling, PET images were smoothed with a Gaussian filter with 5 mm FWHM.

The 22 PET images of the validation dataset were compared with the 29 of the control dataset by expressing the value at each voxel x as a Z-score

$$Z_{\text{group-wise}}(x) = \frac{I_G(x) - \mu_G^{\text{NC}}(x)}{\sigma_G^{\text{NC}}(x)} \quad , \tag{9.2}$$

where I_G corresponds to the subject's PET in the group space, and μ_G^{NC} and σ_G^{NC} are the mean and standard deviation of the 29 subjects of the control dataset in the group space.

9.1.5 Voxel-wise analysis in the subject's space

Analysing the subject's PET image in its native space requires the control dataset to be transported to the target subject space. To do so, each of the 29 MR images of the control dataset was deformed to the target image using an affine followed by a non-rigid registration (Modat et al., 2010). The PET images of the control dataset, pre-aligned to the MR images, were then mapped using the same transformation to the subject MR image. The Z-score between the subject's PET and the entire control dataset aligned to the subject is defined as

$$Z_{\text{native}}(x) = \frac{I(x) - \mu^{\text{NC}}(x)}{\sigma^{\text{NC}}(x)} \quad , \tag{9.3}$$

where I corresponds to the subject's PET image, and μ^{NC} and σ^{NC} are the arithmetic mean and standard deviation of the 29 ADNI2 controls mapped into the native subject space, respectively.

9.1.6 Proposed voxel-wise subject-specific analysis

I propose a novel analysis framework that consists of creating a subject-specific healthy PET template. As in the previous approach (section 9.1.5), the control dataset is transported into the target subject space. A local image similarity measure, here the local normalised cross-correlation extended to irregular ROIs (ROI-LNCC, see section 6.1.1), is then used to estimate the morphological similarity between the subject's MR image and the set of registered MR images from the control dataset. To generate the subject-specific PET Z-score parameters, namely the patient-specific healthy-population mean and standard deviation, the set of registered PETs is locally selected and fused using a voxel-wise weighting scheme. For all of the N control dataset MR images propagated to the target subject's MR image, the ROI-LNCC at each voxel is ranked across all images. This ranking, denoted $r_n(x)$ (with x indexing the voxel and n indexing the propagated MRI) is converted to a weight by applying an exponential decay function $w_n(x) = e^{-\beta r_n(x)}$, with $\beta = 0.5$. Here, $w_n(x)$ represents the weight or contribution of subject n at voxel x to the patient specific model. The value of β influences the repartition of the weights (i.e. the number of subjects contributing to the patient specific model). This parameter was optimised in the context of CT synthesis (section 3.2.2) and the subject-specific PET template may benefit from further optimisation. For each of the N subjects in the control dataset, let the n^{th} mapped PET image be denoted by J_n. The subject-specific Z-score model parameters (I_μ, I_σ) are obtained by a spatially varying

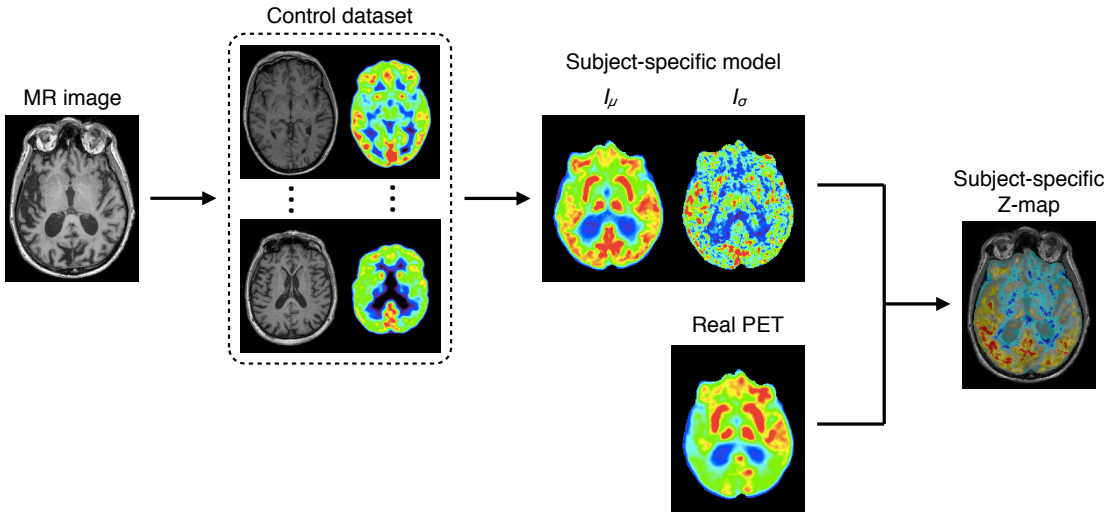

Figure 9.1: Subject-specific PET analysis framework. The control dataset is first transported into the subject space. To generate the subject-specific Z-score parameters, the patient-specific healthy-population mean (I_μ) and standard deviation (I_σ), the set of registered PETs is locally selected and fused. Finally, the subject-specific Z-map is computed using the model parameters.

weighted average

$$I_\mu(x) = \frac{\sum_{n=1}^{N} w_n(x) \cdot J_n(x)}{\sum_{n=1}^{N} w_n(x)} \tag{9.4}$$

$$I_\sigma(x) = \sqrt{\frac{N_w}{N_w - 1} \frac{\sum_{n=1}^{N} w_n(x) \cdot \left(J_n(x) - I_\mu(x)\right)^2}{\sum_{n=1}^{N} w_n(x)}} \tag{9.5}$$

where N_w is the number of non-zero weights. Finally, the subject-specific Z-score is defined as

$$Z_{\text{subject-specific}}(x) = \frac{I(x) - I_\mu(x)}{I_\sigma(x)} \quad . \tag{9.6}$$

9.2 Validation and results

The ^{18}F-FDG PET images of the 22 subjects from the validation dataset were examined using the regional, group-wise, native and proposed subject-specific analyses. Comparisons were restricted to eight clinically relevant regions (Figure 9.2, top) for the sake of brevity. These regions were selected to represent the areas where abnormal uptake, compared with controls, is expected for the four pathologies represented in our dataset:

- a frontal region, comprising the inferior frontal gyrus, precentral gyrus and anterior insula, was defined as relevant for PNFA subjects (Nestor et al., 2003; Rabinovici et al., 2008);
- the anterior temporal region, comprising the hippocampus, amygdala and temporal pole, was defined as relevant for SD (Rabinovici et al., 2008);
- the tempoparietal region, comprising the inferior parietal lobule, posterior middle and superior temporal gyri, was defined as relevant for LPA (Rabinovici et al., 2008);
- finally, the occipital region, comprising the inferior, middle and superior occipital gyri, was defined as relevant for PCA (Crutch et al., 2012).

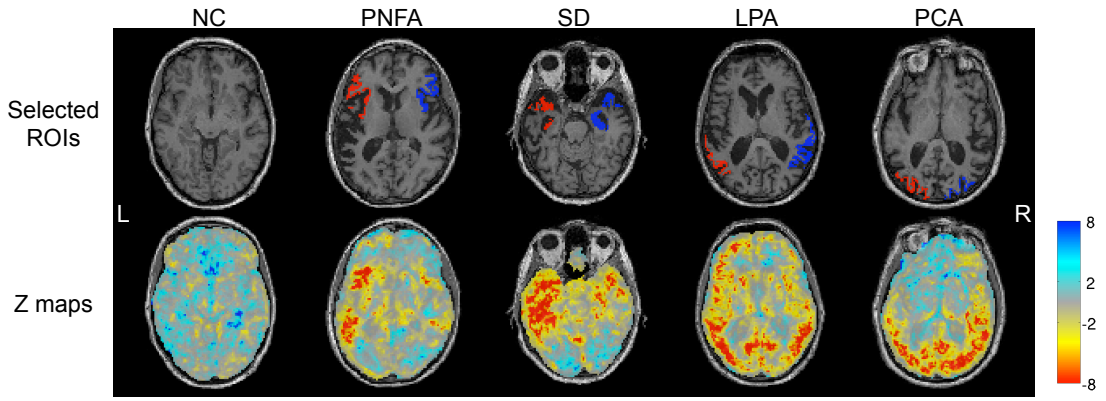

Figure 9.2: T1 images overlaid with the selected ROIs (top) and the patient-specific Z-scores (bottom) for a representative subject of each condition.

Each hemisphere was analysed separately to account for left/right asymmetry.

9.2.1 Subject-specific Z-maps

As a first evaluation of the proposed method, I visually assessed the subject-specific Z-scores. Z-maps obtained for a representative subject of each condition are displayed in Figure 9.2 (bottom). A highly negative Z-score (red) indicates a reduced FDG uptake in the subject relative to the controls. Note that the Z-scores coincide with the regions where uptake abnormalities are expected for each pathology, and that the left/right asymmetries observed for the PNFA, SD, LPA and PCA subjects match the clinical syndromes: PNFA, SD and LPA subjects are expected to have greater left hypometabolism (Rabinovici et al., 2008) while a greater right hypometabolism can be observed on subjects with PCA (Crutch et al., 2012).

9.2.2 Z-score comparison in predefined regions-of-interest

The Z-scores obtained from the rSUVR, and average regional Z-scores obtained using the group-wise, native and proposed subject-specific methods in each ROI are displayed in Figure 9.3. We first note that, using the native and subject-specific methods, the controls have approximately zero Z-scores in all regions, while high Z-scores are observed in the occipital region with the group-wise method. We also note that, when using the proposed method, highly negative Z-scores are observed for each pathology in regions where a reduced uptake is expected when compared with healthy controls. Moreover, the left/right observed asymmetries match the clinical syndromes. These highly relevant Z-score results were stable for all the subjects in each pathological group. The same significance and stability was not observed in the native or group-wise methods.

A Wilcoxon-Mann-Whitney test was used to assess whether the different analysis methods were able to differentiate controls and subjects with pathology. Results showed that the Z_{rSUVR}, Z_{native} and the proposed $Z_{\text{subject-specific}}$ scores could distinguish controls from each of the pathologies at a 5% significance level. With the $Z_{\text{group-wise}}$ score, only controls and PCA subjects were significantly different. These results suggest an improvement in sensitivity with the Z_{rSUVR}, Z_{native} and $Z_{\text{subject-specific}}$ scores when compared with the $Z_{\text{group-wise}}$ score.

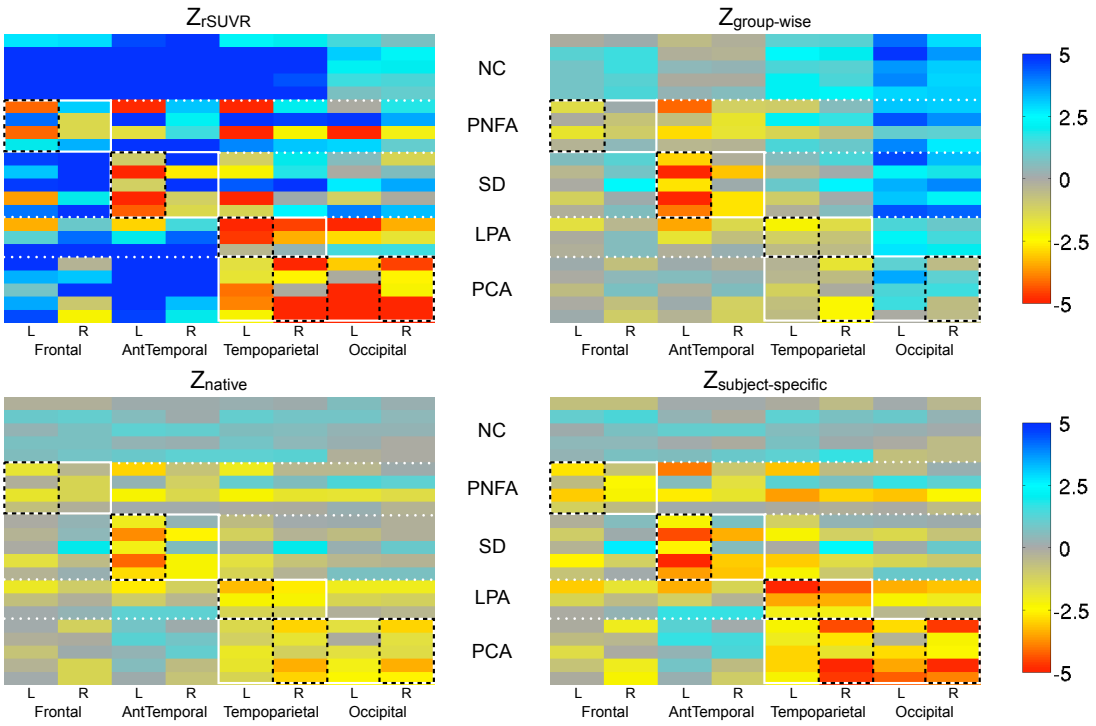

Figure 9.3: Displayed above are the average Z-scores obtained for the rSUVR, group-wise, native and subject-specific methods in each ROI. The white boxes correspond to the regions where abnormal uptake is expected for each of the four pathologies while the black boxes indicate the predominant side when asymmetry is expected.

Z-maps obtained for a representative LPA subject with the different analysis methods are displayed in Figure 9.4. We observe higher negative Z-scores in the relevant ROIs with the subject-specific approach than with the other methods.

9.3 Discussion and conclusion

In this chapter, I analyse ^{18}F-FDG PET data in the original subject space by providing voxel-wise statistics of normality/abnormality. The subject PET image is compared using a Z-score to a subject-specific PET model obtained through the propagation of morphologically-matched PET scans from a control dataset.

We first observed that, when analysing the PET images in the native subject space, the normal controls have low Z-scores in all regions, which was not always the case with the other methods (Figure 9.3). We note that the Z-scores obtained with the proposed method coincide with the regions where uptake abnormalities are expected for each of the pathologies studied and respect the left/right asymmetry (Figures 9.2 & 9.3). Finally, it appears that these highly negative Z-score results are stable across all subjects in each pathological group, which is not the case with the other methods (Figure 9.3).

The group-wise analysis seems strongly affected by uncertainties in the group-wise registration, driven by subjects with a large amount of atrophy (i.e. subjects with PCA), and the large variations in the normal population. Analysing the PET data in the native space avoids registering and resampling the subject PET into the group space. Group-wise, but also pair-wise, registrations could be improved by

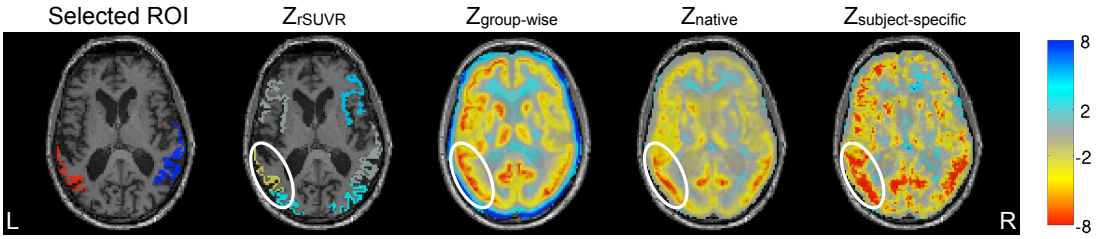

Figure 9.4: Z-maps obtained with the different analysis methods for a subject with LPA. The white ellipses indicate the predominant side where abnormal uptake is expected.

using additional information such as tissue classification (Heckemann et al., 2010). Furthermore, in the subject-specific method, only the most morphologically similar controls per target are selected to build the model, which reduces the variance of the normal population used for comparison in the Z-score, thus increasing the sensitivity. The low Z-scores systematically observed for the healthy subjects suggest that the subject-specific analysis is less prone to false positives. Finally, in contrast with rSUVR-based methods, the proposed analysis is not restricted to predefined regions.

While the method offers greater sensitivity, this is not its only purpose. It is my hope that, by disentangling the measurement of atrophy and metabolic decline, this method may provide a greater understanding of neurodegenerative diseases. Future work will involve validating the method on a larger dataset to provide more quantitative results.

Chapter 10

CT synthesis for MR-based radiotherapy treatment planning

In 2015, the number of people living with cancer in the UK is estimated at 2.5 million, rising to 4 million by 2030 (Maddams et al., 2012). Radiotherapy is a common treatment for many types of cancer: about four in ten patients whose cancer is cured receive radiotherapy as part of their treatment (Department of Health, 2012). The aim of radiotherapy treatment planning (RTP) is to deliver an optimal dose of radiation over the target area while sparing the normal tissues. RTP first requires contouring the target and organs at risk (OAR). Once these volumes have been defined, the optimal dose distribution for treating the tumour is determined according to the attenuation properties of the different tissues. Most radiotherapy treatments are planned using a CT scan of the patient. The acquisition of a CT is fast and, as we have already seen, the tissue attenuation coefficients can easily be derived from the intensity values in Hounsfield units. However, CT images have low soft tissue contrast, which can lead to large variations when defining the tumour, particularly when located in the brain, head & neck, or prostate. MRI is often preferred over CT as a structural imaging modality, mainly for its excellent soft-tissue contrast. MRI can provide an in-depth understanding of the underlying pathophysiology by imaging the anatomical, micro-structural and functional characteristics of the tissue. Currently, the use of MRI in RTP is limited by the fact that MRI does not provide photon density information, hampering the calculation of dose distributions.

To overcome this limitation, a solution is to recreate a CT image from the available MR images. Several methods exist to obtain synthetic CT images and many have been applied to RTP. Results presented in Jonsson et al. (2015) are obtained from a Gaussian mixture regression model linking the MRI intensity values to the CT HU. In Korhonen et al. (2014), bones are manually segmented and the MRI intensity values are converted to HU using a dual model, within and outside of the bone class. Other approaches, the atlas-based methods, rely on a single (Dowling et al., 2012) or a database (Sjölund et al., 2015; Gudur et al., 2014; Uh et al., 2014) of MR and CT image pairs and consist of registering each atlas MR image to the target MR image, applying the same transformation to the associated CT image and finally, for multi-atlas methods, fusing the registered CT images. The fusion can be obtained by computing the voxelwise median (Sjölund et al., 2015), using a probabilistic Bayesian framework (Gudur et al.,

2014), an arithmetic mean process or pattern recognition with Gaussian process (Uh et al., 2014).

10.1 Robust CT synthesis in the head & neck region

Most of the methods mentioned above are able to generate CT images in the brain (Sjölund et al., 2015; Jonsson et al., 2015; Gudur et al., 2014; Uh et al., 2014), some in the pelvic area (Dowling et al., 2012; Korhonen et al., 2014), but none in the neck. CT synthesis in the neck is challenging for three main reasons. First, the mixture of bone and air present in this area makes the conversion of MRI intensity values to HU difficult as both bone and air have usually low intensities in MR images. A second challenge comes from the wide range of target image fields of view. Images with large axial FOV can cover an area starting from the top of the lungs to the middle of the head (Figure 10.1, bottom), while images with small axial FOV (Figure 10.1, top) only focus on a target area, such as a tumour. These disparities are a problem when aligning the atlas images to the target. The last challenge arises from the large-scale postural changes, such as flexion or extension of the neck, or the position of the jawbone, which reduces the performances of registration methods.

I propose to redesign the synthesis process and present an iterative multi-atlas algorithm to synthesise CT images in the neck region based on the CT synthesis method developed through this thesis. The contribution of this chapter, compared to the current atlas-based methods, consists of three points.

1. To form the database, the CT and MR images are non-rigidly aligned to account for the different positions between the two acquisitions. All the MR-CT pairs are also aligned to a common coordinate frame.
2. The first step to synthesise a pseudo CT is to register all the atlas MR images to the target MR image. Large differences in the FOV were observed between the subjects, which can hinder the inter-subject registration. To overcome this problem, I propose a robust alignment exploiting the fact that all the atlases are pre-aligned in the same coordinate frame.
3. The algorithm relies on the ability to accurately map T2 images from different subjects, a process that can be challenging, particularly in low-contrast areas. I propose to combine multiple modalities, an initial pseudo CT and the target MR image to improve the synthesis accuracy in the bone region.

This work, done in collaboration with Dr Jamie McClelland at UCL, and Filipa Guerreiro and Dr Antje-Christin Knopf from the Institute of Cancer Research, has been published in Burgos et al. (2015c), Burgos et al. (2015d) and Guerreiro et al. (2015).

10.1.1 Method

The proposed iterative multi-atlas algorithm aims at synthesising CT from MR images of the neck region using a database of non-rigidly aligned MR and CT image pairs. In this section, I apply a robust process to align the atlas images to the target image and propose an iterative process aiming at improving the synthesis in the bone region, critical for radiotherapy planning. A diagram illustrating the proposed method is shown in Figure 10.2.

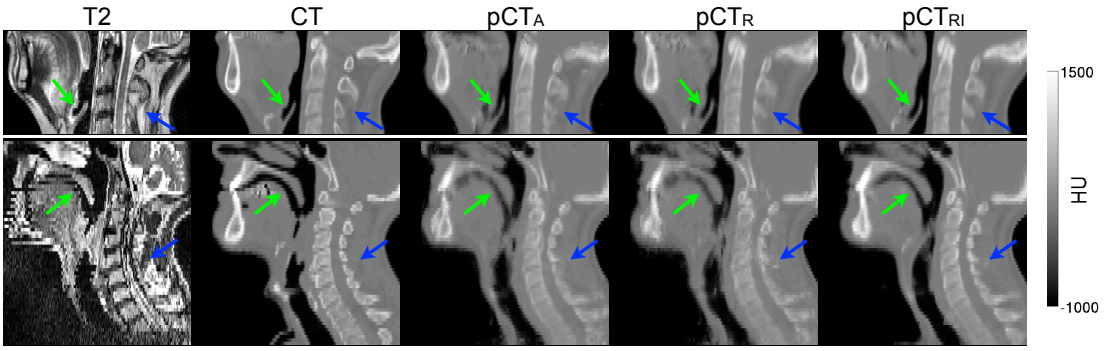

Figure 10.1: Examples of T2-w MRI, CT, and pseudo CT images for a subject from dataset 1 (top) and dataset 2 (bottom). pCT_A was obtained using a single affine transformation between the atlases and target, pCT_R using the robust affine transformation and pCT_{RI} after the robust affine transformation and the iterative bone refinement. Note that the method is able to generate a pseudo CT even in the presence of motion and large-scale postural changes such as neck flexion.

10.1.1.1 MR-CT database building

The CT synthesis method relies on pre-acquired pairs of T2-weighted MR and CT images of the neck. For each subject, the MR image was mapped to the CT using a non-rigid deformation algorithm (Modat et al., 2010) to compensate for neck flexion. The MR image from the atlases were then mapped to a common coordinate frame via an affine groupwise registration (Rohlfing et al., 2001; Modat et al., 2014). The transformations were then applied to the MR-CT pairs by updating their image coordinate system, thus forming a database of MR and CT images aligned in a common space.

10.1.1.2 Inter-subject mapping

The first step to synthesise a CT for a given MR image is to register all the MR images in the atlas database to the target MR image. As we have seen in the previous chapters, this inter-subject coordinate mapping can be obtained using a symmetric global registration followed by a non-rigid registration. However, when the FOV of the target MR image is limited, which can occur when a tumour is the sole target of the imaging protocol, the affine alignment can be inaccurate. To overcome this weakness, a robust affine transformation, similar to the one proposed by Klemt et al. (2015), which relies on the fact that the atlases are aligned to the same space, is used.

Robust affine transformation The robust affine alignment consisted of three steps. Each atlas MR image was first affinely mapped to the target. The average transformation, computed in the log space, was obtained from all the pairwise affine transformations. This average affine transformation was then used to initialise a second affine registration step to refine the alignment. As all the atlases were aligned to the same space, applying the average affine transformation to all of them guarantees that each atlas is initially aligned with the target.

Non-rigid registration The robust affine alignment between atlas and target images was used to initialise a cubic B-spline parametrised non-rigid registration using a stationary velocity field, normalised mutual information as a measure of similarity and a final grid spacing of $15\times15\times15$ mm^3 (Modat et al., 2012). These non-rigid transformations were also applied to all the CTs in the atlas database. Through this registration and resampling procedure, one obtains a series of MR/CT pairs aligned to the target MRI.

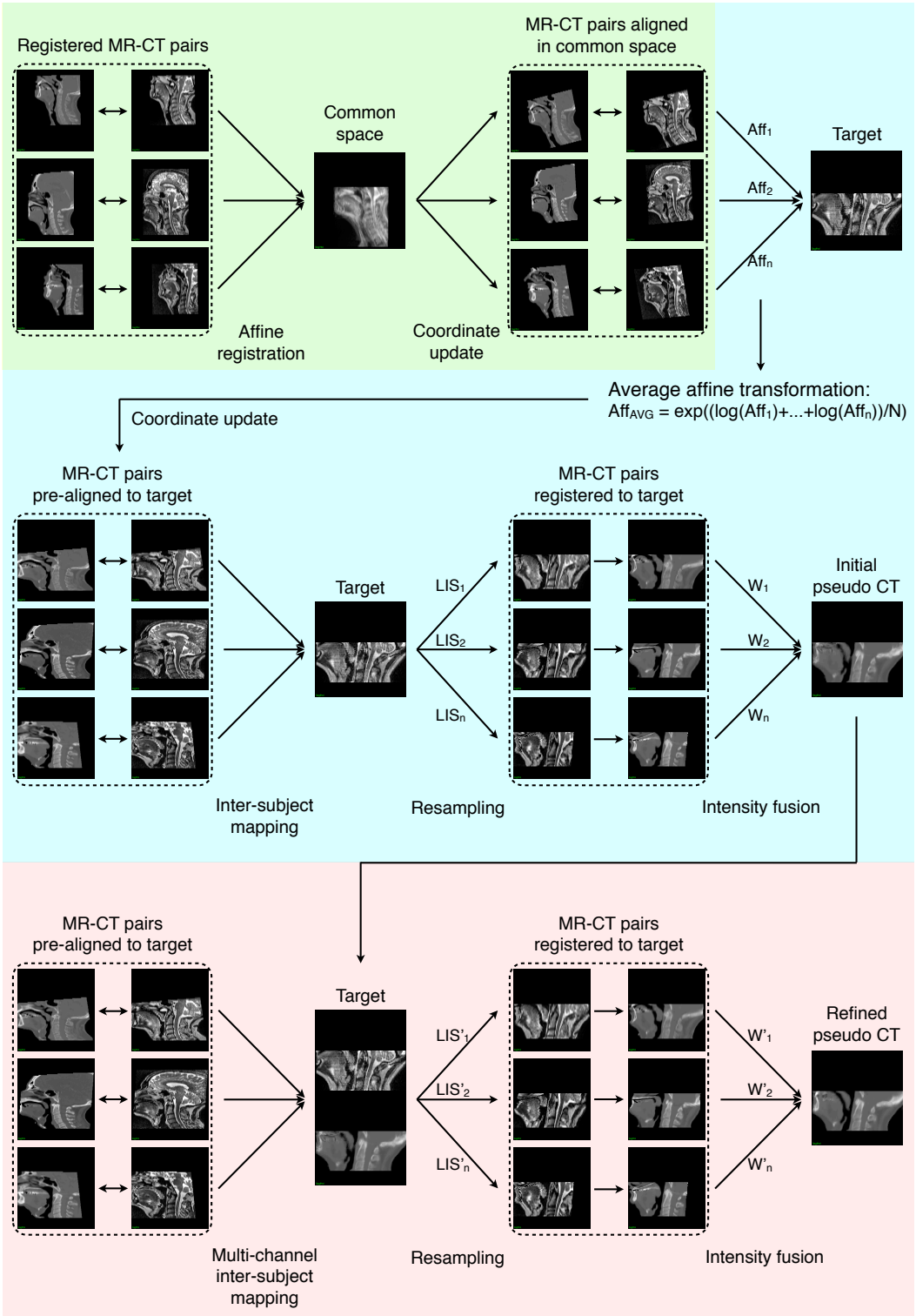

Figure 10.2: Diagram of the CT synthesis in the head & neck region. A preliminary step is required to build the MR-CT database (green). In the next step (blue), an initial pseudo CT is generated. All the MR images in the database are registered to the target MR image. The atlas CTs are then mapped using the same transformations to the target MR image. A local image similarity measure (LIS) between the mapped and target MR images is converted to weights (W) to reconstruct the pseudo CT. In a final step (red), the bone is refined through an iterative process. Following a similar process, a refined pseudo CT is obtained from a new target comprising the target MR image and the initial pseudo CT.

10.1.1.3 CT synthesis

The pseudo CT was obtained by fusing the mapped atlases according to their morphological similarity to the target. A local image similarity measure between the target MR image and the set of registered MR images from the database was used as a surrogate of the underlying morphological similarity, under the assumption that if two MR images are similar at a certain spatial location, the two CT images will also be similar at this location.

Image/Morphological Similarity Due to different acquisition FOVs, the inter-subject mapping and re-sampling processes introduce areas where no information is available. Those areas have to be accounted for when the similarity measure is computed and during the intensity fusion process. To assess the morphological similarity between target subject's MR image (I^{MRI}) and each of the N atlases in the database (J_n^{MRI}, $n \in N$), I used the local normalised cross-correlation extended to irregular ROIs (ROI-LNCC, see section 6.1.1).

Intensity Fusion The ROI-LNCCs at each voxel were ranked across all atlas images in the database and the ranks, noted as $r_n(x)$, were converted to weights by applying an exponential decay function $w_n(x) = e^{-\beta r_n(x)}$ with $w_n(x)$ being the weight associated with the n^{th} mapped atlas image at voxel x and $\beta = 0.5$. As in the original method, the final pseudo CT (I^{pCT}) was obtained by applying a spatially varying weighted averaging

$$I^{pCT}(x) = \frac{\sum_{n=1}^{N} w_n(x) \cdot J_n^{CT}(x)}{\sum_{n=1}^{N} w_n(x)} \quad . \tag{10.1}$$

10.1.1.4 Iterative bone refinement process

In contrast to CT images, T2-weighted MR images do not provide a good estimate of the bone location. I propose to combine multiple modalities to regularise the registration in low-contrast areas, providing more realistic mappings.

An initial pseudo CT (pCT) was synthesised following the method described previously. This pCT was then combined with the MR image to form an MR-pCT pair. The MR-pCT pair was registered to all the MR-CT pairs from the database. The inter-subject coordinate mapping was obtained using the robust affine transformation followed by a multi-channel non-rigid registration. Normalised mutual information was used as a similarity measure for the T2-weighted MR channel while the sum of squared differences was computed for the second channel, exploiting the quantitative property of the CT intensities. A refined pseudo CT was obtained by fusing the mapped MR-CT pairs according to their morphological similarity to the target MR-pCT pair, which was assessed using a multivariate LNCC (MV-ROI-LNCC) defined as MV-ROI-LNCC$_n$ = ROI-LNCC $\left(I^{MRI}, J_n^{MRI}\right)$ + ROI-LNCC $\left(I^{pCT}, J_n^{CT}\right)$ (see section 7.1.1).

10.1.2 Validation and results

Data

Images from two retrospective studies were used to build the MR-CT database and validate the proposed method.

Dataset 1: Small axial FOV. Six subjects with a small axial FOV were used to assess the robustness of the method. They have both T2-weighted MRI (1.5 T; 2D spin echo; TE/TR: 13/794 ms; voxel size $1\times1\times2$ mm^3, matrix size $192\times192\times40$) and CT (voxel size $1\times1\times2$ mm^3, matrix size $512\times512\times200$, 120 kVp) images.

Dataset 2: Large axial FOV. Seventeen subjects with a large axial FOV were used to build the database and validate the method. They have both T2-weighted MRI (1.5 T; 2D spin echo; TE/TR: 107/7000 ms; voxel size $0.7\times0.7\times3.3$ mm^3, matrix size $256\times256\times60$) and CT (voxel size $1\times1\times2.5$ mm^3, matrix size $512\times512\times160$, 120 kVp) images.

10.1.2.1 Algorithmic comparison

Subjects from dataset 2 were used to build the database. Using the proposed technique, I first synthesised pseudo CTs for all subjects in dataset 1 to study the benefits of the robust affine compared with a single affine transformation. I then performed a leave-one-out cross validation using all the subjects from dataset 2 to study the impact of the bone refinement process on the pseudo CT images. For each subject in both datasets, three pseudo CTs were synthesised:

- pCT_A, obtained using a single affine transformation between the atlases and target;
- pCT_R, obtained using the robust affine transformation;
- pCT_RI, obtained after the robust affine transformation and the iterative bone refinement.

The mean absolute error (MAE) and the standard deviation of the absolute error (SAE) were calculated for every subject between the reference CT non-rigidly aligned to the MR (R^{CT}) and each of the pseudo CTs (I^{CT}), in a region of interest comprising V voxels: $\text{MAE} = \frac{1}{V}\sum_x |I^{CT}(x) - R^{CT}(x)|$, $\text{SAE} = \frac{1}{V-1}\sqrt{\sum_x (|I^{CT}(x) - R^{CT}(x)| - \text{MAE})^2}$. The MAE gives information on the amount of error while the SAE gives information on the amount of dispersion of the error. I focused the validation on three regions: air (< -100 HU), soft-tissue (between -100 and 300 HU), and bone (>300 HU). As inaccuracies exist in the registration between the real CT and T2-weighted images, I also provide a reference-free metric using the entropy of the pseudo CT images in the frequency domain as a measure of sharpness: $\text{FDE} = -\sum(f\log_2(f))$ where f is the normalised absolute amplitudes of frequencies of the pseudo CT image (Kristan and Pernus, 2004). Statistical significance was assessed using the paired, one-tailed, Wilcoxon signed-rank test at the 5% significance level.

10.1.2.2 Robust affine transformation: validation with small axial FOV

The average and standard deviation (SD) of the MAE, SAE and FDE metrics are presented in Table 10.1. Using the robust instead of a single affine transform decreases the MAE, SAE and FDE in all the regions. Colour coded statistical test results are presented in Figure 10.3. These results show significant improvements when comparing synthesis using the robust affine to synthesis using a single affine transformation. An example of MR, CT and pCT images are displayed in Figure 10.1 (top).

10.1.2.3 Iterative bone refinement: validation with large axial FOV

After one iteration of the bone refinement process, the MAE and SAE in the bone region and the FDE are significantly decreased (Table 10.1 & Figure 10.3). An example of MR, CT and pCT images are

Table 10.1: Average ± SD of the MAE and SAE computed between the reference CT and the pseudo CTs, and of the FDE computed for each pseudo CT.

		Dataset 1			Dataset 2		
		pCT_A	pCT_R	pCT_{RI}	pCT_A	pCT_R	pCT_{RI}
MAE	Bone	204.5 ± 19.2	193.6 ± 23.2	196.8 ± 16.0	208.0 ± 19.6	205.2 ± 18.2	192.1 ± 13.4
(HU)	Soft	41.2 ± 1.7	40.2 ± 2.2	39.1 ± 1.9	41.1 ± 5.3	40.6 ± 5.1	40.4 ± 4.6
	Air	63.4 ± 8.4	55.6 ± 8.4	56.6 ± 10.3	133.8 ± 29.4	133.0 ± 23.0	126.7 ± 25.4
SAE	Bone	201.8 ± 40.0	189.5 ± 45.1	186.9 ± 34.9	184.4 ± 14.8	182.0 ± 14.1	169.7 ± 10.9
(HU)	Soft	45.8 ± 1.6	44.5 ± 2.1	43.4 ± 2.0	46.5 ± 3.7	46.1 ± 3.7	46.0 ± 3.4
	Air	114.7 ± 11.4	106.0 ± 11.1	108.6 ± 13.7	145.4 ± 18.5	143.8 ± 13.1	150.2 ± 20.6
FDE	All	18.40 ± 0.12	18.11 ± 0.13	17.77 ± 0.13	19.73 ± 0.32	19.69 ± 0.32	19.44 ± 0.34

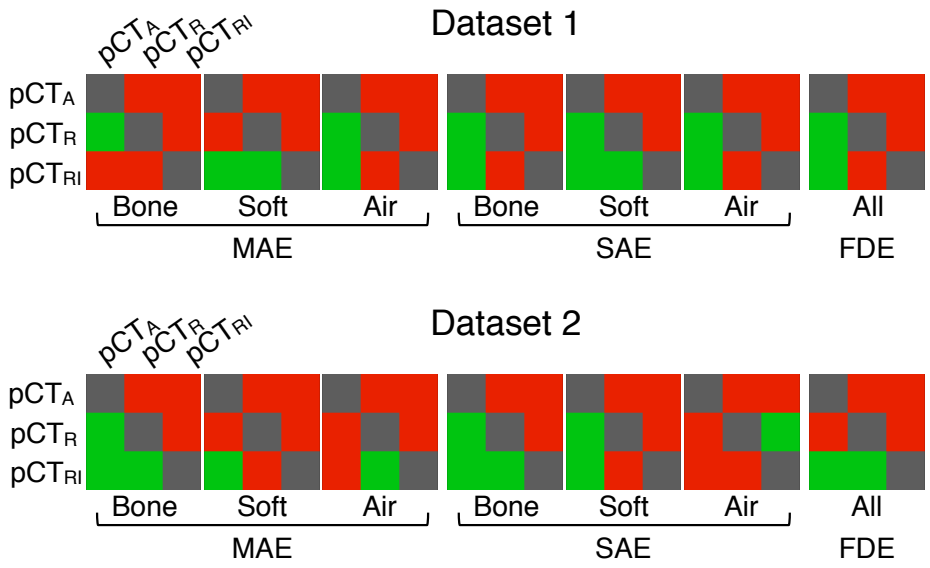

Figure 10.3: Results of the one-tailed Wilcoxon signed-rank test at the 5% significance level for the MAE, SAE and FDE metrics. The colour green indicates a significant decrease for the row method when compared to the column method, while the red indicates that the difference is not significant.

displayed in Figure 10.1 (bottom).

10.1.2.4 Case study: dosimetry calculations

To test the impact of the proposed improvements in RTP, dose calculations were performed for a test subject from dataset 1 by Filipa Guerreiro. We compared the cumulative dose volume histogram (DVH) obtained for the pseudo CTs to the DVH obtained for the reference CT image in the planning target volume (PTV). The DVHs displayed in Figure 10.4 show a close agreement between the pseudo CTs and the CT. A 2D gamma analysis (Low et al., 1998), evaluated at 2%/2 mm dose difference/distance to agreement, was used to compare axial dose distributions. A gamma index greater than 1 means that the calculation does not meet the acceptance criteria. The gamma maps displayed in Figure 10.4 show that the robust affine improves the results compared with a single affine transformation and that the bone refinement process further reduces the error to an acceptable range ($\gamma < 1$). Results obtained for the other subjects are available in Guerreiro (2015).

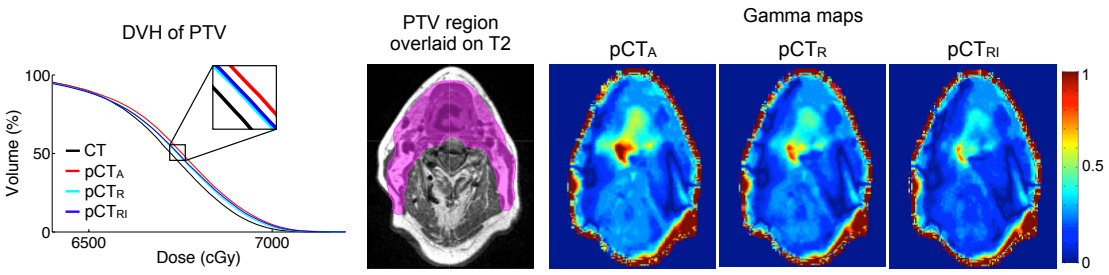

Figure 10.4: Results of the dose calculations performed for a test subject from dataset 1.

10.2 Multi-contrast CT synthesis in the pelvic region

The superior soft-tissue contrast of MR images is also valuable for visualising organs and determining target volumes in other areas of the body. In this section, I synthesise pseudo CT images for radiotherapy treatment planning in the pelvic region. This work, done in collaboration with Filipa Guerreiro and Dr Antje-Christin Knopf from the Institute of Cancer Research, and Dr Jamie McClelland at UCL, has been published in Burgos et al. (2016) and Guerreiro et al. (2015).

10.2.1 Method

Data

Sixteen subjects were used to evaluate the proposed methodology. Each subject had a T1-weighted MR image (3 T; 2D spin echo; TE/TR: 10/400 ms; voxel size $1.64 \times 1.64 \times 5$ mm^3), a T2-weighted MR image (3 T; 2D spin echo; TE/TR: 80/2500 ms; $1.46 \times 1.46 \times 5$ mm^3), and a CT image (voxel size $0.98 \times 0.98 \times 1.5$ mm^3, 140 kVp), all acquired on the same day.

10.2.1.1 Database building

A multi-contrast MR-CT database consisting of T1, T2, T1-T2 pair and CT images of 15 subjects was created by non-rigidly registering for each subject both the CT and T1 images to the T2 image. As the image FOVs were consistent amongst the subjects, the alignment to a common space was not necessary.

10.2.1.2 CT synthesis

Pseudo CT images were synthesised from T1 images, T2 images and T1-T2 image pairs. The inter-subject coordinate mapping between MR images, either T1s, T2s or T1-T2 pairs, was obtained using a symmetric global registration followed by a cubic B-spline parametrised non-rigid registration using a stationary velocity field, normalised mutual information as a measure of similarity and a final grid spacing of $15 \times 15 \times 15$ mm^3, as implemented in NiftyReg (Modat et al., 2012). All the CTs in the database were then mapped to the target subject using the transformation that maps the subject's corresponding MR image in the database to the target MR image. The ROI-LNCC or MV-ROI-LNCC was used for the local atlas ranking. As in the previous section, an iterative process was used to refine the synthesis in the bone region. An initial pseudo CT was combined with the T1, T2 or T1-T2 pair to form an MR-pCT pair. The MR-pCT pair was registered to all the MR-CT pairs from the database and a refined pseudo CT was obtained by fusing the mapped MR-CT pairs according to their morphological similarity to the target MR-pCT pair.

Table 10.2: For 15 subjects: average ± SD of the MAE and ME computed between the reference CT and the pseudo CTs synthesised from a T1 image, T2 image and T1-T2 image pair using the single affine transformation and the iterative bone refinement process.

		Single affine transformation			Iterative bone refinement		
		$pCT_{A,T2}$	$pCT_{A,T1}$	$pCT_{A,T1,T2}$	$pCT_{AI,T2}$	$pCT_{AI,T1}$	$pCT_{AI,T1,T2}$
MAE (HU)	All	41.1 ± 3.3	41.4 ± 3.4	40.9 ± 3.2	43.7 ± 4.5	44.2 ± 4.5	41.6 ± 3.6
	Bone	118.3 ± 13.4	117.3 ± 12.9	116.7 ± 13.2	116.4 ± 10.9	116.7 ± 10.5	115.5 ± 11.2
ME (HU)	All	-1.4 ± 9.3	-1.8 ± 9.3	-1.4 ± 9.2	-5.9 ± 10.2	-6.6 ± 9.8	-2.9 ± 9.6
	Bone	-31.3 ± 31.0	-30.6 ± 30.9	-30.2 ± 31.3	-6.5 ± 32.7	-6.8 ± 32.9	-12.8 ± 32.3

10.2.2 Validation and results

10.2.2.1 Algorithmic comparison

The performance of the synthesis algorithm was compared with reference data for 15 subjects following a leave-one-out cross-validation scheme. For each subject, a total of six pseudo CTs were synthesised:

- $pCT_{A,T1}$, using a single affine transformation on the T1 image;
- $pCT_{A,T2}$, using a single affine transformation on the T2 image;
- $pCT_{A,T1,T2}$, using a single affine transformation on the T1,T2 image pair;
- $pCT_{AI,T1}$, using a single affine transformation and the iterative bone refinement on the T1 image;
- $pCT_{AI,T2}$, using a single affine transformation and the iterative bone refinement on the T2 image;
- $pCT_{AI,T1,T2}$, using a single affine transformation and the iterative bone refinement on the T1,T2 image pair.

The mean absolute error (MAE) and the mean error (ME) were calculated for every subject between the reference CT and each of the pseudo CTs. Statistical significance was assessed using the paired, one-tailed, Wilcoxon signed-rank test at the 5% significance level. Pseudo CTs were also generated for an additional subject presenting metal artefacts, thus not included in the database nor in the global results.

10.2.2.2 Results

The average ± SD of the MAE and ME across 15 subjects are presented in Table 10.2 and a summary of the significance tests between the different methods is displayed in Figure 10.5. We observe that combining MRI contrasts significantly improves the synthesis accuracy, both at the initial stage using the single affine transformation and after bone refinement. These results also show that even if the bone refinement process decreases the overall accuracy, it improves the synthesis and reduces the bias in the bone region.

Examples of pseudo CTs obtained from a T1-T2 image pair for a representative subject and a subject with a hip implant are displayed in Figure 10.6. When no metal artefacts are present, the method is able to generate accurate pseudo CT images. However, for the subject with the metallic hip implant, the MRI signal drops and the method is unable to generate accurate results in the region affected by the artefacts. The MAE obtained for this subject was of 85 HU over all the tissues and 381 HU in the bone.

Dose calculations were performed for these subjects and are available in Guerreiro (2015).

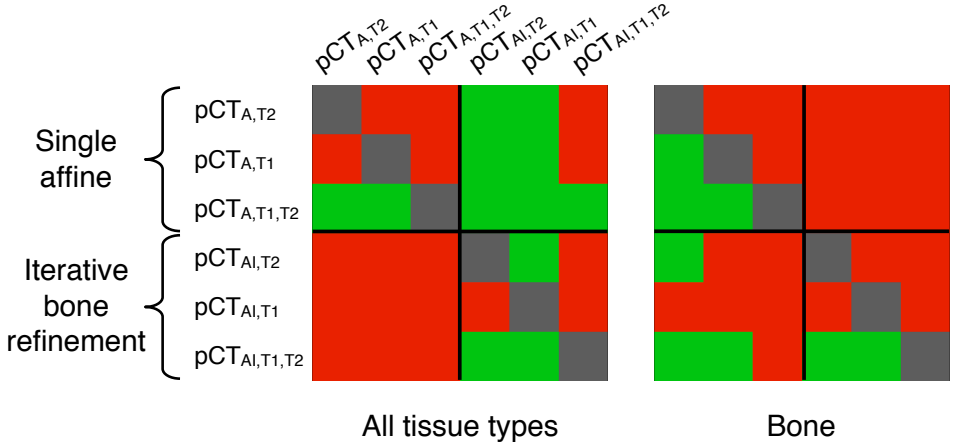

Figure 10.5: Results of the one-tailed Wilcoxon signed-rank test at the 5% significance level for the MAE. The colour green indicates a significant decrease for the row method when compared to the column method, while the red indicates that the difference is not significant.

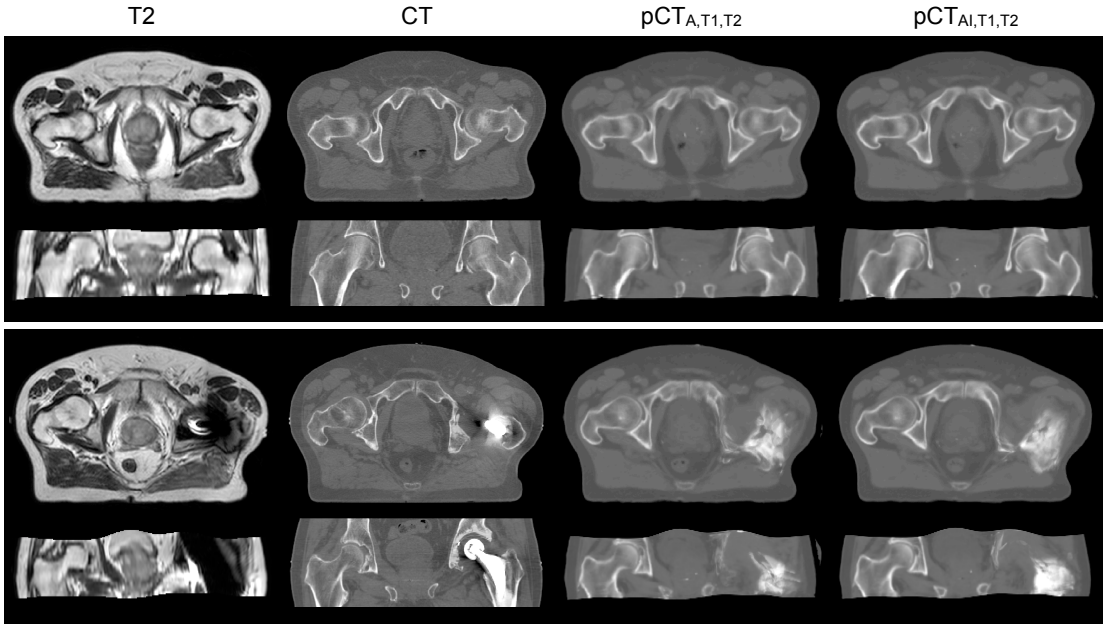

Figure 10.6: Examples of CT synthesis in the pelvic region for a representative subject (top) and a subject with a hip implant (bottom). From left to right: the T2 image, reference CT and pseudo CTs obtained from a T1-T2 pair using a single affine transformation before (pCT$_{A,T1,T2}$) and after (pCT$_{AI,T1,T2}$) bone refinement.

10.3 Discussion and conclusion

This chapter tackles the problem of MR-based radiotherapy treatment planning in the head & neck and pelvic areas by synthesising CT from MR images using an iterative multi-atlas approach. The proposed method relies on pre-acquired pairs of non-rigidly aligned MR and CT images. To synthesise a pseudo CT, all the MR images in the database are first registered to the target MR image using a robust affine transformation followed by a deformable registration. An initial pseudo CT is obtained by fusing the mapped atlases according to their morphological similarity to the target. This initial pseudo CT is then combined with the target MR image in order to improve both the registration and fusion stages and refine

the synthesis in the bone region.

I first applied the method to the head & neck region and showed that the proposed CT synthesis algorithm is able to generate pseudo CT images in a challenging region for registration algorithms. The results displayed in Table 10.1 demonstrate that the robust affine decreases the overall absolute error compared to a single affine transformation, mainly in images with small axial field-of-view, whilst the bone refinement process further reduces the error in the bone region, increasing image sharpness. Most of the errors observed when comparing with results obtained in the brain can be explained by inaccuracies in the inter-subject registrations due to a complex mixture of tissues present in the neck area, and by large epiglottis/tongue mismatch between MR and CT data. As a proof of concept that the method could be used for MR-based RTP, dose calculations were performed for a test subject (Figure 10.4), showing close agreement between the proposed pseudo CT and the reference CT, within acceptable error margins ($\gamma < 1$).

As a second step, I applied the method to the pelvic region and showed that the proposed algorithm can generate accurate pseudo CT images using a single MR image or a combination of MR images as an input. The results displayed in Table 10.2 demonstrate that the absolute error is lower when MRI contrasts are combined, and that the bone refinement process reduces the error in the bone region. I also showed that the presence of metallic implants hinders the synthesis of an accurate pseudo CT.

Further experiments are required to verify the suitability of this proposed framework for dose calculation and to study the effect of anatomical abnormalities, such as tumours, on the results. I will also explore the effect of the number of iterations on the synthesis accuracy.

Finally, note that while the main focus in this chapter was to estimate dose deposition in the context of MR-based RTP, the proposed method could also be used for attenuation correction in PET/MR imaging studies.

Chapter 11

General conclusions

11.1 Summary

One of the factors limiting the use of PET/MR scanners, especially in the case of neurology studies, is the imperfect attenuation correction, leading to a strong bias of the PET activity. My first goal was to improve MR-based attenuation correction in the brain region to reach the quality of the CT-based attenuation correction achieved on PET/CT scanners.

To do so, I developed a new method to correct for attenuation PET/MR data by synthesising pseudo CT images from a single MR image or a combination of sequences. This multi-atlas CT synthesis method relies on a pre-acquired set of aligned MR and CT image pairs from multiple subjects forming an MR-CT database. We have seen that a minimum of 15 atlases is necessary to guarantee accurate results and that increasing the number of atlases reduces the synthesis error. When dealing with large databases, pre-selecting atlases based on their global morphological similarity to the target improves the synthesis accuracy while maintaining a reasonable computational time.

To generate a CT from a target MR image, each MR image from the database is deformed to the target MR image using affine followed by non-rigid registration. The CT images in the database are then mapped using the same transformation to the target MR image. A local image similarity measure between the target MR image and the set of registered MR images from the database is used as a surrogate of the underlying morphological similarity, under the assumption that if two MR images are similar at a certain spatial location, the two CTs will also be similar at this location. Finally, the set of registered CTs is fused using a voxel-wise weighting scheme, generating a pseudo CT. We have seen that taking into account the FOV mismatches between target and atlas images during the fusion step improves the CT synthesis accuracy at the borders of the field of view.

The multi-contrast multi-atlas CT and attenuation map synthesis algorithm was validated using two different PET tracers: ^{18}F-FDG and ^{18}F-florbetapir. I showed that the absolute difference between the PET images corrected for attenuation with the reference CT-based attenuation maps and the PET images corrected using the synthetic attenuation maps was, on average, less than 2%, with less than 1% bias. I consider these results satisfactory enough to provide an accurate attenuation correction in the brain region, thus allowing an unbiased analysis of the PET images.

My second objective was to develop a new framework for the analysis of FDG PET data in the brain to improve the differentiation of diseases by better identifying patterns of metabolic abnormality. The framework developed combines the advantages of both regional and voxel-wise approaches by analysing PET data in the original subject space while still providing voxel-by-voxel statistics of normality/abnormality. This is achieved through a subject-specific PET model based on the propagation of morphologically-matched PET images. By accounting for inter-subject morphological differences, the proposed method reduces the variance of the normal population used for comparison and increases the sensitivity. I showed that the method was able to accurately distinguish subgroups in a dataset comprising subjects with distinct neurodegenerative syndromes.

The application of the CT synthesis method is not limited to PET/MR attenuation correction. My last objective was to develop a new method to derive tissue attenuation properties from MR images in the head & neck and pelvic regions to facilitate MR-based radiotherapy treatment planning. To do so, I redesigned the CT synthesis process developed for brain attenuation correction. I showed that this new iterative multi-atlas algorithm was able to synthesise CT images in the neck and pelvis, regions challenging for registration algorithms.

11.2 Future research directions

A limitation of the proposed CT synthesis method is its poor ability to handle subjects with abnormalities affecting the morphology, particularly of bones. As no close match exist in the database, the accuracy of the registrations between the target and all the atlases is limited and cannot be compensated by the local atlas ranking. The method will also have difficulties when artefacts are present in the target MR image. We have seen in chapter 10 (Figure 10.6) that the method was not able to generate an accurate pseudo CT from a target MR image with important artefacts caused by a metallic hip implant. In these two situations, the values of the local similarity measure computed between the target MR image and each atlas could be used to detect outliers. For attenuation correction purposes, a simple solution could then be to apply soft-tissue values to these regions.

Although the synthesis method is able to generate pseudo CT images with accurate skull thickness, producing accurate results when the subject presents an unusual skull density is challenging. This is explained by the fact that none of the sequences used in this thesis as an input for the synthesis process capture the bone signal. A way to mitigate this limitation could be to use the UTE sequence, which makes the imaging of bone possible despite its very short spin-spin relaxation time (T2) (Robson et al., 2003). Horch et al. (2010) showed using this sequence that the water bound to the collagen in cortical bone (higher density) has a shorter T2 than the water present in the porous regions of cortical bone (lower density). As T2* comprises T2 relaxation, it is expected that changes in R2* values (R2* = 1/T2*), which can be calculated from two UTE echos (see section 2.3.2), would reflect changes in bone density. This property could be exploited for example by synthesising CT images from UTE images. Having signal in the bone regions should improve the registrations and help select the atlases with the closest bone density. Exploiting MRI phase information could be another approach to explore. MR phase

images contain information about local magnetic susceptibility sources in the brain and can be used to reconstruct susceptibility maps. Buch et al. (2015) showed that susceptibility imaging can be used to image bone, which is more diamagnetic than most of the soft tissues in the body, but further work is necessary to assess the ability to measure bone density.

In chapter 10, we saw that the CT synthesis method could be applied to other regions than the brain. By redesigning the method, pseudo CT images were synthesised in the head & neck and pelvic regions. An additional step would be to test the ability of the method to generate pseudo CT images in other body parts, for example the lungs. Lungs are particularly challenging for registration algorithms and building a representative database would require a large number of subjects (> 100) as the inter-subject variability is high. Susceptibility imaging could also play an important role in this region.

In chapter 9, I developed a new framework for the analysis of FDG PET data that consists of creating a subject-specific healthy PET model using the subject's T1-w MR image and a database of T1-w MRI and FDG PET scans from healthy subjects. This framework was used to help distinguish neurodegenerative syndromes but could also be applied to other modalities and tasks. A potential application is the study of deviations in brain perfusion through the synthesis of subject-specific healthy arterial spin labelling data. In addition, the framework could be extended to generate multi-modal Z-scores obtained from multiple modalities synthesised at the same time. This could be used to detect white matter lesions for the diagnosis of multiple sclerosis by synthesising subject-specific healthy fluid attenuation inversion recovery (FLAIR), T2-w and PD-w images from MRI contrasts where lesions are less visible, and comparing them by means of a multi-modal Z-score to the real images. Another example of application is the delineation of tumours in the context of radiotherapy treatment planning. The method could benefit from the multiple modalities made available by PET/MR scanners, such as diffusion weighted imaging and magnetisation transfer ratio, or tumour-specific PET tracers (e.g. choline PET) to estimate the degree of abnormality of pathological tumorous regions. This degree of abnormality would not only be used to delineate the tumour, but also to provide a spatially-varying estimate of the required dose.

The methods developed in this thesis could also be extended and applied to other aspects of radiotherapy, for example the automatic planning from MR images only. To deliver an optimal dose of radiation over the target area while sparing the normal tissues, RTP first requires contouring the target and organs at risk. Once these volumes have been defined, the optimal dose distribution for treating the tumour is determined according to the attenuation properties of the different tissues. As we have seen in chapter 10, when the planning is done only from MR images, the tissue attenuation properties can be derived from synthetic CT images. In clinical practice, the contouring of the organs at risk is done manually, a laborious and error prone task. A multi-atlas segmentation approach, based on the CT synthesis framework, could be used to delineate the critical organs. The multi-modal nature of the MR data could be exploited to align, morphologically match, and fuse all the image contrasts using a joint intensity model, allowing for a fully automated, accurate and robust segmentation of normal tissues.

Bibliography

Aasheim, L. B., Karlberg, A., Goa, P. E., Håberg, A., Sørhaug, S., Fagerli, U.-M., and Eikenes, L. (2015). PET/MR brain imaging: Evaluation of clinical UTE-based attenuation correction. *European Journal of Nuclear Medicine and Molecular Imaging*, 42(9):1439–1446.

Aitken, A. P., Giese, D., Tsoumpas, C., Schleyer, P., Kozerke, S., Prieto, C., and Schaeffter, T. (2014). Improved UTE-based attenuation correction for cranial PET-MR using dynamic magnetic field monitoring. *Medical Physics*, 41(1):012302.

Aljabar, P., Heckemann, R. A., Hammers, A., Hajnal, J. V., and Rueckert, D. (2009). Multi-atlas based segmentation of brain images: Atlas selection and its effect on accuracy. *NeuroImage*, 46(3):726–738.

Anazodo, U. C., Thiessen, J. D., Ssali, T., Mandel, J., Günther, M., Butler, J., Pavlosky, W., Prato, F. S., Thompson, R. T., and Lawrence, K. S. S. (2015). Feasibility of simultaneous whole-brain imaging on an integrated PET-MRI system using an enhanced 2-point Dixon attenuation correction method. *Frontiers in Neuroscience*, 8:434.

Andersen, F. L., Ladefoged, C. N., Beyer, T., Keller, S. H., Hansen, A. E., Højgaard, L., Kjær, A., Law, I., and Holm, S. (2014). Combined PET/MR imaging in neurology: MR-based attenuation correction implies a strong spatial bias when ignoring bone. *NeuroImage*, 84:206–216.

Andreasen, D., Van Leemput, K., Hansen, R. H., Andersen, J. A., and Edmund, J. M. (2015). Patch-based generation of a pseudo CT from conventional MRI sequences for MRI-only radiotherapy of the brain. *Medical Physics*, 42(4):1596–1605.

Ashburner, J. (2007). A fast diffeomorphic image registration algorithm. *NeuroImage*, 38(1):95–113.

Ashburner, J. and Friston, K. J. (2005). Unified segmentation. *NeuroImage*, 26(3):839–851.

Ay, M., Shirmohammad, M., and Sarkar, S. (2011). Comparative assessment of energy-mapping approaches in CT-based attenuation correction for PET. *Molecular Imaging and Biology*, 13(1):187–198.

Benoit, D., Ladefoged, C., Rezaei, A., Keller, S., Andersen, F., Hojgaard, L., Hansen, A. E., Holm, S., and Nuyts, J. (2015). PET/MR: Improvement of the UTE μ-maps using modified MLAA. *EJNMMI Physics*, 2(Suppl 1):A58.

Berker, Y., Franke, J., Salomon, A., Palmowski, M., Donker, H. C. W., Temur, Y., Mottaghy, F. M., Kuhl, C., Izquierdo-Garcia, D., Fayad, Z. A., Kiessling, F., and Schulz, V. (2012). MRI-based attenuation correction for hybrid PET/MRI systems: A 4-class tissue segmentation technique using a combined ultrashort-echo-time/Dixon MRI sequence. *Journal of Nuclear Medicine*, 53(5):796–804.

Berker, Y., Kiessling, F., and Schulz, V. (2014). Scattered PET data for attenuation-map reconstruction in PET/MRI. *Medical Physics*, 41(10):102502.

Beyer, T., Townsend, D. W., Brun, T., Kinahan, P. E., Charron, M., Roddy, R., Jerin, J., Young, J., Byars, L., and Nutt, R. (2000). A combined PET/CT scanner for clinical oncology. *Journal of Nuclear Medicine*, 41(8):1369–1379.

Bezrukov, I., Schmidt, H., Mantlik, F., Schwenzer, N., Brendle, C., Schölkopf, B., and Pichler, B. J. (2013). MR-based attenuation correction methods for improved PET quantification in lesions within bone and susceptibility artifact regions. *Journal of Nuclear Medicine*, 54(10):1768–1774.

Brendle, C., Schmidt, H., Oergel, A., Bezrukov, I., Mueller, M., Schraml, C., Pfannenberg, C., la Fougère, C., Nikolaou, K., and Schwenzer, N. (2015). Segmentation-based attenuation correction in positron emission tomography/magnetic resonance: Erroneous tissue identification and its impact on positron emission tomography interpretation. *Investigative Radiology*, 50(5):339–346.

Buch, S., Liu, S., Ye, Y., Cheng, Y.-C. N., Neelavalli, J., and Haacke, E. M. (2015). Susceptibility mapping of air, bone, and calcium in the head. *Magnetic Resonance in Medicine*, 73(6):2185–2194.

Burger, C., Goerres, G., Schoenes, S., Buck, A., Lonn, a. H. R., and Von Schulthess, G. K. (2002). PET attenuation coefficients from CT images: Experimental evaluation of the transformation of CT into PET 511-keV attenuation coefficients. *European Journal of Nuclear Medicine and Molecular Imaging*, 29(7):922–7.

Burgos, N., Cardoso, M. J., Thielemans, K., Modat, M., Dickson, J., Schott, J. M., Atkinson, D., Arridge, S. R., Hutton, B. F., and Ourselin, S. (2015a). Multi-contrast attenuation map synthesis for PET/MR scanners: Assessment on FDG and Florbetapir PET tracers. *European Journal of Nuclear Medicine and Molecular Imaging*, 42(9):1447–1458.

Burgos, N., Cardoso, M. J., Thielemans, K., Modat, M., Pedemonte, S., Dickson, J., Barnes, A., Ahmed, R., Mahoney, C. J., Schott, J. M., Duncan, J. S., Atkinson, D., Arridge, S. R., Hutton, B. F., and Ourselin, S. (2014a). Attenuation correction synthesis for hybrid PET-MR scanners: Application to brain studies. *Medical Imaging, IEEE Transactions on*, 33(12):2332–2341.

Burgos, N., Cardoso, M. J., Mendelson, A., Schott, J. M., Atkinson, D., Arridge, S. R., Hutton, B. F., and Ourselin, S. (2015b). Subject-specific models for the analysis of pathological FDG PET data. In *Medical Image Computing and Computer-Assisted Intervention MICCAI 2015*, pages 651–658.

Burgos, N., Cardoso, M. J., Thielemans, K., Duncan, J. S., Atkinson, D., Arridge, S. R., Hutton, B. F., and Ourselin, S. (2014b). Attenuation correction synthesis for hybrid PET-MR scanners: Validation for brain study applications. *EJNMMI Physics*, 1(Suppl 1):A52.

Burgos, N., Cardoso, M. J., Guerreiro, F., Veiga, C., Modat, M., McClelland, J., Knopf, A., Punwani, S., Atkinson, D., Arridge, S. R., Hutton, B. F., and Ourselin, S. (2015c). Robust CT synthesis for radiotherapy planning: Application to the head & neck region. In *Medical Image Computing and Computer-Assisted Intervention MICCAI 2015*, pages 476–484.

Burgos, N., Thielemans, K., Cardoso, M. J., Markiewicz, P., Jiao, J., Dickson, J., Duncan, J. S., Atkinson, D., Arridge, S. R., Hutton, B. F., and Ourselin, S. (2014c). Effect of scatter correction when comparing attenuation maps: Application to brain PET/MR. In *Nuclear Science Symposium Conference Record, 2014. NSS'14. IEEE*, pages 1–5.

Burgos, N., Cardoso, M. J., Guerreiro, F., McClelland, J., Knopf, A., Punwani, S., and Ourselin, S. (2016). CT Synthesis in the head & neck and pelvic regions for radiotherapy treatment planning. In *IPEM Workshop on MRI Guided Radiotherapy*.

Burgos, N., Cardoso, M. J., Modat, M., Pedemonte, S., Dickson, J., Barnes, A., Duncan, J. S., Atkinson, D., Arridge, S. R., Hutton, B. F., and Ourselin, S. (2013). Attenuation correction synthesis for hybrid PET-MR scanners. In *Medical Image Computing and Computer-Assisted Intervention MICCAI 2013*, pages 147–154.

Burgos, N., Cardoso, M. J., Modat, M., Punwani, S., Atkinson, D., Arridge, S. R., Hutton, B. F., and Ourselin, S. (2015d). CT Synthesis in the head & neck region for PET/MR attenuation correction: An iterative multi-atlas approach. *EJNMMI Physics*, 2(Suppl 1):A31.

Cabello, J., Lukas, M., Förster, S., Pyka, T., Nekolla, S. G., and Ziegler, S. I. (2015). MR-Based attenuation correction using ultrashort-echo-time pulse sequences in dementia patients. *Journal of Nuclear Medicine*, 56(3):423–429.

Cachier, P., Bardinet, E., Dormont, D., Pennec, X., and Ayache, N. (2003). Iconic feature based nonrigid registration: The PASHA algorithm. *Computer Vision and Image Understanding*, 89(2-3):272–298.

Cardoso, M., Modat, M., Wolz, R., Melbourne, A., Cash, D., Rueckert, D., and Ourselin, S. (2015). Geodesic information flows: Spatially-variant graphs and their application to segmentation and fusion. *Medical Imaging, IEEE Transactions on*, 34(9):1976–1988.

Cardoso, M., Wolz, R., Modat, M., Fox, N. C., Rueckert, D., and Ourselin, S. (2012). Geodesic information flows. In *Medical Image Computing and Computer-Assisted Intervention MICCAI 2012*, volume 7511, pages 262–270.

Cardoso, M. J., Clarkson, M. J., Ridgway, G. R., Modat, M., Fox, N. C., Ourselin, S., and The Alzheimer's Disease Neuroimaging Initiative (2011). LoAd: A locally adaptive cortical segmentation algorithm. *NeuroImage*, 56(3):1386–1397.

Carney, J., Townsend, D. W., Rappoport, V., and Bendriem, B. (2006). Method for transforming CT images for attenuation correction in PET/CT imaging. *Medical Physics*, 33(4):976–983.

Catana, C., Benner, T., van der Kouwe, A., Byars, L., Hamm, M., Chonde, D. B., Michel, C. J., El Fakhri, G., Schmand, M., and Sorensen, A. G. (2011). MRI-assisted PET motion correction for neurologic studies in an integrated MR-PET scanner. *Journal of Nuclear Medicine*, 52(1):154–161.

Catana, C., Drzezga, A., Heiss, W.-D., and Rosen, B. R. (2012). PET/MRI for neurologic applications. *Journal of Nuclear Medicine*, 53(12):1916–1925.

Catana, C., Guimaraes, A. R., and Rosen, B. R. (2013). PET and MR imaging: The odd couple or a match made in heaven? *Journal of Nuclear Medicine*, 54(5):815–824.

Catana, C., van der Kouwe, A., Benner, T., Michel, C. J., Hamm, M., Fenchel, M., Fischl, B., Rosen, B., Schmand, M., and Sorensen, a. G. (2010). Toward implementing an MRI-based PET attenuation-correction method for neurologic studies on the MR-PET brain prototype. *Journal of Nuclear Medicine*, 51(9):1431–8.

Censor, Y., Gustafson, D. E., Lent, A., and Tuy, H. (1979). A new approach to the emission computerized tomography problem: Simultaneous calculation of attenuation and activity coefficients. *Nuclear Science, IEEE Transactions on*, 26(2):2775–2779.

Chang, T., Diab, R. H., Clark Jr, J. W., and Mawlawi, O. R. (2013). Investigating the use of nonattenuation corrected PET images for the attenuation correction of PET data. *Medical Physics*, 40(8):082508.

Chen, Y., Juttukonda, M., Su, Y., Benzinger, T., Rubin, B. G., Lee, Y. Z., Lin, W., Shen, D., Lalush, D., and An, H. (2015). Probabilistic air segmentation and sparse regression estimated pseudo CT for PET/MR attenuation correction. *Radiology*, 275(2):562–569.

Crutch, S. J., Lehmann, M., Schott, J. M., Rabinovici, G. D., Rossor, M. N., and Fox, N. C. (2012). Posterior cortical atrophy. *The Lancet Neurology*, 11(2):170–178.

Defrise, M., Rezaei, A., and Nuyts, J. (2012). Time-of-flight PET data determine the attenuation sinogram up to a constant. *Physics in Medicine and Biology*, 57(4):885.

Defrise, M., Rezaei, A., and Nuyts, J. (2014). Transmission-less attenuation correction in time-of-flight PET: Analysis of a discrete iterative algorithm. *Physics in Medicine and Biology*, 59(4):1073.

Department of Health (2012). Radiotherapy services in England 2012. `https://www.gov.uk/government/publications/radiotherapy-services-in-england-2012`.

Dickson, J. C., O'Meara, C., and Barnes, A. (2014). A comparison of CT- and MR-based attenuation correction in neurological PET. *European Journal of Nuclear Medicine and Molecular Imaging*, 41(6):1176–1189.

Dixon, W. T. (1984). Simple proton spectroscopic imaging. *Radiology*, 153(1):189–194.

Dowling, J. A., Lambert, J., Parker, J., Salvado, O., Fripp, J., Capp, A., Wratten, C., Denham, J. W., and Greer, P. B. (2012). An atlas-based electron density mapping method for magnetic resonance imaging (MRI)-alone treatment planning and adaptive MRI-based prostate radiation therapy. *International Journal of Radiation Oncology · Biology · Physics*, 83(1):e5–e11.

Drzezga, A., Grimmer, T., Riemenschneider, M., Lautenschlager, N., Siebner, H., Alexopoulus, P., Minoshima, S., Schwaiger, M., and Kurz, A. (2005). Prediction of individual clinical outcome in MCI by means of genetic assessment and ^{18}F-FDG PET. *Journal of Nuclear Medicine*, 46(10):1625–1632.

Erlandsson, K., Buvat, I., Pretorius, P. H., Thomas, B. A., and Hutton, B. F. (2012). A review of partial volume correction techniques for emission tomography and their applications in neurology, cardiology and oncology. *Physics in Medicine and Biology*, 57(21):R119.

Fehily, A. M., Coles, R. J., Evans, W. D., and Elwood, P. C. (1992). Factors affecting bone density in young adults. *The American Journal of Clinical Nutrition*, 56(3):579–586.

Fei, B., Yang, X., Nye, J. A., Aarsvold, J. N., Raghunath, N., Cervo, M., Stark, R., Meltzer, C. C., and Votaw, J. R. (2012). MR/PET quantification tools: Registration, segmentation, classification, and MR-based attenuation correction. *Medical Physics*, 39(10):6443–6454.

Gudur, M. S. R., Hara, W., Le, Q.-T., Wang, L., Xing, L., and Li, R. (2014). A unifying probabilistic Bayesian approach to derive electron density from MRI for radiation therapy treatment planning. *Physics in Medicine and Biology*, 59(21):6595.

Guerreiro, F. (2015). Calibration of MR Images for Accurate Dose Calculations. Master's thesis, Universidade de Lisboa, Portugal.

Guerreiro, F., McClelland, J., Burgos, N., Cardoso, M., Dunlop, A., Wong, K., Nill, S., Oelfke, U., and AC, K. (2015). Evaluation of different approaches to obtain synthetic CT images for a MRI-only radiotherapy workflow. In *MR in RT Symposium*.

Heckemann, R. A., Hajnal, J. V., Aljabar, P., Rueckert, D., and Hammers, A. (2006). Automatic anatomical brain MRI segmentation combining label propagation and decision fusion. *NeuroImage*, 33(1):115–26.

Heckemann, R. A., Keihaninejad, S., Aljabar, P., Rueckert, D., Hajnal, J. V., Hammers, A., and The Alzheimer's Disease Neuroimaging Initiative (2010). Improving intersubject image registration using tissue-class information benefits robustness and accuracy of multi-atlas based anatomical segmentation. *NeuroImage*, 51(1):221–227.

Heiss, W.-D. (2009). The potential of PET/MR for brain imaging. *European Journal of Nuclear Medicine and Molecular Imaging*, 36(1):105–112.

Herholz, K. (2003). PET studies in dementia. *Annals of Nuclear Medicine*, 17(2):79–89.

Herholz, K. (2014). The role of PET quantification in neurological imaging: FDG and amyloid imaging in dementia. *Clinical and Translational Imaging*, 2(4):321–330.

Herzog, H., Langen, K., Weirich, C., Rota Kops, E., Kaffanke, J., Tellmann, L., Scheins, J., Neuner, I., Stoffels, G., Fischer, K., Caldeira, L., Coenen, H. H., and Shah, N. J. (2011). High resolution BrainPET combined with simultaneous MRI. *Nuklearmedizin-Nuclear Medicine*, 50(2):74.

Hess, S., Blomberg, B. A., Zhu, H. J., Høilund-Carlsen, P. F., and Alavi, A. (2014). The pivotal role of FDG-PET/CT in modern medicine. *Academic Radiology*, 21(2):232–249.

Hofmann, M., Bezrukov, I., Mantlik, F., Aschoff, P., Steinke, F., Beyer, T., Pichler, B. J., and Schölkopf, B. (2011). MRI-based attenuation correction for whole-body PET/MRI: Quantitative evaluation of segmentation-and atlas-based methods. *Journal of Nuclear Medicine*, 52(9):1392–1399.

Hofmann, M., Steinke, F., Scheel, V., Charpiat, G., Farquhar, J., Aschoff, P., Brady, M., Schölkopf, B., and Pichler, B. J. (2008). MRI-based attenuation correction for PET/MRI: A novel approach combining pattern recognition and atlas registration. *Journal of Nuclear Medicine*, 49(11):1875–83.

Horch, R. A., Nyman, J. S., Gochberg, D. F., Dortch, R. D., and Does, M. D. (2010). Characterization of ^{1}H NMR signal in human cortical bone for magnetic resonance imaging. *Magnetic Resonance in Medicine*, 64(3):680–687.

Hsu, S.-H., Cao, Y., Huang, K., Feng, M., and Balter, J. M. (2013). Investigation of a method for generating synthetic CT models from MRI scans of the head and neck for radiation therapy. *Physics in Medicine and Biology*, 58(23):8419.

Huang, C., Ouyang, J., Reese, T., Wu, Y., El Fakhri, G., and Ackerman, J. (2015). Continuous MR bone density measurement using water-and fat-suppressed projection imaging (WASPI) for PET attenuation correction in PET-MR. *Physics in Medicine and Biology*, 60(20):N369.

Hutton, B. F., Thomas, B. A., Erlandsson, K., Bousse, A., Reilhac-Laborde, A., Kazantsev, D., Pedemonte, S., Vunckx, K., Arridge, S., and Ourselin, S. (2013). What approach to brain partial volume correction is best for PET/MRI? *Nuclear Instruments and Methods in Physics Research Section A: Accelerators, Spectrometers, Detectors and Associated Equipment*, 702:29–33.

Huynh, T., Gao, Y., Kang, J., Wang, L., Zhang, P., Lian, J., and Shen, D. (2016). Estimating CT image from MRI data using structured random forest and auto-context model. *Medical Imaging, IEEE Transactions on*, 35(1):174–183.

Izquierdo-Garcia, D., Hansen, A. E., Förster, S., Benoit, D., Schachoff, S., Frst, S., Chen, K. T., Chonde, D. B., and Catana, C. (2014). An SPM8-based approach for attenuation correction combining segmentation and nonrigid template formation: Application to simultaneous PET/MR brain imaging. *Journal of Nuclear Medicine*, 55(11):1825–1830.

Johansson, A., Garpebring, A., Karlsson, M., Asklund, T., and Nyholm, T. (2013). Improved quality of computed tomography substitute derived from magnetic resonance (MR) data by incorporation of spatial information–Potential application for MR-only radiotherapy and attenuation correction in positron emission tomography. *Acta Oncologica*, 52(7):1369–73.

Johansson, A., Karlsson, M., and Nyholm, T. (2011). CT substitute derived from MRI sequences with ultrashort echo time. *Medical Physics*, 38(5):2708.

Jonsson, J., Akhtari, M., Karlsson, M., Johansson, A., Asklund, T., and Nyholm, T. (2015). Accuracy of inverse treatment planning on substitute CT images derived from MR data for brain lesions. *Radiation Oncology*, 10(1):1.

Juttukonda, M. R., Mersereau, B. G., Chen, Y., Su, Y., Rubin, B. G., Benzinger, T. L., Lalush, D. S., and An, H. (2015). MR-based attenuation correction for PET/MRI neurological studies with continuous-valued attenuation coefficients for bone through a conversion from R2* to CT-Hounsfield units. *NeuroImage*, 112:160–168.

Kawaguchi, H., Hirano, Y., Yoshida, E., Kershaw, J., Shiraishi, T., Suga, M., Ikoma, Y., Obata, T., Ito, H., and Yamaya, T. (2014). A proposal for PET/MRI attenuation correction with μ-values measured using a fixed-position radiation source and MRI segmentation. *Nuclear Instruments and Methods in Physics Research Section A: Accelerators, Spectrometers, Detectors and Associated Equipment*, 734:156–161.

Keereman, V., Fierens, Y., Broux, T., De Deene, Y., Lonneux, M., and Vandenberghe, S. (2010). MRI-based attenuation correction for PET/MRI using ultrashort echo time sequences. *Journal of Nuclear Medicine*, 51(5):812–8.

Khateri, P., Rad, H. S., Jafari, A. H., Kazerooni, A. F., Akbarzadeh, A., Moghadam, M. S., Aryan, A., Ghafarian, P., and Ay, M. R. (2015). Generation of a four-class attenuation map for MRI-based attenuation correction of PET data in the head area using a novel combination of STE/Dixon-MRI and FCM clustering. *Molecular Imaging and Biology*, 17(6):884–892.

Klemt, C., Modat, M., Pichat, J., Cardoso, M., Henckel, J., Hart, A., and Ourselin, S. (2015). Automatic assessment of volume asymmetries applied to hip abductor muscles in patients with hip arthroplasty. In *Proc. SPIE, Medical Imaging*, pages 94131M–94131M.

Koesters, T., Friedman, K. P., Fenchel, M., Zhan, Y., Hermosillo, G., Babb, J., Jelescu, I. O., Faul, D., Boada, F. E., and Shepherd, T. M. (2016). Dixon sequence with superimposed model-based bone compartment provides highly accurate PET/MR attenuation correction of the brain. *Journal of Nuclear Medicine*, 57(6):918–924.

Kops, E. R. and Herzog, H. (2007). Alternative methods for attenuation correction for PET images in MR-PET scanners. In *Nuclear Science Symposium Conference Record, 2007. NSS'07. IEEE*, volume 6, pages 4327–4330.

Kops, E. R. and Herzog, H. (2008). Template based attenuation correction for PET in MR-PET scanners. In *Nuclear Science Symposium Conference Record, 2008. NSS'08. IEEE*, pages 3786–3789.

Korhonen, J., Kapanen, M., Keyriläinen, J., Seppälä, T., and Tenhunen, M. (2014). A dual model HU conversion from MRI intensity values within and outside of bone segment for MRI-based radiotherapy treatment planning of prostate cancer. *Medical Physics*, 41(1):011704.

Kristan, M. and Pernus, F. (2004). Entropy based measure of camera focus. In *Proc. ERK2004*, pages 179–182.

Ladefoged, C. N., Benoit, D., Law, I., Holm, S., Kjær, A., Højgaard, L., Hansen, A. E., and Andersen, F. L. (2015). Region specific optimization of continuous linear attenuation coefficients based on UTE (RESOLUTE): Application to PET/MR brain imaging. *Physics in Medicine and Biology*, 60(20):8047.

Ladefoged, C. N., Law, I., Anazodo, U., St. Lawrence, K., Izquierdo-Garcia, D., Catana, C., Burgos, N., Cardoso, M. J., Hutton, B. F., Ourselin, S., Merida, I., Costes, N., Hammers, A., Benoit, D., Holm, S., Juttukonda, M., An, H., Cabello, J., Lukas, M., Nekolla, S., Ziegler, S., Fenchel, M., Jakoby, B., Casey, M., Benzinger, T., Højgaard, L., Hansen, A. E., and Andersen, F. L. (2016). Multi-center evaluation of eleven PET/MRI brain attenuation correction methods. In *Nuclear Science Symposium Conference Record, 2016. NSS'16. IEEE.*

Le Goff-Rougetet, R., Frouin, V., Mangin, J.-F., and Bendriem, B. (1994). Segmented MR images for brain attenuation correction in PET. In *Medical Imaging 1994*, pages 725–736.

Lee, E. M., Park, G. Y., Im, K. C., Kim, S. T., Woo, C.-W., Chung, J. H., Kim, K. S., Kim, J. S., Shon, Y.-M., Kim, Y. I., and Kang, J. K. (2012). Changes in glucose metabolism and metabolites during the epileptogenic process in the lithium-pilocarpine model of epilepsy. *Epilepsia*, 53(5):860–869.

Li, Y., Defrise, M., Metzler, S. D., and Matej, S. (2015). Transmission-less attenuation estimation from time-of-flight PET histo-images using consistency equations. *Physics in Medicine and Biology*, 60(16):6563.

Low, D. A., Harms, W. B., Mutic, S., and Purdy, J. A. (1998). A technique for the quantitative evaluation of dose distributions. *Medical Physics*, 25(5):656–661.

Maddams, J., Utley, M., and Møller, H. (2012). Projections of cancer prevalence in the United Kingdom, 2010–2040. *British Journal of Cancer*, 107(7):1195–1202.

Manber, R., Thielemans, K., Hutton, B., Barnes, A., Ourselin, S., Arridge, S., OMeara, C., and Atkinson, D. (2014). Initial evaluation of a practical PET respiratory motion correction method in clinical simultaneous PET/MRI. *EJNMMI Physics*, 1(Suppl 1):A40.

Marshall, H. R., Patrick, J., Laidley, D., Prato, F. S., Butler, J., Théberge, J., Thompson, R. T., and Stodilka, R. Z. (2013). Description and assessment of a registration-based approach to include bones for attenuation correction of whole-body PET/MRI. *Medical Physics*, 40(8):082509.

Marshall, H. R., Patrick, J., Laidley, D., Prato, F. S., Deans, L., Thberge, J., Thompson, R. T., and Stodilka, R. Z. (2012). Variable lung density consideration in attenuation correction of whole-body PET/MRI. *Journal of Nuclear Medicine*, 53(6):977–984.

Martinez-Möller, A., Souvatzoglou, M., Delso, G., Bundschuh, R. A., Chefd'hotel, C., Ziegler, S. I., Navab, N., Schwaiger, M., and Nekolla, S. G. (2009). Tissue classification as a potential approach for attenuation correction in whole-body PET/MRI: Evaluation with PET/CT data. *Journal of Nuclear Medicine*, 50(4):520–6.

Mehranian, A. and Zaidi, H. (2015). Emission-based estimation of lung attenuation coefficients for attenuation correction in time-of-flight PET/MR. *Physics in Medicine and Biology*, 60(12):4813.

Meikle, S. and Badawi, R. (2005). Quantitative techniques in PET. In Bailey, D., Townsend, D., Valk, P., and Maisey, M., editors, *Positron Emission Tomography*, pages 93–126. Springer.

Meikle, S. R., Bailey, D. L., Hooper, P. K., Eberl, S., Hutton, B. F., Jones, W. F., Fulton, R. R., and Fulham, M. J. (1995). Simultaneous emission and transmission measurements for attenuation correction in whole-body PET. *Journal of Nuclear Medicine*, 36(9):1680–1688.

Merida, I., Costes, N., Heckemann, R. A., Drzezga, A., Forster, S., and Hammers, A. (2015). Evaluation of several multi-atlas methods for pseudo-CT generation in brain MRI-PET attenuation correction. In *Biomedical Imaging (ISBI), 2015 IEEE 12th International Symposium on*, pages 1431–1434.

Michel, C., Sibomana, M., Boi, A., Bernard, X., Lonneux, M., Defrise, M., Comtat, C., Kinahan, P., and Townsend, D. (1998). Preserving Poisson characteristics of PET data with weighted OSEM reconstruction. In *Nuclear Science Symposium, 1998. Conference Record. 1998 IEEE*, volume 2, pages 1323–1329.

Minoshima, S., Frey, K. A., Foster, N. L., and Kuhl, D. E. (1995). Preserved pontine glucose metabolism in Alzheimer disease: A reference region for functional brain image (PET) analysis. *Journal of Computer Assisted Tomography*, 19(4):541–547.

Modat, M., Cash, D. M., Daga, P., Winston, G. P., Duncan, J. S., and Ourselin, S. (2014). A symmetric block-matching framework for global registration. In *Proc. SPIE, Medical Imaging*, volume 9034, pages 90341D–90341D.

Modat, M., Ridgway, G. R., Daga, P., Cardoso, M. J., Ashburner, J., and Ourselin, S. (2012). Parametric non-rigid registration using a stationary velocity field. In *Mathematical Methods in Biomedical Image Analysis (MMBIA), 2012 IEEE Workshop on*, pages 145–150.

Modat, M., Taylor, Z. A., Lehmann, M., Barnes, J., Hawkes, D. J., Fox, N. C., and Ourselin, S. (2010). Fast free-form deformation using graphics processing units. *Computer Methods and Programs in Biomedicine*, 98(3):278–84.

Mollet, P., Keereman, V., Bini, J., Izquierdo-Garcia, D., Fayad, Z. A., and Vandenberghe, S. (2014). Improvement of attenuation correction in time-of-flight PET/MR imaging with a positron-emitting source. *Journal of Nuclear Medicine*, 55(2):329–336.

Mollet, P., Keereman, V., Clementel, E., and Vandenberghe, S. (2012). Simultaneous MR-compatible emission and transmission imaging for PET using time-of-flight information. *Medical Imaging, IEEE Transactions on*, 31(9):1734–1742.

Montandon, M.-L. and Zaidi, H. (2005). Atlas-guided non-uniform attenuation correction in cerebral 3D PET imaging. *NeuroImage*, 25(1):278–286.

Natterer, F. and Herzog, H. (1992). Attenuation correction in positron emission tomography. *Mathematical Methods in the Applied Sciences*, 15(5):321–330.

Navalpakkam, B. K., Braun, H., Kuwert, T., and Quick, H. H. (2013). Magnetic resonance-based attenuation correction for PET/MR hybrid imaging using continuous valued attenuation maps. *Investigative Radiology*, 48(5):323–32.

Nestor, P. J., Graham, N. L., Fryer, T. D., Williams, G. B., Patterson, K., and Hodges, J. R. (2003). Progressive non-fluent aphasia is associated with hypometabolism centred on the left anterior insula. *Brain*, 126(11):2406–2418.

Nuyts, J., Dupont, P., Stroobants, S., Benninck, R., Mortelmans, L., and Suetens, P. (1999). Simultaneous maximum a posteriori reconstruction of attenuation and activity distributions from emission sinograms. *Medical Imaging, IEEE Transactions on*, 18(5):393–403.

Ostertag, H., Kübler, W. K., Doll, J., and Lorenz, W. J. (1989). Measured attenuation correction methods. *European Journal of Nuclear Medicine*, 15(11):722–726.

Ourselin, S., Roche, A., Subsol, G., Pennec, X., and Ayache, N. (2001). Reconstructing a 3D structure from serial histological sections. *Image and Vision Computing*, 19(1):25–31.

Ouyang, J., Li, Q., and El Fakhri, G. (2013). Magnetic resonance-based motion correction for positron emission tomography imaging. In *Seminars in Nuclear Medicine*, volume 43, pages 60–67.

Pajevic, S., Daube-Witherspoon, M., Bacharach, S. L., and Carson, R. (1998). Noise characteristics of 3-D and 2-D PET images. *Medical Imaging, IEEE Transactions on*, 17(1):9–23.

Paulus, D. H., Quick, H. H., Geppert, C., Fenchel, M., Zhan, Y., Hermosillo, G., Faul, D., Fernando, B., Friedman, K., and Koesters, T. (2015). Whole-body PET/MR imaging: Quantitative evaluation of a novel model-based MR attenuation correction method including bone. *Journal of Nuclear Medicine*, 56(7):1061–1066.

Poynton, C. B., Chen, K. T., Chonde, D. B., Izquierdo-Garcia, D., Gollub, R. L., Gerstner, E. R., Batchelor, T. T., and Catana, C. (2014). Probabilistic atlas-based segmentation of combined T1-weighted

and DUTE MRI for calculation of head attenuation maps in integrated PET/MRI scanners. *American Journal of Nuclear Medicine and Molecular Imaging*, 4(2):160.

Qi, J. and Leahy, R. M. (2006). Iterative reconstruction techniques in emission computed tomography. *Physics in Medicine and Biology*, 51(15):R541.

Rabinovici, G. D., Jagust, W. J., Furst, A. J., Ogar, J. M., Racine, C. A., Mormino, E. C., O'Neil, J. P., Lal, R. A., Dronkers, N. F., Miller, B. L., and Gorno-Tempini, M. L. (2008). Aβ amyloid and glucose metabolism in three variants of primary progressive aphasia. *Annals of Neurology*, 64(4):388–401.

Rasmussen, C. E. and Williams, C. K. (2006). *Gaussian Processes for Machine Learning*. The MIT Press.

Reader, A. J. and Zaidi, H. (2007). Advances in PET image reconstruction. *PET Clinics*, 2(2):173–190.

Reich, N. E., Seidelmann, F. E., Tubbs, R., Mac Intyre, W. J., Meaney, T., Alfidi, R., and Pepe, R. (1976). Determination of bone mineral content using CT scanning. *American Journal of Roentgenology*, 127(4):593–594.

Rezaei, A., Defrise, M., Bal, G., Michel, C., Conti, M., Watson, C., and Nuyts, J. (2012). Simultaneous reconstruction of activity and attenuation in time-of-flight PET. *Medical Imaging, IEEE Transactions on*, 31(12):2224–2233.

Rezaei, A., Defrise, M., and Nuyts, J. (2014). ML-reconstruction for TOF-PET with simultaneous estimation of the attenuation factors. *Medical Imaging, IEEE Transactions on*, 33(7):1563–1572.

Robson, M. D., Gatehouse, P. D., Bydder, M., and Bydder, G. M. (2003). Magnetic resonance: An introduction to ultrashort TE (UTE) imaging. *Journal of Computer Assisted Tomography*, 27(6):825–846.

Rohlfing, T., Brandt, R., Maurer, C.R., J., and Menzel, R. (2001). Bee brains, B-splines and computational democracy: Generating an average shape atlas. In *Mathematical Methods in Biomedical Image Analysis (MMBIA), 2001 IEEE Workshop on*, pages 187–194.

Roy, S., Wang, W.-T., Carass, A., Prince, J. L., Butman, J. A., and Pham, D. L. (2014). PET attenuation correction using synthetic CT from ultrashort echo-time MR imaging. *Journal of Nuclear Medicine*, 55(12):2071–2077.

Sabuncu, M. R., Van Leemput, K., Fischl, B., and Golland, P. (2010). A generative model for image segmentation based on label fusion. *Medical Imaging, IEEE Transactions on*, 29(10):1714–1729.

Salomon, A., Goedicke, A., Schweizer, B., Aach, T., and Schulz, V. (2011). Simultaneous reconstruction of activity and attenuation for PET/MR. *Medical Imaging, IEEE Transactions on*, 30(3):804–13.

Sari, H., Erlandsson, K., Thielemans, K., Atkinson, D., Ourselin, S., Arridge, S. R., and Hutton, B. F. (2015). Incorporation of MRI-AIF information for improved kinetic modelling of dynamic PET data. *Nuclear Science, IEEE Transactions on*, 62(3):612–618.

Schlemmer, H.-P. W., Pichler, B. J., Schmand, M., Burbar, Z., Michel, C., Ladebeck, R., Jattke, K., Townsend, D., Nahmias, C., Jacob, P. K., Heiss, W.-D., and Claussen, C. D. (2008). Simultaneous MR/PET imaging of the human brain: Feasibility study. *Radiology*, 248(3):1028–1035.

Schleyer, P. J., Schaeffter, T., and Marsden, P. K. (2010). The effect of inaccurate bone attenuation coefficient and segmentation on reconstructed PET images. *Nuclear Medicine Communications*, 31(8):708–16.

Schreibmann, E., Nye, J. A., Schuster, D. M., Martin, D. R., Votaw, J., and Fox, T. (2010). MR-based attenuation correction for hybrid PET-MR brain imaging systems using deformable image registration. *Medical Physics*, 37(5):2101.

Schulte-Geers, C., Obert, M., Schilling, R., Harth, S., Traupe, H., Gizewski, E., and Verhoff, M. (2011). Age and gender-dependent bone density changes of the human skull disclosed by high-resolution flat-panel computed tomography. *International Journal of Legal Medicine*, 125(3):417–425.

Schulz, V., Torres-Espallardo, I., Renisch, S., Hu, Z., Ojha, N., Börnert, P., Perkuhn, M., Niendorf, T., Schäfer, W. M., Brockmann, H., Krohn, T., Buhl, A., Günther, R. W., Mottaghy, F. M., and Krombach, G. A. (2011). Automatic, three-segment, MR-based attenuation correction for whole-body PET/MR data. *European Journal of Nuclear Medicine and Molecular Imaging*, 38(1):138–152.

Signorini, M., Paulesu, E., Friston, K., Perani, D., Colleluori, A., Lucignani, G., Grassi, F., Bettinardi, V., Frackowiak, R., and Fazio, F. (1999). Rapid assessment of regional cerebral metabolic abnormalities in single subjects with quantitative and nonquantitative [^{18}F]FDG PET: A clinical validation of statistical parametric mapping. *NeuroImage*, 9(1):63–80.

Sjölund, J., Forsberg, D., Andersson, M., and Knutsson, H. (2015). Generating patient specific pseudo-CT of the head from MR using atlas-based regression. *Physics in Medicine and Biology*, 60(2):825.

Sled, J. G., Zijdenbos, A. P., and Evans, A. C. (1998). A nonparametric method for automatic correction of intensity nonuniformity in MRI data. *Medical Imaging, IEEE Transactions on*, 17(1):87–97.

Su, K.-H., Hu, L., Stehning, C., Helle, M., Qian, P., Thompson, C. L., Pereira, G. C., Jordan, D. W., Herrmann, K. A., Traughber, M., Muzic, R. F., and Traughber, B. J. (2015). Generation of brain pseudo-CTs using an undersampled, single-acquisition UTE-mDixon pulse sequence and unsupervised clustering. *Medical Physics*, 42(8):4974–4986.

Thielemans, K., Tsoumpas, C., Mustafovic, S., Beisel, T., Aguiar, P., Dikaios, N., and Jacobson, M. W. (2012). STIR: Software for tomographic image reconstruction release 2. *Physics in Medicine and Biology*, 57(4):867–83.

Tong, S., Alessio, A. M., and Kinahan, P. E. (2010). Image reconstruction for PET/CT scanners: Past achievements and future challenges. *Imaging in Medicine*, 2(5):529–545.

Torrado-Carvajal, A., Herraiz, J. L., Alcain, E., Montemayor, A. S., Garcia-Caamaque, L., Hernandez-Tamames, J. A., Rozenholc, Y., and Malpica, N. (2016). Fast patch-based pseudo-CT synthesis from T1-weighted MR images for PET/MR attenuation correction in brain studies. *Journal of Nuclear Medicine*, 57(1):136–143.

Townsend, D. W. (2008). Dual-modality imaging: Combining anatomy and function. *Journal of Nuclear Medicine*, 49(6):938–955.

Uh, J., Merchant, T. E., Li, Y., Li, X., and Hua, C. (2014). MRI-based treatment planning with pseudo CT generated through atlas registration. *Medical Physics*, 41(5):051711.

Ullisch, M. G., Scheins, J. J., Weirich, C., Kops, E. R., Celik, A., Tellmann, L., Stöcker, T., Herzog, H., and Shah, N. J. (2012). MR-based PET motion correction procedure for simultaneous MR-PET neuroimaging of human brain. *PloS One*, 7(11):e48149.

Vapnik, V. (2000). *The Nature of Statistical Learning Theory*. Springer.

Wagenknecht, G., Kops, E. R., Tellmann, L., and Herzog, H. (2009). Knowledge-based segmentation of attenuation-relevant regions of the head in T1-weighted MR images for attenuation correction in MR/PET systems. In *Nuclear Science Symposium Conference Record, 2009. NSS'09. IEEE*, pages 3338–3343.

Watson, C. C. (2000). New, Faster, Image-Based Scatter Correctionfor 3D PET. *Nuclear Science, IEEE Transactions on*, 47(4):1587–1594.

Watson, C. C., Panin, V. Y., Keller, S. H., Holm, S., and Nuyts, J. (2014). A sparse transmission method for PET attenuation correction in the head. In *Nuclear Science Symposium Conference Record, 2014. NSS'14. IEEE*, pages 1–4.

Weinzapfel, B. T. and Hutchins, G. D. (2001). Automated PET attenuation correction model for functional brain imaging. *Journal of Nuclear Medicine*, 42(3):483–491.

Wiesinger, F., Sacolick, L. I., Menini, A., Kaushik, S. S., Ahn, S., Veit-Haibach, P., Delso, G., and Shanbhag, D. D. (2016). Zero TE MR bone imaging in the head. *Magnetic Resonance in Medicine*, 75(1):107–114.

Wong, D. F., Rosenberg, P. B., Zhou, Y., Kumar, A., Raymont, V., Ravert, H. T., Dannals, R. F., Nandi, A., Brašić, J. R., Ye, W., Hilton, J., Lyketsos, C., Kung, H. F., Joshi, A. D., Skovronsky, D. M., and Pontecorvo, M. J. (2010). In vivo imaging of amyloid deposition in Alzheimer disease using the radioligand 18F-AV-45 (Flobetapir F 18). *Journal of Nuclear Medicine*, 51(6):913–920.

Wu, Y., Yang, W., Lu, L., Lu, Z., Zhong, L., Yang, R., Huang, M., Feng, Y., Chen, W., and Feng, Q. (2015). Prediction of CT substitutes from MR images based on local sparse correspondence combination. In *Medical Image Computing and Computer-Assisted Intervention - MICCAI 2015*, pages 93–100.

Yang, X. and Fei, B. (2013). Multiscale segmentation of the skull in MR images for MRI-based attenuation correction of combined MR/PET. *Journal of the American Medical Informatics Association*, 20(6):1037–1045.

Yushkevich, P. A., Wang, H., Pluta, J., Das, S. R., Craige, C., Avants, B. B., Weiner, M. W., and Mueller, S. (2010). Nearly automatic segmentation of hippocampal subfields in in vivo focal T2-weighted MRI. *NeuroImage*, 53(4):1208–24.

Zaidi, H. and Koral, K. (2004). Scatter modelling and compensation in emission tomography. *European Journal of Nuclear Medicine and Molecular Imaging*, 31(5):761–782.

Zaidi, H., Montandon, M.-L., and Slosman, D. O. (2003). Magnetic resonance imaging-guided attenuation and scatter corrections in three-dimensional brain positron emission tomography. *Medical Physics*, 30(5):937–948.